

**CORNEAL VISUALIZATION AND CHARACTERIZATION FOR APPLICATIONS IN
OPHTHALMOLOGY USING OPTICAL IMAGING**

by

Tom Yu Chia Lai

B.A.Sc., University of British Columbia, 2010

A THESIS SUBMITTED IN PARTIAL FULFILMENT OF
THE REQUIREMENTS FOR THE DEGREE OF

MASTER OF APPLIED SCIENCE

in

The Faculty of Graduate and Postdoctoral Studies
(Biomedical Engineering)

THE UNIVERSITY OF BRITISH COLUMBIA

(Vancouver)

May 2014

© Tom Yu Chia Lai, 2014

ABSTRACT

Multiphoton microscopy (MPM) and optical coherence tomography (OCT) are two modalities suitable for imaging corneas. MPM is a nonlinear optical imaging technique that has sub-micron spatial resolution, deep penetration, and excellent optical-sectioning capability. It can detect two contrasts simultaneously: two-photon excited fluorescence (TPEF) and second harmonic generation (SHG). TPEF and SHG are used to visualize cells and collagen fibers, respectively. On the other hand, OCT is based on the detection of single-backscattered light using interferometry principles. Generally, it has micrometer-resolution and up to a few millimeters of imaging-depth. Combining MPM and OCT for corneal imaging is intuitive in the current study as the complementary information obtained from cornea helps us to understand the morphological and physiological status of the cornea. Furthermore, the MPM and OCT images can be used to quantitatively characterize the thicknesses and refractive index (RI) of the major corneal layers.

The visualization of the corneal morphology is important in ophthalmology. It can be used to: study the effects of contact lens wear and topical medications; diagnose corneal diseases such as infectious keratitis; and observe corneal ulcers, and keratoconus. In addition, the ability to quantitatively characterize the corneal thickness and RI is valuable for many ophthalmologic applications. These two parameters are useful for laser refractive surgeries, and the diagnosis of corneal degeneration, and endothelial dysfunction. They are also linked to other important parameters such as corneal hydration and intraocular pressure.

In this thesis, the capabilities of a combined MPM and OCT system for corneal imaging are demonstrated. Firstly, it is used to simultaneously visualize and compare the morphology, and to characterize the thicknesses and the RI of five different species' corneas. In order to

visualize the thicker tissues, the OCT modality is altered in two ways: a prism-based hardware dispersion balancing unit is added to minimize the dispersion mismatch in OCT; and an additional OCT configuration of objective lens and spectrometer setup was introduced. Secondly, the combined system is used to identify an induced parasitic infection in human corneas. The study serves as an important step forward to bring the combined MPM and OCT technology to clinical settings.

PREFACE

Chapter 3 is based on previous work conducted at the UBC Biophotonics Laboratory. The combined MPM and OCT system was built and tested by Dr. Shuo Tang, and two previous students, Kenny K. H. Chan and Yifeng Zhou. I was responsible for the implementation of the hardware dispersion balancing unit. I also investigated into the compound lens in the spectrometer to determine the optimal configurations to image the five species of corneas in Chapter 4. The MPM and OCT characterizations were determined by Yifeng Zhou and me.

A version of Chapter 4 has been accepted for publication at Biomedical Optics Express. Lai, T. and Tang, S. (2014) “Cornea characterization using a combined multiphoton microscopy and optical coherence tomography system,” Biomed. Opt. Express **5**(5), 1494-1511 (2014). I designed the experiments, conducted all the experiments, processed the results and wrote the manuscript.

In Chapter 5, the inoculation of the *ex vivo* human corneas was performed by a collaborating microbiologist, Dr. Miguel Imperial. I was responsible for: designing the experiment; obtaining UBC biosafety and human ethics approval; recruiting Dr. Imperial to perform the inoculation; recruiting Dr. Simon Holland, Dr. Gregory Moloney, and Dr. Johnson Tan as my clinical advisors; setting up the collaboration with Quantine Wong and Teresa Lo at the British Columbia Centre for Disease Control to use their parasitology lab for corneal storage and inoculation; conducting the experiments; and processing the results.

The certificate numbers for the biosafety, human ethics, and animal care approvals are H12-01682, A12-0182 and B12-0065, respectively. These certificates were used for both Chapters 4 and 5.

A list of publications is presented in Appendix C.

TABLE OF CONTENTS

Abstract.....	ii
Preface.....	iv
Table of Contents.....	v
List of Tables.....	viii
List of Figures.....	ix
List of Abbreviations.....	xiv
Acknowledgements.....	xv
Chapter 1: Introduction.....	1
1.1 Brief review of the anatomy and physiology of the cornea.....	1
1.1.1 Epithelium.....	2
1.1.2 Bowman’s layer.....	3
1.1.3 Stroma.....	3
1.1.4 Descemet’s membrane.....	4
1.1.5 Endothelium.....	4
1.2 Brief introduction to MPM.....	4
1.3 Brief introduction to OCT.....	5
1.4 Problem statement and motivation.....	6
1.5 Organization of the thesis.....	9
Chapter 2: Principles of MPM and OCT.....	11
2.1 Principles of MPM.....	11
2.1.1 Two-photon excited fluorescence (TPEF).....	11
2.1.2 Second harmonic generation (SHG).....	12
2.1.3 Advantages of MPM.....	13

2.2 Principles of OCT	14
2.2.1 Image depth	18
2.2.2 Dispersion Mismatch.....	19
2.2.3 Sensitivity fall-off.....	21
2.2.4 Advantages of OCT.....	22
Chapter 3: System.....	23
3.1 System overview	23
3.2 Objective lens.....	24
3.3 Spectrometer	25
3.4 Hardware dispersion balancing unit.....	26
3.5 OCT characterization	33
3.6 MPM Characterization	37
Chapter 4: Corneal Characterization Application.....	38
4.1 Introduction and motivation.....	38
4.2 Method	39
4.2.1 Acquisition and Preparation of the corneal tissues.....	39
4.2.2 MPM/OCT imaging and RI and thickness measurement	40
4.3 Morphology.....	44
4.3.1 Murine cornea	44
4.3.2 Piscine cornea	47
4.3.3 Human cornea	49
4.3.4 Porcine cornea.....	51
4.3.5 Bovine cornea	55
4.4 Quantitative Characterization.....	57

4.5 Discussion	63
4.5.1 Cornea transparency	63
5.5.1 Morphology	66
5.5.3 Quantitative Characterization	67
Chapter 5: Induced Acanthamoeba Keratitis Imaging application	69
5.1 Introduction	69
5.1.1 Acanthamoeba Keratitis.....	69
5.1.2 Project motivation and overview	73
5.2 Method	75
5.3 Results	77
5.4 Discussion	80
Chapter 6: Conclusions and Future Work.....	82
6.1 Conclusions	82
6.2 Future work	84
Bibliography	86
Appendix A: Groundwork for Chapter 5	94
Appendix B: Research Ethics	96
Appendix C: List of Publications.....	97

LIST OF TABLES

Table 3.1: Objective lens and spectrometer configuration for MPM and OCT.....	26
Table 3.2: SNR, axial resolution and sensitivity fall-off without software dispersion compensation and without hardware dispersion balancing (10× objective lens in conjunction with the spectrometer compound lens of effective focal length of 37.5 mm)	29
Table 3.3: SNR, axial resolution and sensitivity fall-off without software dispersion compensation and with hardware dispersion balancing (10× objective lens in conjunction with the spectrometer compound lens of effective focal length of 37.5 mm)	30
Table 3.4: SNR, axial resolution and sensitivity fall-off with both software dispersion compensation and hardware dispersion balancing (10× objective lens in conjunction with the spectrometer compound lens of effective focal length of 37.5 mm)	31
Table 3.5: SNR, axial resolution and sensitivity fall-off of the 4× objective lens in conjunction with the spectrometer compound lens of effective focal length of 100 mm.....	35
Table 4.1: RI and thickness results for 6 murine corneas	57
Table 4.2: RI and thickness results for 6 piscine corneas	58
Table 4.3: RI and thickness results for 8 human corneas	58
Table 4.4 RI and thickness results for 3 porcine corneas	59
Table 4.5: RI and thickness results for 5 bovine corneas	59
Table 4.6: Refractive index and thickness results for murine, piscine, human, porcine and bovine corneas	62
Table A.1: List of people involved	95

LIST OF FIGURES

Figure 1.1: Anatomy of the eye [4].....	2
Figure 1.2: Anatomical structure of the cornea [5].....	3
Figure 2.1: OPEF and TPEF excitation energy diagram. (a) OPEF excitation energy diagram. (b) TPEF excitation energy diagram.	12
Figure 2.2: The SHG process. (a) Two photons with the same frequency interact with a tissue to generate a new photon with twice the energy and half the wavelength of the initial photons. (b) SHG excitation energy diagram.....	13
Figure 2.3: Localization of excitation by two-photon excitation [10]. (a) One-photon excitation of fluorescein by focused 488 nm light (0.16 NA). (b) Two-photon excitation using focused (0.16 NA) femtosecond pulses of 960 nm light.....	14
Figure 2.4: Michelson interferometer. L_r and L_s are the reference arm length and sample arm length respectively.	16
Figure 2.5: SD-OCT.....	17
Figure 2.6: Measured interference fringe signal and reconstructed axial profile of reflectivity in SD-OCT [39]. Reconstructed axial profiles $I(\text{pixels})$ at different depths (right) from their measured signals $I(k)$ (left).	18
Figure 2.7: PSF of a mirror sample with and without software dispersion compensation. Intensity (decibels) versus depth (pixels) of the reconstructed axial profiles of a mirror sample with and without software dispersion compensation in red and in blue respectively (No hardware dispersion compensation components).	21
Figure 3.1: Experimental setup of the combined MPM/OCT imaging system. PMT: photomultiplier tube. HDBU: hardware dispersion balancing unit.	24
Figure 3.2: Mirror PSF for 1-7 N-BK7 glass slides (10× objective lens). The 3dB width of the PSF decreases until 5 N-BK7 glass slides then increases. Therefore the amount of N-BK7 glass needed to balance the OCT reference and sample arms is around 5 mm.	27
Figure 3.3: Hardware dispersion balancing unit. (a) By arranging the adjustable glass prism, the total thickness of N-BK7 glass traveled by the reference beam can be set to balance the dispersion mismatch for the 4× objective lens. (b) By moving the adjustable glass prism, the	

thickness can be decreased to accommodate the thickness needed to balance the dispersion mismatch for the 10× objective lens.	28
Figure 3.4: PSF of a mirror at different depths without software dispersion compensation and without hardware dispersion balancing (10× objective lens in conjunction with the spectrometer compound lens of effective focal length of 37.5 mm)	29
Figure 3.5: PSF of a mirror at different depths without software dispersion compensation and with hardware dispersion balancing (10× objective lens in conjunction with the spectrometer compound lens of effective focal length of 37.5 mm)	30
Figure 3.6: PSF of a mirror at different depths with both software dispersion compensation and hardware dispersion balancing (10× objective lens in conjunction with the spectrometer compound lens of effective focal length of 37.5 mm)	31
Figure 3.7: DC band reduction with the HDBU	32
Figure 3.8: PSF peaks with 200 μm separations to determine the depth (μm) to pixel ratio for the 4× objective lens and an effective focal length = 100 mm spectrometer configuration	34
Figure 3.9: Determining the depth (μm) to pixel ratio from the mirror PSFs in Figure 3.8	34
Figure 3.10: OCT lateral resolution for the 10× objective lens configuration. (a) OCT setup to measure lateral resolution. (b) OCT cross-sectional image of a wafer using the 10× objective configuration. (c) Intensity profile of the wafer’s edge.	36
Figure 3.11: MPM setup to measure axial and lateral resolutions.....	37
Figure 4.1: Murine, piscine, porcine, and bovine corneal imaging setup	39
Figure 4.2: Human corneal imaging setup	40
Figure 4.3: Generation of the MPM cross-sectional image from a stack of <i>en face</i> images. (a) One <i>en face</i> image is taken. (b) A stack of <i>en face</i> images are taken. (c) The stack of XY images are combined post-processing to obtain a MPM 3D volume. (d) A XZ cross-sectional MPM image is reconstructed from the 3D volume.	42
Figure 4.4: Determining the epithelial and stromal RI and thicknesses. (a) OCT cross-sectional image. (b) MPM cross-sectional image.	44
Figure 4.5: OCT and MPM images of a murine cornea. (a) OCT cross-sectional image. (b) MPM cross-sectional image. L1 is the epithelium layer. L2 is the Bowman’s layer, stroma, Descemet’s membrane, and endothelium layers. (c) – (h) MPM <i>en face</i> images. (c) Anterior epithelium. (d) Posterior epithelium. (e) Junction between the epithelium and the stroma. (f) Anterior stroma. (g)	

Posterior stroma. (h) Descemet's membrane and Endothelium. Arrowheads point to the Descemet's membrane. (c) – (h) are 12 μm , 28 μm , 42 μm , 92 μm , 146 μm , and 160 μm below the surface of the cornea, respectively. TPEF signals are in red. SHG signals are in green. Scale bars are 50 μm . The red dashed rectangle in the OCT image marks the co-registered MPM imaging area..... 46

Figure 4.6: OCT and MPM images of a piscine cornea. (a) OCT cross-sectional image. (b) MPM cross-sectional image. S1 and S2 are the first and second stromal layers. (c) – (h) MPM *en face* images. (c) Anterior epithelium. (d) Posterior epithelium. (e) Junction between the epithelium and the stroma. (f) Stroma in S1. (g) Stroma in S2. (h) Descemet's membrane and endothelium. (c) – (h) are 4 μm , 28 μm , 44 μm , 69 μm , 253 μm , and 282 μm below the surface of the cornea, respectively. Double arrow marks the direction of the collagen fiber bundles. Scale bars are 50 μm . The red dashed rectangle in the OCT image marks the co-registered MPM imaging area... 48

Figure 4.7: OCT and MPM images of a human cornea . (a) OCT cross-sectional image. (b) MPM cross-sectional image. (c) – (h) MPM *en face* images. (c) Epithelium. (d) Bowman's layer. (e) – (g) Anterior to posterior stroma. (h) Descemet's membrane and endothelium. Yellow arrowheads point to regions of weaker SHG signal in the anterior stroma. Red arrowheads point to collagen micro-folds. Black arrowheads point to the Descemet's membrane. (c) – (h) are 42 μm , 68 μm , 110 μm , 340 μm , 680 μm , and 870 μm below the surface of the cornea, respectively. Scale bars are 50 μm . The red dashed rectangle in the OCT image marks the co-registered MPM imaging area..... 50

Figure 4.8: MPM *en face* images identifying the human Bowman's Layer. (a) Epithelium. (b) Posterior epithelium. (c) Bowman's layer. (d) – (e) Anterior stroma. (f) A typical stromal region. (a) – (f) are 26 μm , 34 μm , 42 μm , 50 μm , 60 μm , and 220 μm below the surface of the cornea, respectively. Scale bar is 50 μm 51

Figure 4.9: OCT and MPM images of a porcine cornea. (a) OCT cross-sectional image. (b) MPM cross-sectional image. (c) – (h) MPM *en face* images. (c) Anterior epithelium. (d) – (e) Junction between the posterior epithelium and the stroma. The Bowman's membrane is estimated as the region between the two arrowheads. (f) – (g) Anterior to posterior stroma. (h) Descemet's membrane and endothelium. (c) – (h) are 12 μm , 72 μm , 96 μm , 234 μm , 534 μm , and 772 μm below the surface of the cornea, respectively. Scale bars are 50 μm . The red dashed rectangle in the OCT image marks the co-registered MPM imaging area. 53

Figure 4.10: MPM *en face* images identifying the porcine Bowman’s Layer. Collagen structural comparison between the Bowman’s layer (a) – (b) and a typical stromal region (c) of a porcine cornea. (a) – (c) are 60 μm , 68 μm , and 190 μm below the surface of the cornea, respectively. Scale bar is 50 μm . The Bowman’s membrane is highlighted by the arrowheads. 54

Figure 4.11: OCT and MPM images of a bovine cornea. (a) OCT cross-sectional image. (b) MPM cross-sectional image. (c) – (k) MPM *en face* images. (c) Anterior epithelium. (d) Posterior epithelium. (e) Bowman’s layer. (f) – (g) Transition from the Bowman’s layer to the stroma. (h) Anterior stroma. (i) Posterior stroma. (j) Descemet’s membrane. (k) Endothelium. (c) – (k) are 36 μm , 136 μm , 154 μm , 164 μm , 174 μm , 478 μm , 898 μm , 934 μm , and 958 μm below the surface of the cornea, respectively. Scale bars are 50 μm . The red dashed rectangle in the OCT image marks the co-registered MPM imaging area. 56

Figure 4.12: RI results. (a) 6 murine samples. (b) 6 piscine samples. (c) 8 human samples. (d) 3 porcine samples. (e) 5 bovine samples. L1 is epithelium, L2 is the remaining corneal layers, and overall is the entire cornea thickness. 61

Figure 4.13: Comparison between the OCT and SHG signals of a human cornea and a bovine cornea. (a) – (d) OCT image, OCT intensity profile, SHG intensity profile, MPM cross-sectional image of a human cornea, respectively. (e) – (h) OCT image, OCT intensity profile, SHG intensity profile, and MPM cross-sectional image of a bovine cornea, respectively. L1 is the epithelium layer. L2 is the Bowman’s layer, stroma, Descemet’s membrane, and endothelium layers. Scale bars are 50 μm 64

Figure 5.1: Scanning electron microscope image of *Acanthamoeba castellanii* [50] 70

Figure 5.2: *Acanthamoeba castellanii* in the trophozoite and cyst stages [51]. (a) *Acanthamoeba castellanii* in the trophozoite stage. (b) *Acanthamoeba castellanii* in the cyst stage. 70

Figure 5.3: Patient with *Acanthamoeba Keratitis* [52]. 71

Figure 5.4: Slit-lamp microscope [54] 72

Figure 5.5: The inoculation equipment. (From left to right) Sterile needles and syringes; Two *Acanthamoeba castellanii* cultures; and an ex vivo corneal button stored inside Optisol corneal storage media. 76

Figure 5.6: The inoculation process..... 76

Figure 5.7: AK corneal imaging setup..... 77

Figure 5.8: Acanthamoeba cysts using the 40× objective lens. (a) TPEF channel. (b) SHG channel. Red arrows point to the Acanthamoeba cysts. Scale bar is 50 μm. 78

Figure 5.9: Keratocytes in the inoculated sample using the 40× objective lens. (a) TPEF channel. (b) SHG channel. Red arrows point to the keratocytes. Scale bar is 50 μm. 78

Figure 5.10: Acanthamoeba cysts using the 60× objective lens. (a) TPEF channel. (b) SHG channel. Red arrows point to the Acanthamoeba cysts. Yellow arrow points to leakage signal from the TPEF channel. Scale bar is 33 μm. 79

Figure 5.11: Control sample using the 60× objective lens. (a) TPEF channel. (b) SHG channel. Scale bar is 33 μm. 79

Figure 5.12: MPM stromal image of human corneas from Chapter 4. TPEF signal is in red and SHG signal is in green. Scale bar is 50 μm. 81

LIST OF ABBREVIATIONS

AK	Acanthamoeba keratitis
BCCDC	British Columbia centre for disease control
BS	Beam splitter
CCD	Charge-coupled device
CM	Confocal microscopy
FOV	Field of view
FWHM	Full width at half maximum
HDBU	Hardware dispersion balancing unit
MPM	Multiphoton microscopy
NA	Numeric aperture
NADH	Nicotinamide adenine dinucleotide phosphate
NIR	Near-infrared
OCT	Optical coherence tomography
OPEF	One-photon excited fluorescence
PCR	Polymerase chain reaction
PMT	Photomultiplier tube
PSF	Point spread function
RI	Refractive index
SD-OCT	Spectral-domain optical coherence tomography
SHG	Second harmonic generation
SNR	Signal to noise ratio
TD-OCT	Time-domain optical coherence tomography
THG	Third harmonic generation
Ti: sapphire	Titanium-sapphire
TPEF	Two-photon excited fluorescence
US	Ultrasound
VGH	Vancouver general hospital

ACKNOWLEDGEMENTS

First and foremost, I would like to thank my supervisor Dr. Shuo Tang for giving me the opportunity to work with her at the UBC Biophotonics laboratory and for providing me with valuable guidance and support.

I would also like to express my gratitude for the expertise and time provided by my collaborators at British Columbia Cancer Agency Research Centre, British Columbia Centre for Disease Control, and Vancouver General Hospital Eye Care Centre and Eye Bank.

I am grateful for the help provided to me by past and present members of the UBC Biophotonics lab. It has been a pleasure spending countless hours at the lab and at the office with such a great group of intellectuals. I would like to give special thanks to: Yifeng Zhou for teaching and training me to operate the combined MPM and OCT imaging system; Myeong Jin Ju for providing me with OCT technical assistances; and Dr. Shau Poh Chong for providing his knowledge and wisdom both academically and personally.

Finally, I would like to thank my family and friends for their support and encouragement throughout my studies.

Tom Yu Chia Lai

University of British Columbia

April 2014

CHAPTER 1: INTRODUCTION

In this thesis, a combined imaging system using multiphoton microscopy (MPM) and optical coherence tomography (OCT) is used to study the cornea. Firstly, it is used to simultaneously visualize and compare the morphology, and to characterize the thicknesses and the refractive index (RI) of five different species' corneas. Secondly, it is used to identify an induced parasitic infection in human corneas. As such, this chapter will provide a brief review of the anatomy and physiology of the cornea, the principles of MPM and OCT, and the motivation for the study. Finally, an outline of the whole thesis is presented.

1.1 BRIEF REVIEW OF THE ANATOMY AND PHYSIOLOGY OF THE CORNEA

The cornea is the outermost layer of the eye. It is a transparent, avascular and dome-shaped tissue that provides roughly two-thirds of the total refractive power in the eye [1]. Along with the aqueous humour and the lens behind it, the cornea focuses light onto the retina such that the eye can see clear images. In order to refract light properly, the cornea must remain transparent. Its clarity is the result of the organized anatomy and physiology of its five basic layers. From the anterior to the posterior side of the cornea, these layers are the epithelium, the Bowman's layer, the stroma, the Descemet's membrane, and the endothelium [2,3].

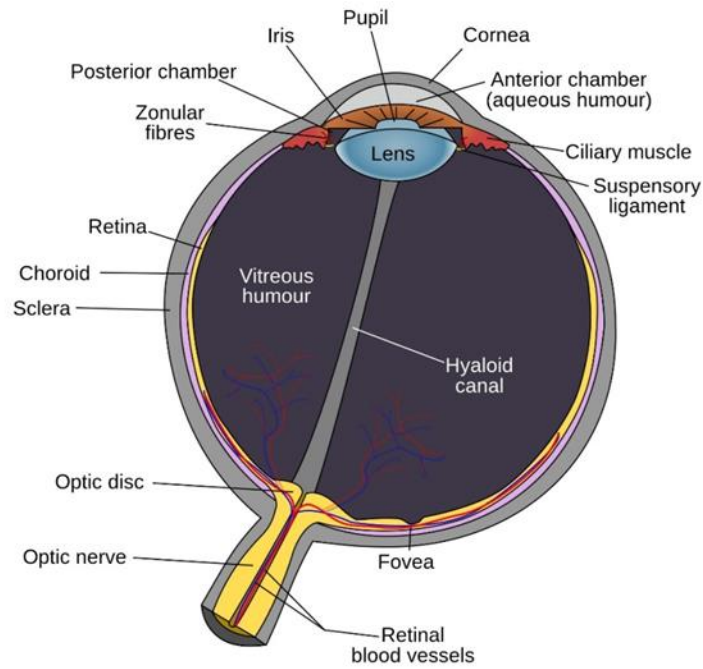


Figure 1.1: Anatomy of the eye [4].

1.1.1 EPITHELIUM

The epithelium is the outermost layer of the cornea. It consists of superficial polygonal cells, winged cells and basal columnar cells. The superficial epithelial cells provide a smooth surface to absorb oxygen and cell nutrients from the tears and then distribute these nutrients to the rest of the cornea. These cells along with the winged cells beneath them maintain tight junctions with their neighbours to prevent dust, fluids and microbes from entering the rest of the cornea. The basal columnar cells are the only cells in the epithelium capable of mitosis and as such they are the source of the winged and polygonal cells above.

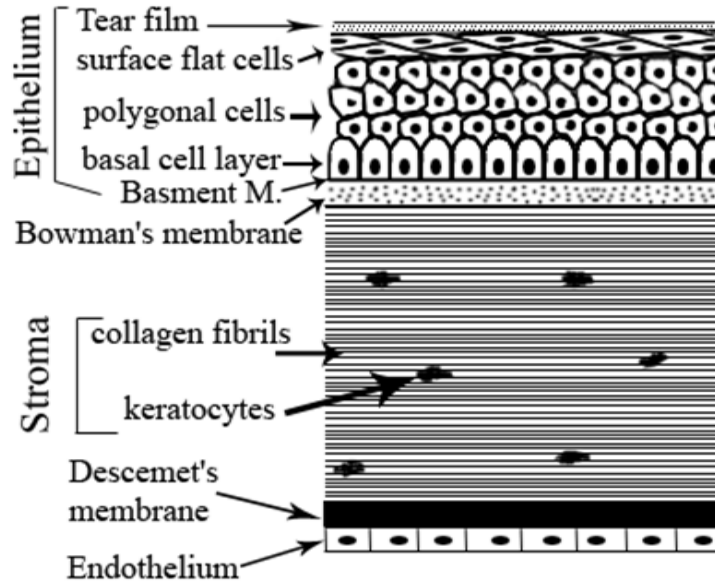


Figure 1.2: Anatomical structure of the cornea [5].

1.1.2 BOWMAN'S LAYER

The Bowman's layer lies beneath the epithelium. It is composed of a condensed layer of randomly arranged collagen fiber bundles [3,6]. These collagen fiber bundles are finer than, but continuous with, the collagen fiber bundles found in the stroma. The compact arrangement of these collagen fiber bundles provides mechanical strength and helps the cornea maintain its shape. However, not all species have a Bowman's layer [6].

1.1.3 STROMA

Below the Bowman's layer is the stroma. It is the thickest layer of the cornea and is composed of mainly type-I collagen fibers. These collagen fibers are arranged in parallel bundles called fibrils and these fibrils are arranged in layers called laminae [2,7]. The fibers have uniform diameters of 25-45 nm and are regularly arranged with respect to each other. This highly organized collagen network contributes to the transparency of the cornea [8]. The collagen arrangement also provides the cornea its rigidity and form. Apart from the collagen fibers, keratocytes also reside within the stroma. These are cells

that maintain the transparency of the stroma by healing its wounds and synthesizing its components. These cells remain dormant and reside at the anterior stroma until the onset of injury or inflammation [2].

1.1.4 DESCOMET'S MEMBRANE

Underneath the stroma is the Descemet's membrane which is a basement membrane made of a thin sheet of collagen. It is composed of primarily type-IV collagen and non-collagenous components such as fibronectin, laminin, and elastin [2,9]. It is very resistant to chemical agents and to pathological processes.

1.1.5 ENDOTHELIUM

As the innermost layer of the cornea, the endothelium maintains the stroma in deturgescence (correct hydration level) through a process of pumping and leaking fluids into and out of the stroma from the aqueous humour. Without this fluid regulation, the stroma would swell up and the cornea would become translucent or opaque [8]. Unlike the epithelial cells, the endothelial cells do not regenerate. Instead, they stretch to compensate for the dead cells. As such, the endothelium is composed of a thin, monolayer of cells which forms a honeycomb mosaic to minimize distribution in cell size and to maximize cell coverage.

1.2 BRIEF INTRODUCTION TO MPM

MPM is a nonlinear optical imaging technique that has subcellular resolution, deep penetration and optical sectioning capability [10]. Since its development over two decades ago, MPM has been widely used for non-invasive cellular imaging in life sciences and medicines. For instance, to name a few: immunologists have used it to

observe lymphocyte trafficking; neuroscientists have applied it to measure calcium dynamics in the brain; cancer researchers have employed it to study angiogenesis and metastasis; and embryologists have utilized it to visualize the development of hamster embryo. Basically, MPM uses multiple photons of lower energy to create an excitation that is normally produced by the absorption of a single photon of higher energy [11]. This process requires very intense excitation light in both spatial and temporal domains to be appreciably observed. Typically, MPM is performed under condition of tight focusing of a pulsed laser. MPM could give much better imaging contrast even at extended penetration depth as it excludes out-of-focus excitation of fluorophores. On top of that, MPM produces less photo-toxicity and photo-bleaching compared to the traditional linear fluorescence microscopy, since only fluorophores in the focal volume are excited. Our current MPM setup allows detection of two contrasts simultaneously: two-photon excited fluorescence (TPEF) and second harmonic generation (SHG). In particular, TPEF signal comes from intrinsic fluorophores such as nicotinamide adenine dinucleotide phosphate (NADH) and elastin. On the other hand, SHG signal comes from non-centrosymmetric molecules such as collagen [12]. MPM can be used to observe cells based on the autofluorescence from NADH found in the cell cytoplasm, and collagen morphology based on the SHG contrast. As such, it is very suitable for imaging the morphology of the entire cornea. The primary drawbacks of MPM are its slow point-scanning acquisition speed and its small field of view.

1.3 BRIEF INTRODUCTION TO OCT

OCT is based on the detection of single-backscattered light using the interferometry technique [12,13]. It provides cross-sectional view of the tissue by

detecting the interference between the reflected light from a sample arm and a reference arm. It has a resolution of ~10 microns and can achieve a penetration depth of a few millimetres, depending on the tissue transparency. Similar to other optical techniques, it is non-invasive, has no ionic-radiation and requires minimal sample preparation [14]. Since its development two decades ago, OCT has been used in medical fields such as urology, gynaecology, pulmonology, gastroenterology, cardiology and ophthalmology [14-20]. In the cornea, OCT can identify structural properties such as scars, foreign objects, superficial pathologies, irregular thicknesses, and epithelial and Descemet's membrane detachments [13]. The main disadvantages of OCT are its lack of biochemical specificity and cellular level resolution.

1.4 PROBLEM STATEMENT AND MOTIVATION

Visualization of the corneal morphology is useful in many ophthalmology applications, such as: analyzing the effects of contact lens wear and topical medications; identifying the type of infectious keratitis; and observing corneal ulcers, keratoconus, and the wound healing process [3,21]. The most common methods for corneal imaging include confocal microscopy (CM), MPM, and OCT. CM uses a light beam that passes through a source pinhole and an objective lens to illuminate the sample [3,21]. The reflected light returns through the objective lens and enters a photo-detector via a detection pinhole. The detection pinhole blocks the out-of-focus light and allows CM to have subcellular resolution and optical sectioning capability. CM has been used for *in vivo* imaging of the corneal morphology. However, it is limited to viewing cellular structures and nerves since it does not provide molecular contrast [22]. Also, it cannot visualize the Bowman's layer or the Descemet's membrane effectively.

In addition to the morphological visualization, the ability to quantitatively characterize the corneal thickness and RI is also of great importance in ophthalmology [8,12,23,24]. The measurement of the corneal thickness is needed in many clinical situations, such as the diagnosis of corneal degeneration, endothelial dysfunction, and stromal dystrophy. The measurement of the corneal RI is important for laser refractive surgery. The thickness and the RI of the cornea are also used as indicators for corneal hydration and intraocular pressure. A constant corneal hydration is necessary for the maintenance of its transparency. When the balance is disrupted, the cornea swells resulting in regions of varying RI, which causes the cornea to become cloudy and translucent. The intraocular pressure is an important parameter in the diagnosis and treatment of glaucoma.

Corneal thickness can be measured using CM, OCT, or ultrasound (US). CM examines the cornea by optically advancing through the entire cornea. By identifying the corneal boundaries, the thickness can be determined [25]. However, due to refraction, this method needs to be calibrated by examining a series of contact lenses with known thicknesses. There are many clinical devices to measure corneal thickness using OCT. However these devices need to assume a corneal group index in their calculations [26,27]. Ultrasound is the most common method clinically to measure corneal thickness [28]. However, it requires contact with the subject which may displace the tear film by 7-40 μm or lead to infections [29]. Ultrasound also uses an estimated value for the acoustic velocity which can differ between different devices and manufacturers.

RI can be measured using critical angle and OCT techniques. In a handheld refractometer, the incidence angle is tuned until the critical angle is reached, from which

the RI can be measured [30]. However, it can only measure the RI of the medium which is in direct contact with the optics. It cannot measure multilayered samples. Focus tracking using OCT has been reported for non-invasive RI measurements in tissues [31,32]. RI can be obtained by tracking the focus shift resulting from translating the focus of an objective along the optical axis within a medium. Rao et al. used the focus tracking method to estimate the RI of the zebrafish lens [31]. However, determining the front and rear surfaces of a multilayered biological sample by OCT can be difficult.

By using a combined MPM and OCT imaging system to acquire co-registered images of the cornea, each modality's limitations are reduced while their advantages are complemented. The OCT modality provides a full cross-sectional view of the cornea over a large field of view at fast speed. The OCT images are able to identify the major structural layers, such as the epithelium and the stroma, using the scattering contrast. In addition, the co-registered MPM images can identify the cellular and collagen fiber structures with high resolution at different depths of the cornea using the biochemically specific TPEF and SHG contrasts. The five corneal layers can be distinguished through the MPM *en-face* images. Furthermore, the thicknesses and the RI of the epithelium and the stroma can be calculated from the co-registered MPM and OCT images. The multimodal system has several advantages over existing methods. It provides both imaging and quantitative characterization of the cornea. This allows researchers and doctors to obtain more information for a more reliable analysis. It can be used to characterize biological tissues with multiple layers. Finally, it is label-free and requires no sample preparation which makes it possible to be implemented *in vivo*.

In this thesis, the MPM and OCT imaging system is used to image normal and diseased corneas. Firstly, the advantages and capabilities of the system are showcased through the visualization and quantitative characterization of normal corneas. Five different species were imaged to compare their morphologies, thicknesses and RI of the various corneal layers. The species studied are mouse, fish, human, pig and cow. Secondly, the MPM modality is used to study induced parasitic infection in *ex-vivo* human corneas. This study serves as important steps forward to bring the combined MPM and OCT technology to the clinical settings.

1.5 ORGANIZATION OF THE THESIS

Chapter 2: The principles of MPM and OCT, starting from the fundamentals of TPEF, SHG, and interferometry, are presented. Key OCT properties are introduced. Advantages of MPM and OCT are also discussed.

Chapter 3: The combined MPM and OCT system is introduced. Objective lens and spectrometer configurations used for Chapter 4 are presented. A hardware dispersion balancing unit is added to the system to minimize the dispersion mismatch between the sample and reference arms of the OCT modality. The benefits and effects of the hardware dispersion balancing unit are examined. Characterizations of the MPM and OCT system are also performed and presented.

Chapter 4: Demonstrations of the multimodal system capabilities are presented in this chapter through the visualization and quantitative characterization of five

different species' corneas. Morphologies of the various corneal layers of the murine, piscine, human, porcine, and bovine corneas are observed and compared. Refractive indices and thicknesses of the major corneal layers are also determined from the co-registered MPM and OCT images.

Chapter 5: In this chapter, *ex vivo* human corneas are inoculated with *Acanthamoeba castellanii* and imaged with the MPM system to study and to build the groundwork for future *Acanthamoeba* keratitis diagnosis.

Chapter 6: The final chapter concludes the thesis and provides discussion for possible future work.

CHAPTER 2: PRINCIPLES OF MPM AND OCT

2.1 PRINCIPLES OF MPM

When light interacts with a material, the material will generate a polarization response. In general, the induced polarization of a material can be expressed as [33]:

$$P = \chi^{(1)}E^1 + \chi^{(2)}E^2 + \chi^{(3)}E^3 + \dots \quad (2.1)$$

In this expression, P is the induced polarization, $\chi^{(1)}$ is the linear susceptibility, $\chi^{(n)}$ is the n^{th} -order nonlinear susceptibility for $n>1$, and E is the electric field vector. The first term describes normal linear interactions such as the absorption and the reflection of light. SHG appears in the second term ($n=2$) while third harmonic generation (THG) and TPEF occurs in the third term ($n=3$). Higher-order susceptibilities are usually very small. MPM is a form of laser scanning microscopy that uses pulsed near infrared (NIR) wavelength light to create non-linear excitations within the specimen being observed [10]. In this work, the two imaging contrast mechanisms, TPEF and SHG, are utilized.

2.1.1 TWO-PHOTON EXCITED FLUORESCENCE (TPEF)

In the energy diagrams shown in Figure 2.1, the ground state S_0 and the first excited state S_1 will be used to explain one-photon excitation fluorescence (OPEF) and TPEF. In OPEF, Figure 2.1(a), a single photon of sufficient energy excites an electron to an excited state, S_1 . The electron then goes to the lowest vibrational energy level of the excited state via relaxation of the energy. When the electron returns from the excited state to the ground state, the energy is released as an emission of a fluorescence photon. In TPEF, Figure 2.1(b), two photons are absorbed simultaneously to cause the electron to transfer to the excited state. Specifically, the first photon excites the electron to an

intermediate virtual state and the second photon excites the electron to the excited state within a few femtoseconds of the first photon [34,35]. The two photons absorbed in TPEF have roughly half the energy (twice the wavelength) of the photon absorbed in OPEF. In biological tissues, intrinsic fluorophores such as NADH, elastin, flavins, and melanin produce TPEF signals when being excited in the infrared region. Since NADH exists in the cell cytoplasm, TPEF can be used to image cellular structures.

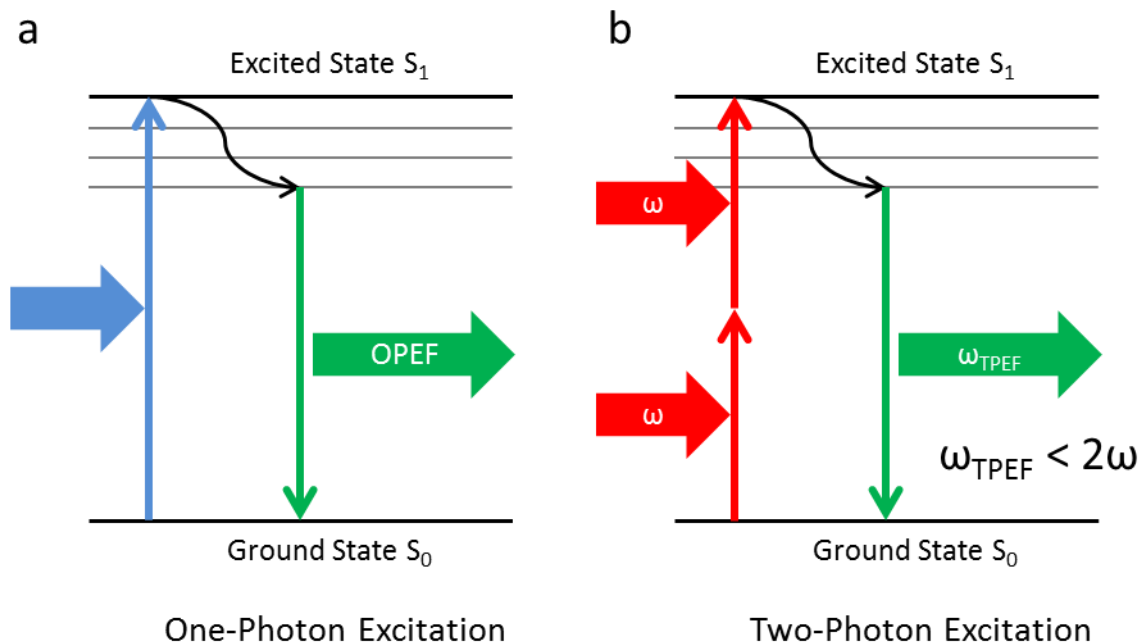


Figure 2.1: OPEF and TPEF excitation energy diagram. (a) OPEF excitation energy diagram. (b) TPEF excitation energy diagram.

2.1.2 SECOND HARMONIC GENERATION (SHG)

Unlike TPEF, SHG does not require real absorption of the photons. Instead, as shown in Figure 2.2, two photons with the same frequency interact with a nonlinear material to cause frequency doubling, a process that generates a new photon with exactly twice the energy (half the wavelength) of the initial photons [36]. This phenomenon requires intense laser light passing through a highly polarizable material with a

noncentrosymmetric molecular organization [33]. In biological tissues, SHG is often used to image collagen, which is a primary structural protein in connective tissues in animals. It is a primary component of cartilage, bone, tendon, skin and cornea [37].

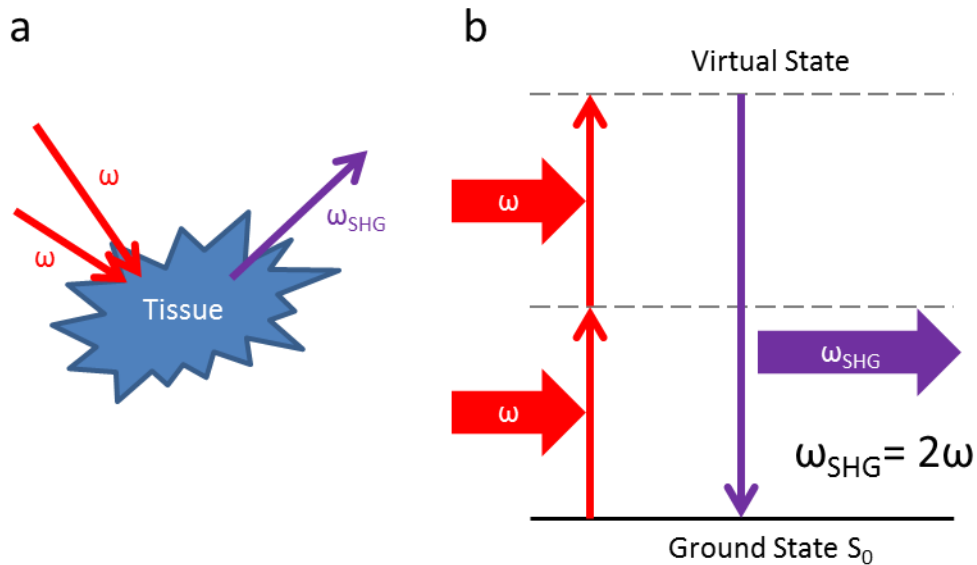


Figure 2.2: The SHG process. (a) Two photons with the same frequency interact with a tissue to generate a new photon with twice the energy and half the wavelength of the initial photons. (b) SHG excitation energy diagram

2.1.3 ADVANTAGES OF MPM

A high photon flux is required in order to produce observable TPEF and SHG signals. This can be achieved by focusing the excitation light in both the temporal and spatial domains. As such, MPM uses a pulsed laser and an objective lens with high numerical aperture (NA) to produce TPEF and SHG at the focal volume. This gives inherent optical sectioning capability, mainly because TPEF and SHG have a quadratic dependence on the illumination intensity. Thus the excitation is localized which results in high resolution in all 3 dimensions [33,38] and minimal excitation of out-of-focus fluorophores. Another significant advantage of localized excitation is that wide-field detection can be employed without the need of pinhole apertures to reject out-of-focus

fluorescence such as used by confocal fluorescence microscopy. Figure 2.3 compares the excitation profiles of the OPEF and TPEF respectively. Penetration depth is also increased in MPM because the excitation photons are usually in the NIR wavelength range which experiences much less scattering in biological tissues. Furthermore, phototoxicity in tissue is minimized due to the lack of endogenous absorbers at NIR wavelength as well as the localization of the excitation. Finally, MPM produces two biochemically specific contrasts allowing the visualization of common tissue structures such as cells and collagen without the need of exogenous staining.

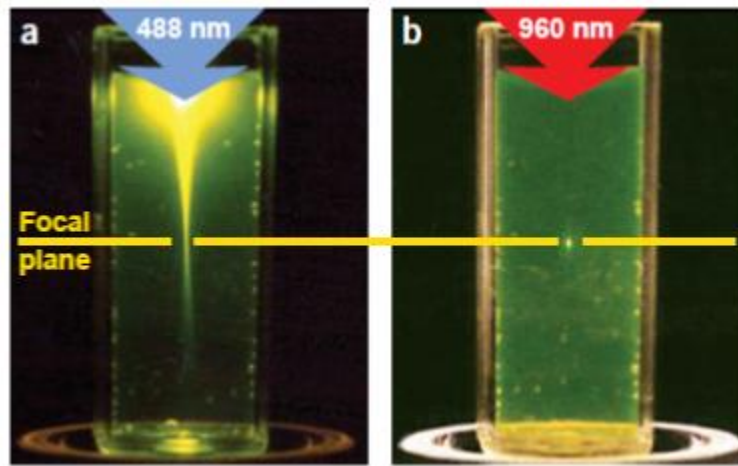


Figure 2.3: Localization of excitation by two-photon excitation [10]. (a) One-photon excitation of fluorescein by focused 488 nm light (0.16 NA). (b) Two-photon excitation using focused (0.16 NA) femtosecond pulses of 960 nm light.

2.2 PRINCIPLES OF OCT

OCT is based on low-coherence interferometry techniques. The basic optical set up for an OCT system involves a Michelson interferometer, as shown in Figure 2.4. A low coherent light is split by a beam splitter into a sample beam and a reference beam. The sample beam penetrates the sample and is reflected, while the reference beam is reflected by the reference mirror. The two reflected beams are recombined at the beam

splitter and then directed into a detector. The superimposed beams create interference patterns and are recorded by the detector. The recorded intensity is given by the expression [20,39]:

$$I \propto A_r^2 + A_s^2 + 2A_rA_s \cos(2k\Delta l) \quad (2.2)$$

In Equation 2.2, I is the intensity detected, k is the angular wavenumber which is equal to $2\pi/\lambda$, Δl is the pathlength mismatch between the two arms, A_r and A_s are the amplitudes of the reflected electric fields from the reference and sample mirrors, respectively. The first two terms in the expression are the DC terms. The first term is measurable and can be subtracted in post-processing while the second term is very small and can be neglected. The third term corresponds to the cross-correlation term which contains the interference information. It depends on the pathlength mismatch, Δl , between the sample arm and the reference arm [39]. The frequency of the cross-correlation term changes as Δl changes. A higher frequency corresponds to a larger Δl . By measuring the cross-correlation frequency, the depth location of the reflection in the sample can be determined.

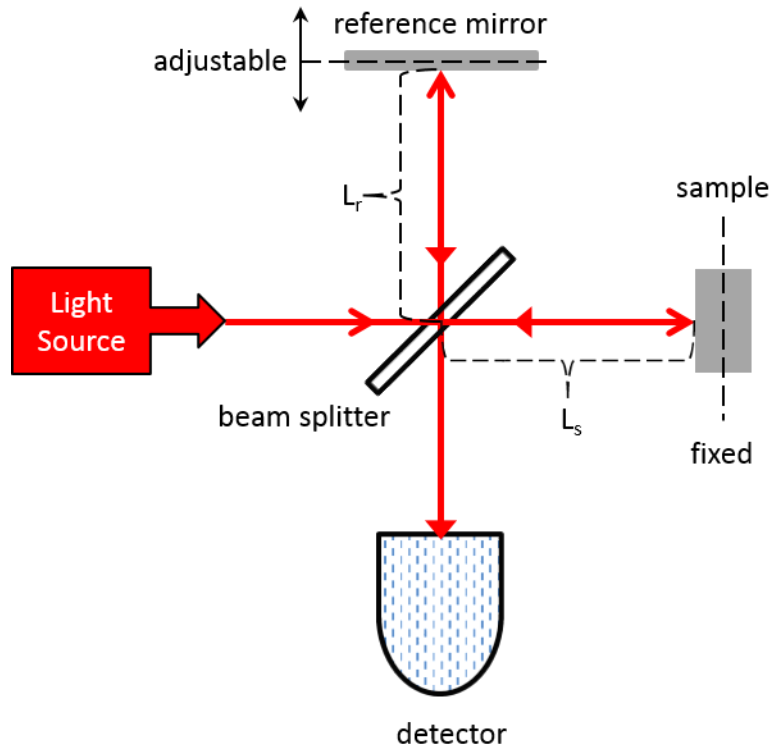


Figure 2.4: Michelson interferometer. L_r and L_s are the reference arm length and sample arm length respectively.

In time-domain optical coherence tomography (TD-OCT), the intensity received by the detector corresponds to the amount of reflection from the sample at a specific depth [39]. This depth is controlled by the reference arm length since the interference fringes only appear when the pathlength difference between the two arms is within the coherence length of the light source. By stepping through different reference arm lengths, TD-OCT can obtain the intensity of the reflected light as a function of the sample depth. High intensities result from interfaces in the sample with large refractive index differences.

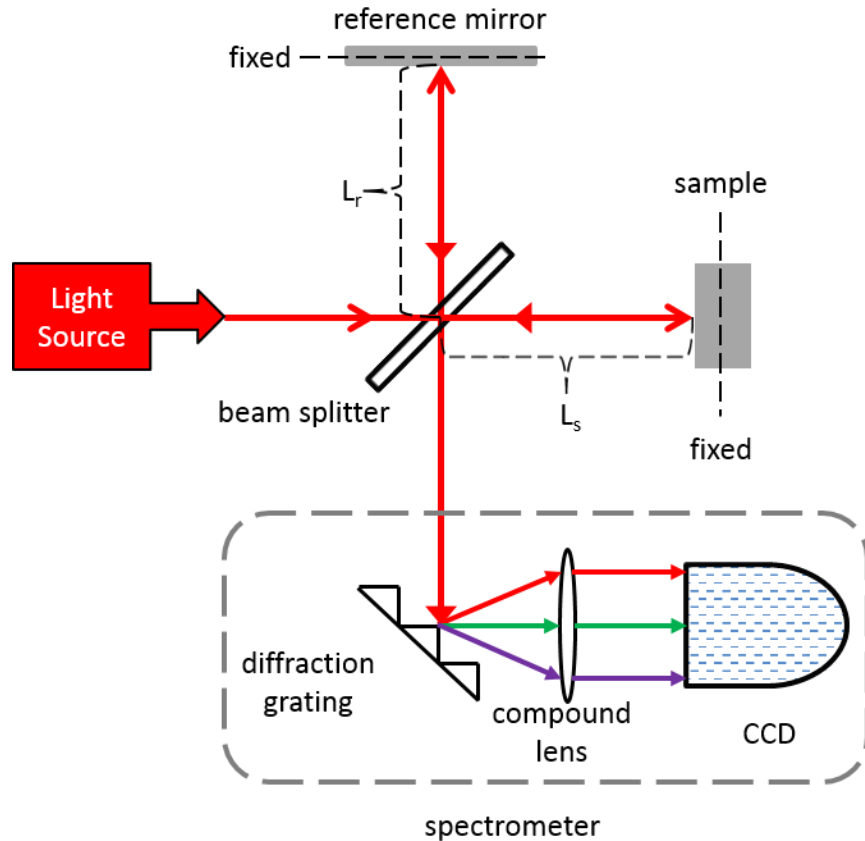


Figure 2.5: SD-OCT

Since the detected signal is made up of all the reflected monochromatic waves from the sample arm and the reference arm, the intensities at different wavelengths can be separated by a diffraction grating and focused onto a charge-coupled device (CCD) camera by a compound lens, as shown in Figure 2.5. Together, the diffraction grating, the compound lens and the CCD camera form a spectrometer. As shown in Equation 2.2, the inference signal is encoded in the angular wavenumber k -domain; while the detected signal using the diffraction grating and line camera is encoded in the λ -domain; hence proper resampling of the fringe signal is required. By converting the intensities as a function of wavelengths, $I(\lambda)$, to intensities as a function of one over wavelengths, $I(1/\lambda)$, then interpolating the data to obtain evenly sampling intervals, Fourier transforms can be

applied to obtain the reflectivity intensities as a function of the depth in pixels on the CCD detector, $I(\text{pixels})$. This pixel depth can be converted to the actual sample depth by a simple calibration process. Depth information is encoded in the frequency of the fringe signal. For instance, high frequency oscillations in the k -domain ($1/\lambda$) corresponds to reflections at deeper sample locations, as shown in Figure 2.6. This method is the basis for spectral domain optical coherence tomography (SD-OCT) which is the type of OCT used in my thesis.

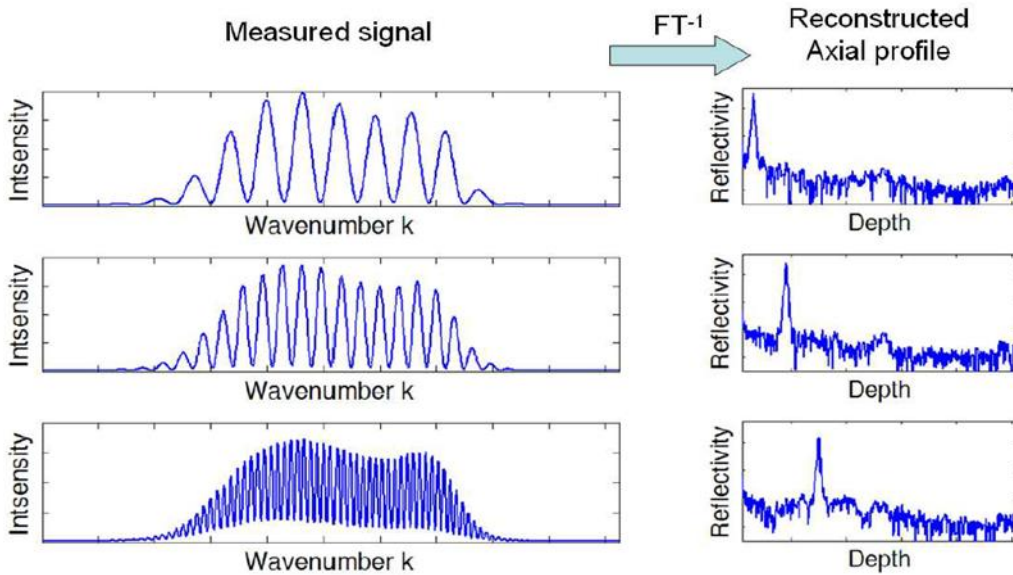


Figure 2.6: Measured interference fringe signal and reconstructed axial profile of reflectivity in SD-OCT [39]. Reconstructed axial profiles $I(\text{pixels})$ at different depths (right) from their measured signals $I(k)$ (left).

2.2.1 IMAGE DEPTH

The maximum imaging depth of an OCT system is determined mainly by its source as well as its spectrometer design. The maximum imaging depth can be expressed as a function of the pixel spacing and the number of pixels on the CCD camera [40]:

$$d \leq \Delta s \frac{N}{2} \quad (2.3)$$

where d is the maximum imaging depth, Δs is the pixel spacing in the depth domain and N is the number of pixels on the CCD camera. Base on the Nyquist-Shannon sampling theorem, in order to achieve source-limited axial resolution, the sampling rate must be at least two times larger than the maximum frequency of the oscillation:

$$\Delta s \leq \frac{\Delta z}{2} \quad (2.4)$$

where Δz is the axial resolution. Combining Equations 2.3 and 2.4 gives:

$$d \leq \frac{\Delta z}{4} N \quad (2.5)$$

Equation 2.5 shows that to increase the OCT's maximum imaging depth while maintaining source-limited axial resolution, a CCD camera with more pixels is needed. However, the imaging depth can also be increased by sacrificing the axial resolution.

2.2.2 *DISPERSION MISMATCH*

Dispersion is a phenomenon in which the phase velocity of a wave depends on its frequency. As light passes through optical components, different frequencies of the light propagate at different velocities. Since the sample and reference arms contain different optical components, dispersion mismatch occurs and ultimately reduces the OCT image quality. Dispersion mismatch can be rectified either through software dispersion compensation or hardware dispersion balancing. In the current setup, software dispersion compensation was developed by a previous master student, Kenny K. H. Chan. Without software dispersion compensation, the reconstructed axial profile of a mirror sample results in a broadened point spread function (PSF) (blue curve in Figure 2.7). After software dispersion compensation, the reconstructed axial profile becomes a narrow PSF (red curve in Figure 2.7). However, compared to uncompensated PSF profile, a larger DC band occurs in the axial profile thus reducing the observable imaging depth of the

system. The DC band is a result from the Fourier transformations in the OCT image reconstruction. By using hardware dispersion balancing, a narrow PSF can be achieved without the DC band artifact. Hardware dispersion balancing is implemented by me and will be discussed in the follow chapter. Since the mirror can be regarded as a single reflecting surface, its ideal PSF would be a delta function. As such, the full-width-half-maximum (FWHM) of the PSF from the reconstructed axial profile of a mirror describes its axial resolution. Since the z-domain axial profile is plotted in decibel scaling, the FWHM is taken as the 3dB width of the PSF peak. The axial resolution and the reduction of the DC band will be used to evaluate the effectiveness of the hardware dispersion balancing component in the following chapter.

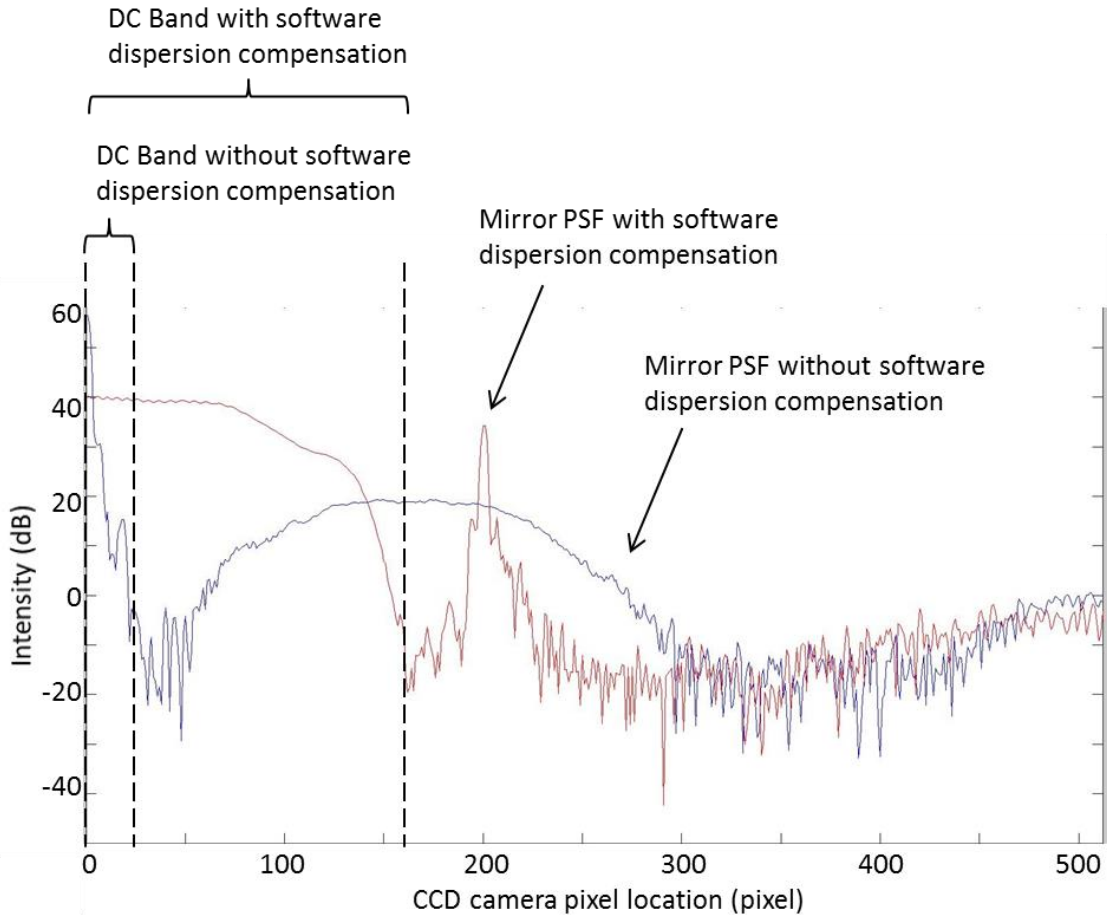


Figure 2.7: PSF of a mirror sample with and without software dispersion compensation. Intensity (decibels) versus depth (pixels) of the reconstructed axial profiles of a mirror sample with and without software dispersion compensation in red and in blue respectively (No hardware dispersion compensation components).

2.2.3 SENSITIVITY FALL-OFF

As the image depth increases, the cross-correlation frequency approaches the Nyquist sampling limit of the CCD camera and the interference intensity falls off. The attenuation of the signal as OCT depth increases is the sensitivity fall-off, which is one of the main disadvantages of SD-OCT. The sensitivity fall-off will be used to evaluate the effectiveness of the hardware dispersion balancing unit in the following chapter.

2.2.4 ADVANTAGES OF OCT

Since SD-OCT simultaneously acquires the entire depth information at a sample location through its spectrometer, OCT image acquisition does not require depth scanning and thus high imaging speed is achievable. This allows real-time *in vivo* tissue imaging, which is more susceptible to motion artifacts. Furthermore, by using NIR light, deep penetration in scattering medium such as biological tissues can be achieved. Therefore, OCT has been used for imaging transparent to scattering tissues such as cornea and skin. Finally, since OCT is based on the backscattered signal, it provides a different contrast mechanism from TPEF and SHG.

CHAPTER 3: SYSTEM

The combined MPM and OCT imaging system has been built and tested by Dr. Shuo Tang, and a previous master's student, Yifeng Zhou. Characterization of the system was done by Yifeng Zhou with my help. The OCT hardware dispersion balancing unit is implemented by me. Finally, I have modified the spectrometer for two different imaging depth capability for my corneal imaging applications.

3.1 SYSTEM OVERVIEW

The schematic of the MPM/OCT system is shown in Figure 3.1. A sub-10 fs Ti: Sapphire laser (Fusion PRO 400, Femtolasers) with a centre-wavelength of 800 nm, a bandwidth of 120 nm and a coherence length of 2.3 μm in air is used as the light source for both the MPM and the OCT imaging. The laser light passes through a prism-based dispersion pre-compensation unit before entering a 50/50 beam splitter. The dispersion pre-compensation unit is to compensate for pulse broadening due to dispersion from the objective lens and other optics in the beam path. The beam splitter divides the light into a sample beam and a reference beam.

For MPM imaging, the sample beam illuminates the sample through two galvanometer mirrors (Cambridge Technology), a pair of beam expansion lenses, and an objective lens mounted on a piezo-scanner (MIPOS 500, Piezosystem Jena). The galvanometer mirrors and the piezo-scanner are used to achieve transversal and axial scanning, respectively. The focused light from the objective lens excite both the TPEF and SHG signals in the sample. The generated signals are collected in the backward direction and separated by dichroic mirrors into their respective photomultiplier tubes (PMTs).

For OCT imaging, the backscattered beam from the sample combines with that from the reference mirror through the beam splitter into the spectrometer. The reference beam passes through a hardware dispersion balancing unit (HDBU) which will be discussed in a following section. The detected spectral signals are used to form the OCT images.

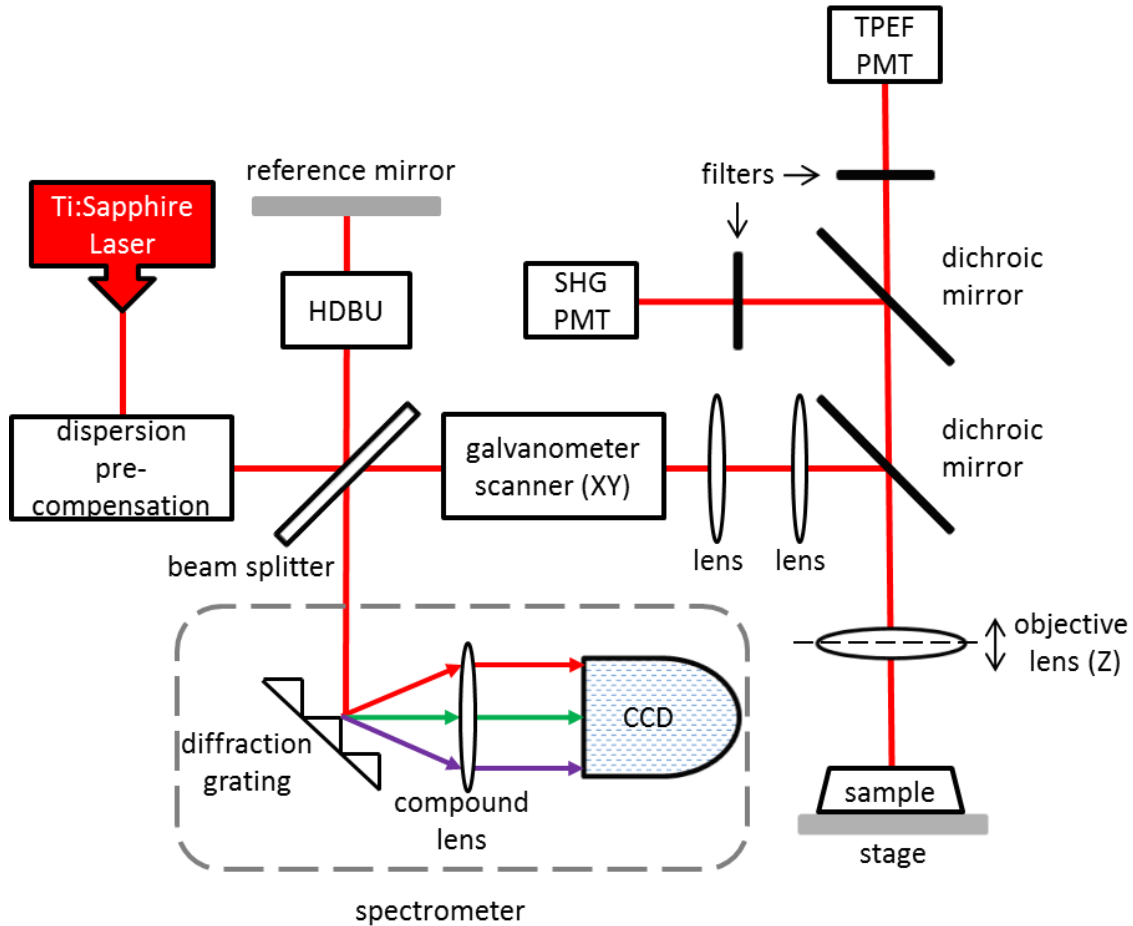


Figure 3.1: Experimental setup of the combined MPM/OCT imaging system. PMT: photomultiplier tube. HDBU: hardware dispersion balancing unit.

3.2 OBJECTIVE LENS

A 40× water immersion objective lens (LUMPlanFL N, Olympus, NA=0.8) is used for the MPM imaging in chapter 4. In chapter 5, a 60× water immersion objective lens (UPlanSApo, Olympus, NA=1.2) is used in conjunction with the 40× objective lens.

For OCT imaging, a 10× objective lens (MPlanFL N, Olympus, NA=0.3) is used to image the murine and piscine corneas in Chapter 4 while a 4× objective lens (Plan N, Olympus, NA=0.1) is used to image the human, porcine and bovine corneas. The 4× objective lens is used to image the thicker samples because it has a smaller NA.

3.3 SPECTROMETER

The spectrometer shown in Figure 3.1 is composed of a diffraction grating (Wasatch Photonics, 1200 lines/mm), a compound lens and a line CCD camera (AViiVA SM2 CL, E2V, 1024 pixels, $14 \times 14 \mu\text{m}^2$ pixel size). The OCT lateral resolution is dependent on the numerical aperture of the objective lens while the axial resolution is dependent on the coherence length of the laser source and the spectrometer design. A compound lens with a longer effective focal length in the spectrometer can increase the maximum imaging depth. However, when the dispersed laser spectrum exceeds the sampling range of the CCD camera, the increase in the maximum imaging depth will have a trade-off of a decrease in axial resolution. In this study, two spectrometer and objective lens configurations were used to image the thinner and thicker corneas. An effective $f = 37.5$ mm achromatic compound doublet lens is used in conjunction with the 10× objective lens to image the murine and piscine corneas in Chapter 4 while an effective $f = 100$ mm compound lens is used in conjunction with the 4× objective lens to image the thicker samples, namely the human, porcine and bovine corneas. The objective lens and compound lens configuration for different specimen is summarized in Table 3.1.

Specimen	Objective lens		Effective focal length of the spectrometer compounds lens
	MPM	OCT	
Murine	40×, NA= 0.8	10×, NA= 0.3	f = 37.5 mm
Piscine	40×, NA= 0.8	10×, NA= 0.3	f = 37.5 mm
Human	40×, NA=8 60×, NA = 1.2 (Chapter 5)	4×, NA= 0.1	f = 100 mm
Porcine	40×, NA= 0.8	4×, NA= 0.1	f = 100 mm
Bovine	40×, NA= 0.8	4×, NA= 0.1	f = 100 mm

Table 3.1: Objective lens and spectrometer configuration for MPM and OCT

3.4 HARDWARE DISPERSION BALANCING UNIT

Since software dispersion compensation increases the DC band and ultimately reduces the maximum OCT imaging depth, a hardware dispersion balance unit is introduced in the reference arm. Ideally, the sample and reference arms should contain the same optics to reduce any dispersion mismatch. However, having duplicates of the OCT objective lens is costly and inefficient. Therefore, N-BK7 glass is chosen as an alternative to balance the dispersion mismatch. The thickness of the glass needed is first estimated by introducing one 1-mm-thick N-BK7 glass slide at a time into the reference arm and observing the PSF of a mirror sample. When the PSF is at its minimum width, the dispersion mismatch is minimized. The PSF of a mirror sample using the 10× objective lens for one to seven N-BK7 glass slides are shown in Figure 3.2. The graphs show the reconstructed axial profile of the mirror PSF in black, and the interference fringes in blue. The axes are intensity in the y-axis and depth (in pixels) in the x-axis. In this case, the thickness of glass needed is estimated to be around 5 mm (5 glass slides) since it produces the narrowest PSF. For the 4× objective lens, an estimation of 13 mm of glass is needed. In order to provide dispersion balancing for both OCT objective lenses, a

prism-based dispersion balancing unit is implemented in the reference arm. The prism-based HDBU is shown in Figure 3.3.

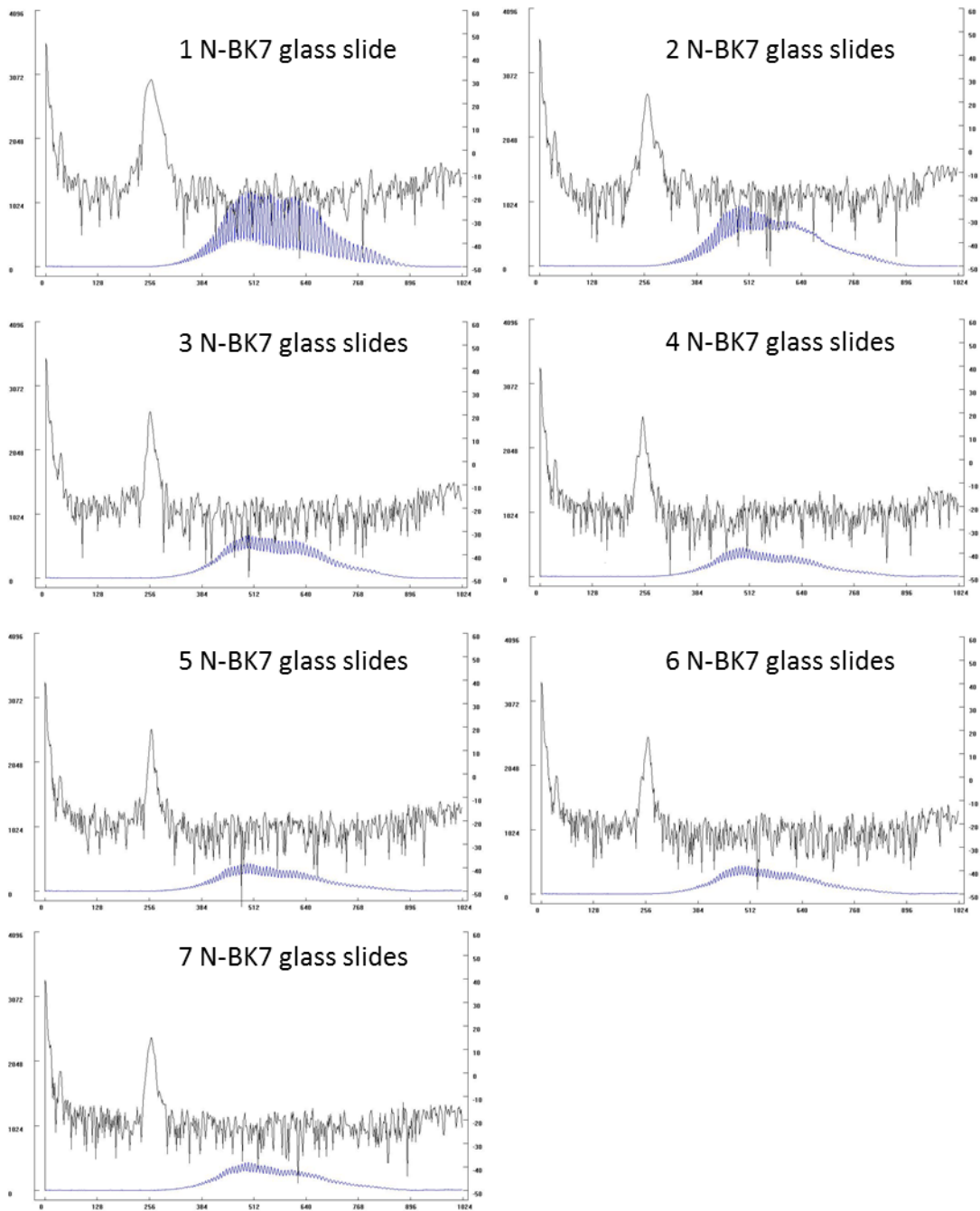


Figure 3.2: Mirror PSF for 1-7 N-BK7 glass slides (10× objective lens). The 3dB width of the PSF decreases until 5 N-BK7 glass slides then increases. Therefore the amount of N-BK7 glass needed to balance the OCT reference and sample arms is around 5 mm.

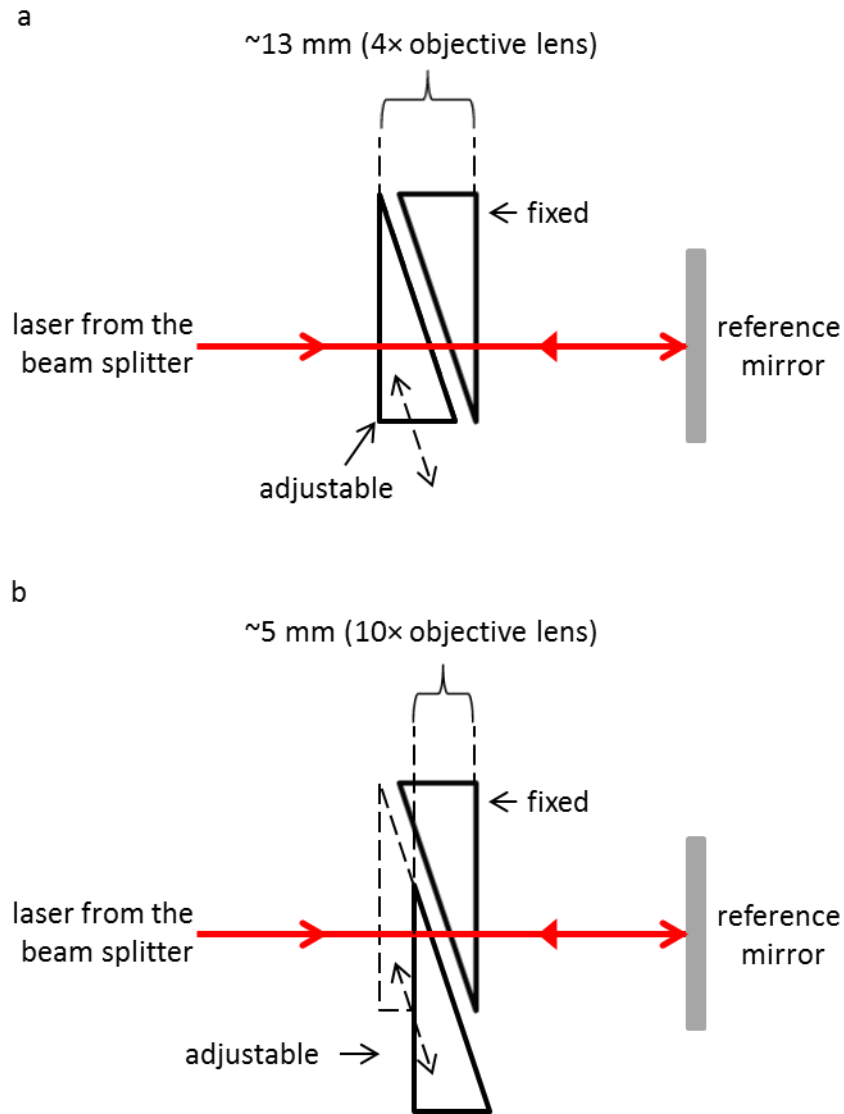


Figure 3.3: Hardware dispersion balancing unit. (a) By arranging the adjustable glass prism, the total thickness of N-BK7 glass traveled by the reference beam can be set to balance the dispersion mismatch for the 4× objective lens. (b) By moving the adjustable glass prism, the thickness can be decreased to accommodate the thickness needed to balance the dispersion mismatch for the 10× objective lens.

The axial resolution at different depths for a mirror sample can be measured by translating the reference mirror along the optical axis. The PSFs for the 10× objective lens without software dispersion compensation or hardware dispersion balancing is shown in Figure 3.4. The signal to noise ratio (SNR), axial resolutions and sensitivity fall-offs are summarized in Table 3.2.

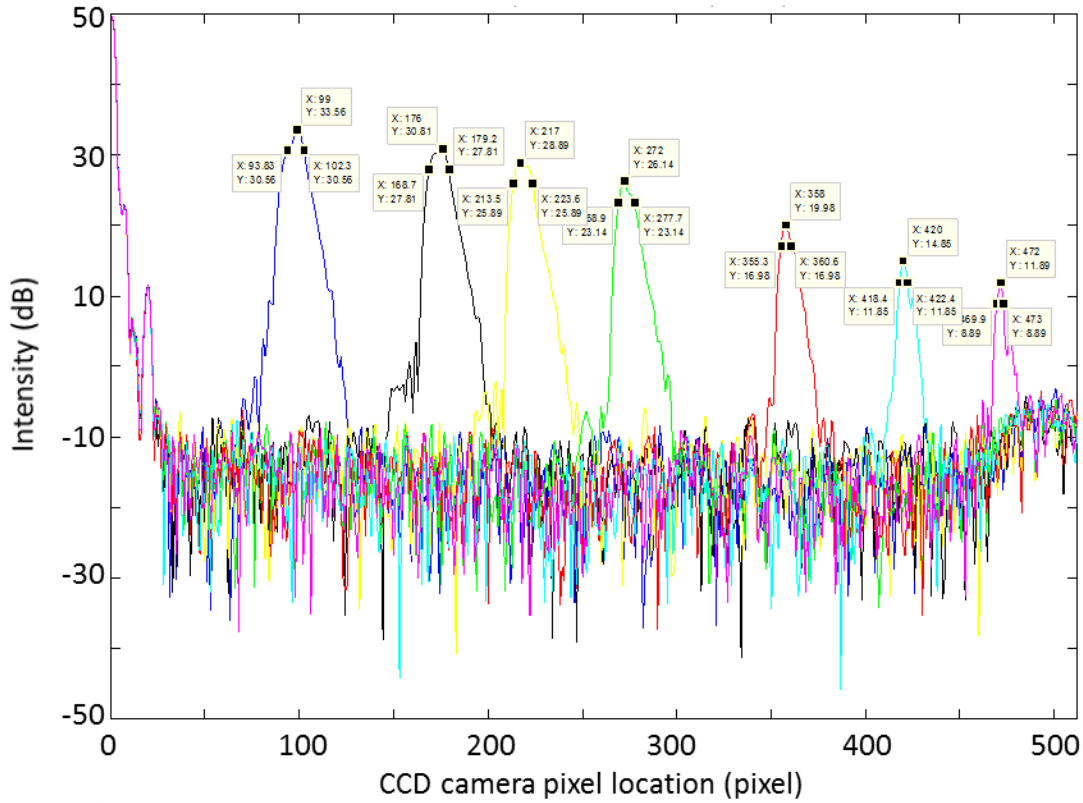


Figure 3.4: PSF of a mirror at different depths without software dispersion compensation and without hardware dispersion balancing (10× objective lens in conjunction with the spectrometer compound lens of effective focal length of 37.5 mm)

Peak #	Pixel #	Depth (μm)	SNR (dB)	Axial Resolution (μm)	Sensitivity Fall-off (dB)
1	99	118	43.56	10.09	0
2	176	210	40.81	12.51	2.75
3	217	359	38.89	12.03	4.67
4	272	324	36.14	10.48	7.42
5	358	427	29.98	6.31	13.58
6	420	500	25.85	4.77	17.71
7	472	562	21.89	3.69	21.67

Table 3.2: SNR, axial resolution and sensitivity fall-off without software dispersion compensation and without hardware dispersion balancing (10× objective lens in conjunction with the spectrometer compound lens of effective focal length of 37.5 mm)

With the introduction of the HDBU, the SNR, the axial resolution and the sensitivity fall-offs are all improved, as shown in Figure 3.5 and in Table 3.3.

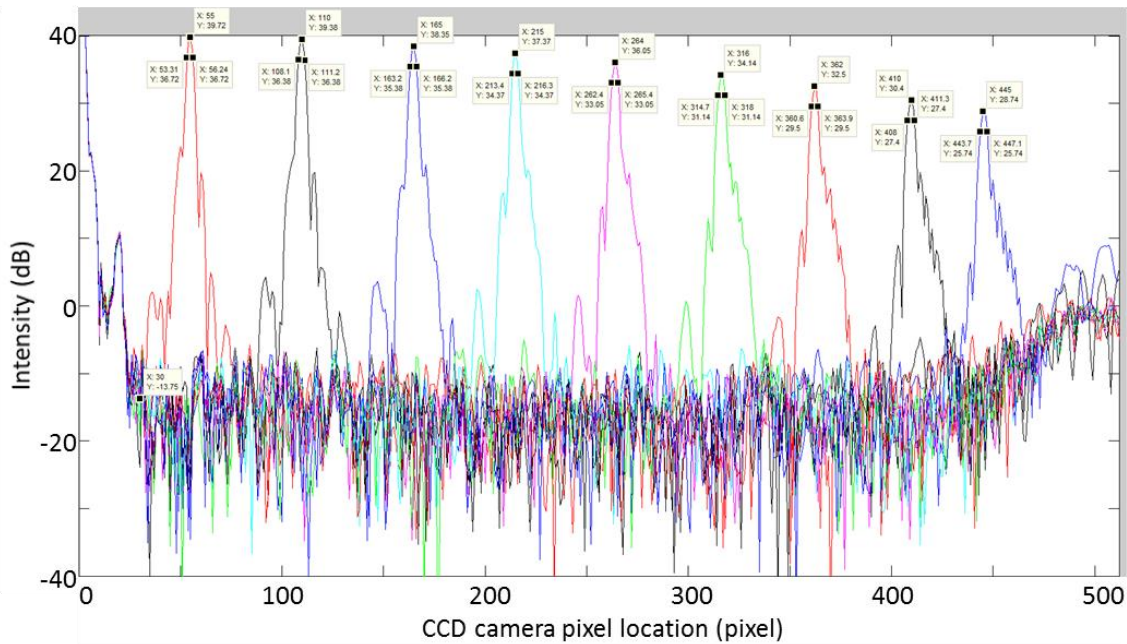


Figure 3.5: PSF of a mirror at different depths without software dispersion compensation and with hardware dispersion balancing (10× objective lens in conjunction with the spectrometer compound lens of effective focal length of 37.5 mm)

Peak #	Pixel #	Depth (μm)	SNR (dB)	Axial Resolution (μm)	Sensitivity Fall-off (dB)
1	55	66	49.72	3.49	0
2	110	131	49.38	3.69	0.34
3	165	197	48.35	3.57	1.37
4	215	256	47.37	3.46	2.35
5	264	315	46.05	3.57	3.67
6	316	376	41.14	3.93	8.58
7	362	431	42.5	3.93	7.22
8	410	488	40.4	3.93	9.32
9	445	530	38.74	3.93	10.98

Table 3.3: SNR, axial resolution and sensitivity fall-off without software dispersion compensation and with hardware dispersion balancing (10× objective lens in conjunction with the spectrometer compound lens of effective focal length of 37.5 mm)

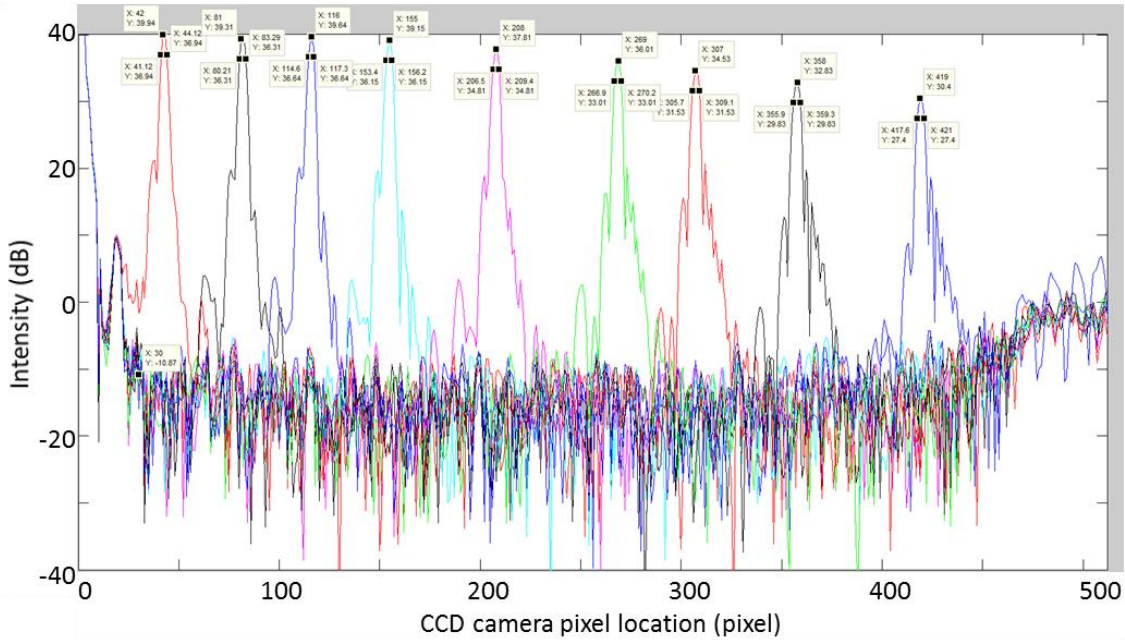


Figure 3.6: PSF of a mirror at different depths with both software dispersion compensation and hardware dispersion balancing (10× objective lens in conjunction with the spectrometer compound lens of effective focal length of 37.5 mm)

Peak #	Pixel #	Depth (μm)	SNR (dB)	Axial Resolution (μm)	Sensitivity Fall-off (dB)
1	42	50	49.94	3.57	0
2	81	97	49.31	3.67	0.63
3	116	138	49.64	3.22	0.30
4	155	185	49.15	3.34	0.79
5	208	248	47.81	3.46	2.13
6	269	320	46.01	3.93	3.93
7	307	366	44.53	4.05	5.41
8	358	427	42.83	4.05	7.11
9	419	499	40.40	4.05	9.54

Table 3.4: SNR, axial resolution and sensitivity fall-off with both software dispersion compensation and hardware dispersion balancing (10× objective lens in conjunction with the spectrometer compound lens of effective focal length of 37.5 mm)

The SNR, the axial resolution and the sensitivity fall-offs did not change much with the addition of the software dispersion compensation, as shown in Figure 3.6 and in Table 3.4. With the HDBU, with or without software dispersion compensation yields similar SNR of 40-50 dB and axial resolutions of around 3.5-4 μm . For both cases the

sensitivity fall-off is ~ 9 dB over 500 μm depth. As such we can conclude that the HDBU can balance the dispersion mismatch quite well and software dispersion compensation is no longer necessary.

The HDBU improves the SNR, the axial resolution and the sensitivity fall-off. Furthermore, it minimizes the DC band in the reconstructed image thus increasing the maximum OCT imaging depth. Figure 3.7 shows a comparison of the DC band for an OCT cross-sectional image of a coverslip with software dispersion compensation and another image with hardware dispersion balancing. The two horizontal lines in each image correspond to the top and bottom surfaces of the coverslip. The lines in the right image of Figure 3.7 are slightly slanted because the coverslip was not flat relative to the laser beam from the objective lens.

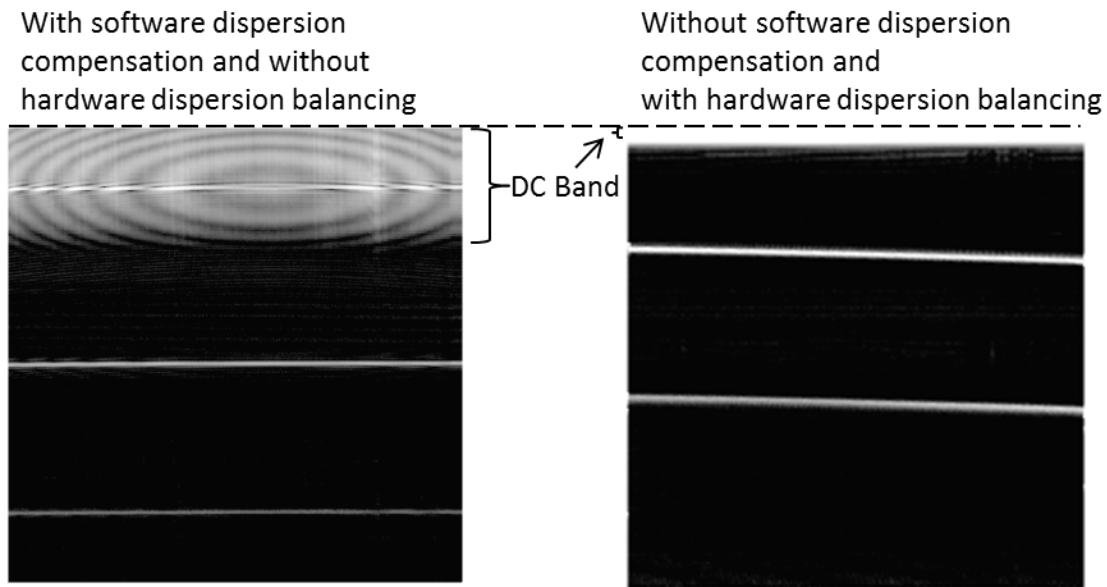


Figure 3.7: DC band reduction with the HDBU

3.5 OCT CHARACTERIZATION

The maximum imaging depth for OCT is determined by recording multiple PSFs of a mirror sample at different depths by translating the reference mirror by 200 μm at a time. Figure 3.8 shows the PSFs of a mirror separated by 200 μm in air with the 4 \times objective lens and an effective focal length of 100 mm spectrometer configuration. Since the physical distance between two PSF peaks is known, the depth (μm) to pixel ratio can be determined as shown in Figure 3.9 to be $2.8489 \frac{\mu\text{m}}{\text{pixel}}$. By multiplying this ratio with the number of pixels in the image (512), the maximum imaging depth for this configuration is determined to be around 1460 μm in air. The maximum imaging depth for the 10 \times objective lens and an effective focal length of 37.5 mm spectrometer configuration is around 550 μm in air. As such, the 10 \times objective lens configurations is used to image thinner samples such as the murine and piscine corneas, with higher resolution, while the 4 \times objective lens configuration is used to image thicker samples such as the human, porcine and bovine corneas.

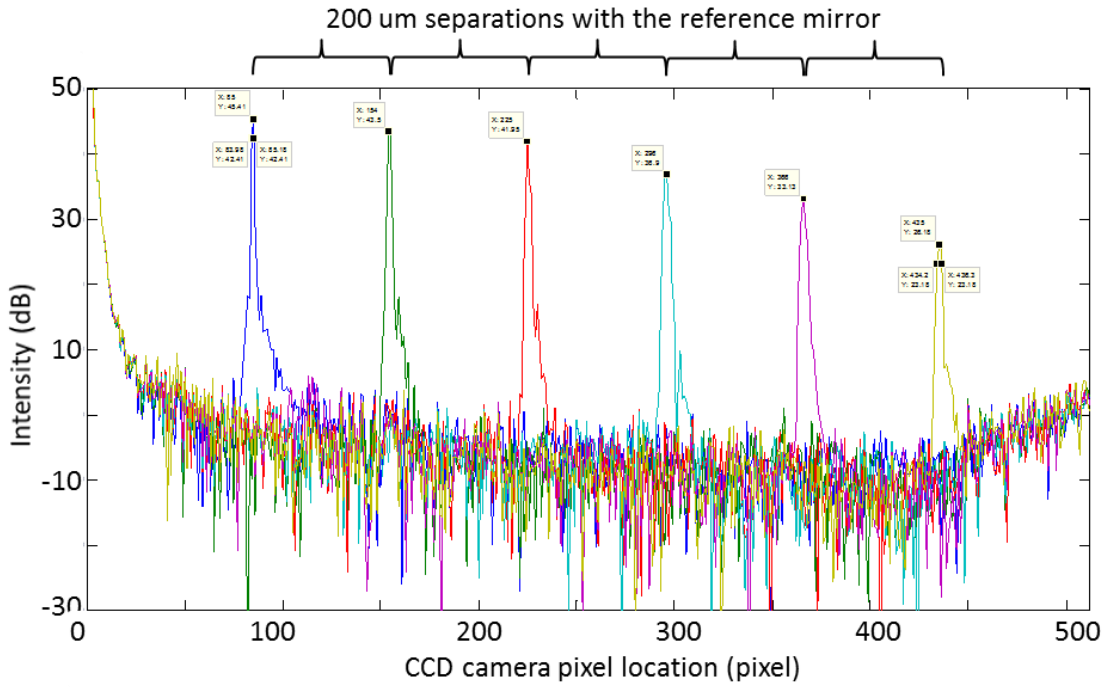


Figure 3.8: PSF peaks with 200 μm separations to determine the depth (μm) to pixel ratio for the 4× objective lens and an effective focal length = 100 mm spectrometer configuration

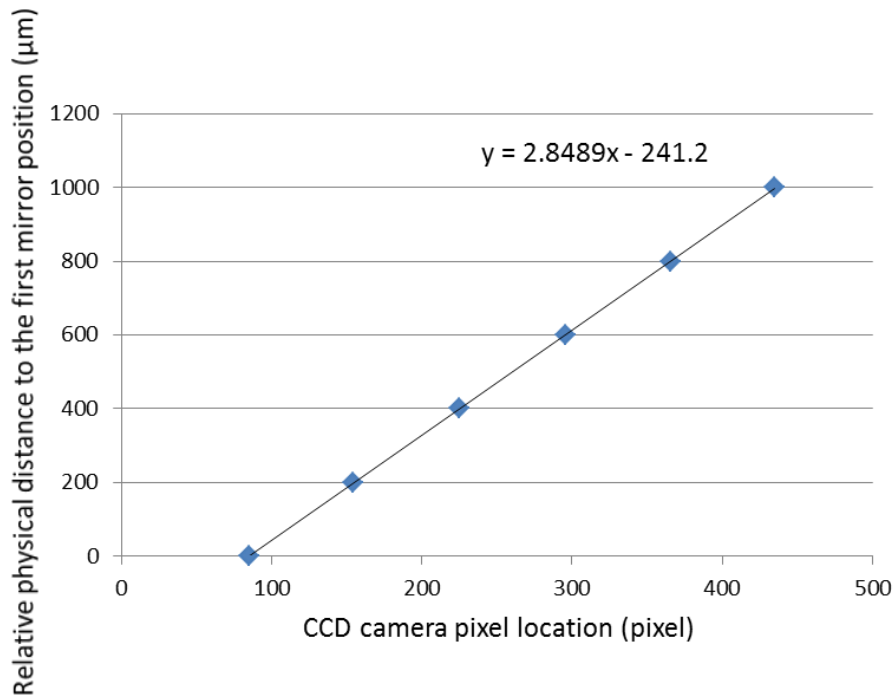


Figure 3.9: Determining the depth (μm) to pixel ratio from the mirror PSFs in Figure 3.8

The SNR, the axial resolution and the sensitivity fall-off of the 10× objective lens in conjunction with the spectrometer compound lens of effective focal length of 37.5 mm is summarized in table 3.4.

The SNR, the axial resolution and the sensitivity fall-off of the 4× objective lens in conjunction with the spectrometer compound lens of effective focal length of 100 mm is summarized in table 3.5. In this configuration, the maximum imaging depth is increased but the axial resolution and the signal to noise ratio are decreased. The sensitivity fall-off is ~12 dB over 1000 μm depth.

Peak #	Pixel #	Depth (μm)	SNR (dB)	Axial Resolution (μm)	Sensitivity Fall-off (dB)
1	85	242	45.41	3.42	0
2	154	439	43.50	4.78	1.91
3	225	641	41.95	3.38	3.46
4	296	843	36.90	5.30	8.51
5	366	1043	33.13	5.77	12.28
6	435	1239	26.18	5.98	19.23

Table 3.5: SNR, axial resolution and sensitivity fall-off of the 4× objective lens in conjunction with the spectrometer compound lens of effective focal length of 100 mm

The lateral resolutions are determined by measuring the edge response function of a silicon wafer [41]. The experimental setup is shown in Figure 3.10(a). An OCT cross-sectional image of a sharp wafer edge is taken. The OCT cross-sectional image and the intensity profile of the wafer edge are shown in Figure 3.10(b) and 3.10(c), respectively. By measuring the 10-90% width of the intensity profile of the sharp wafer edge in Figure 3.10(c), the lateral resolution can be determined. The lateral resolution using the 10× and 4× configurations are found to be 2.2 μm and 5.4 μm, respectively.

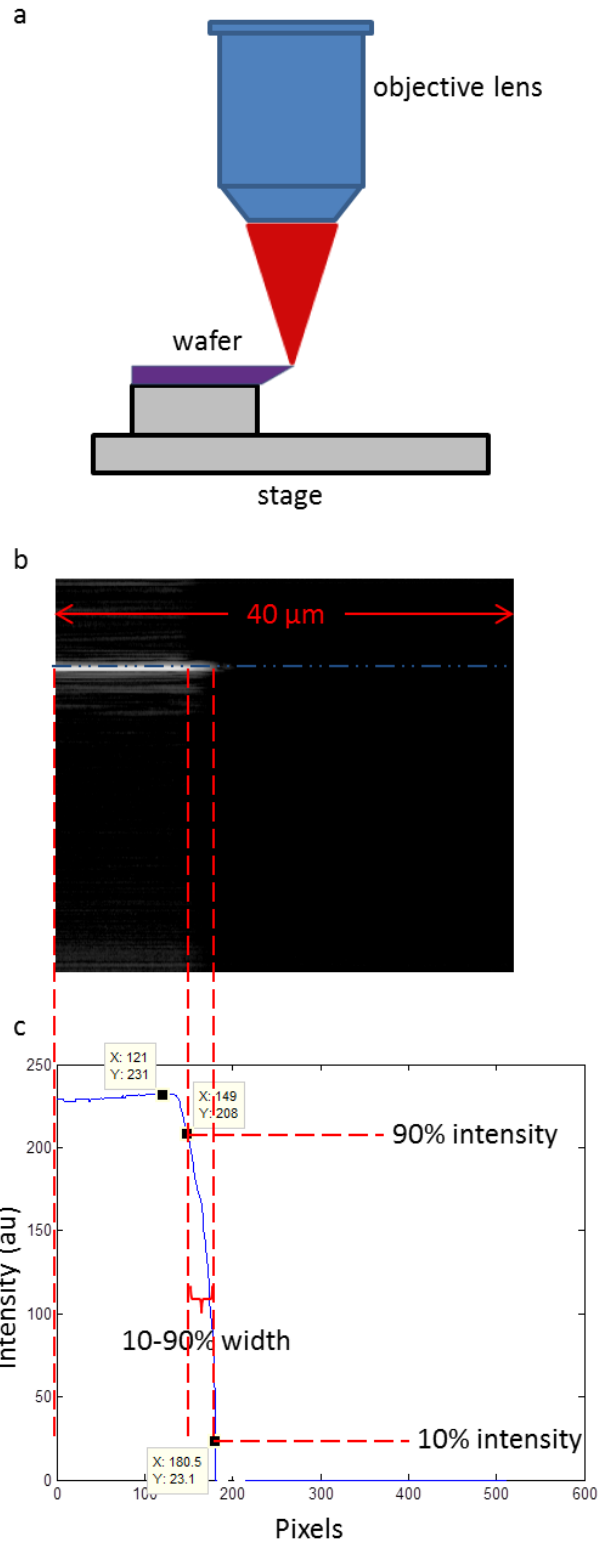


Figure 3.10: OCT lateral resolution for the 10× objective lens configuration. (a) OCT setup to measure lateral resolution. (b) OCT cross-sectional image of a wafer using the 10× objective configuration. (c) Intensity profile of the wafer’s edge.

3.6 MPM CHARACTERIZATION

The MPM axial and lateral resolutions are determined by imaging fluorescent microspheres imbedded in agarose gel. The size of the spheres is chosen to be much smaller than the theoretical, system-limited resolution, such that the PSF imaged in the axial and lateral directions correspond to their respective resolutions. The setup is shown in Figure 3.11. The axial and lateral resolutions for the 40 \times objective lens are determined to be around 1.6 μm and 0.6 μm . The axial and lateral resolutions for the 60 \times objective lens are determined to be around 1.5 μm and 0.4 μm .

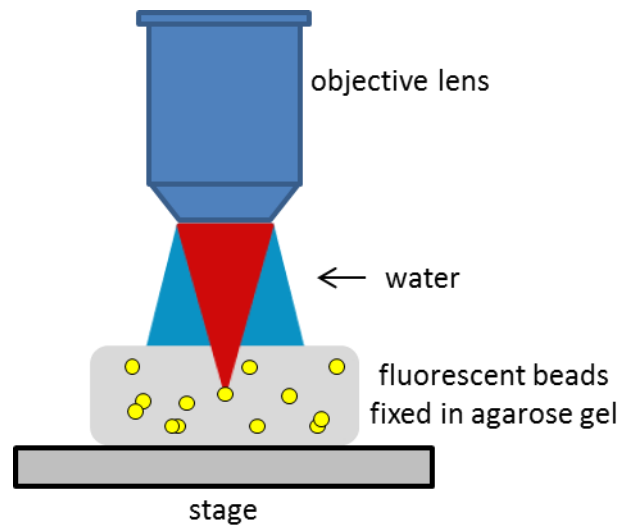


Figure 3.11: MPM setup to measure axial and lateral resolutions

CHAPTER 4: CORNEAL CHARACTERIZATION APPLICATION

4.1 INTRODUCTION AND MOTIVATION

MPM has the ability to visualize both cellular and collagen structures in corneas with high resolution and deep penetration through its biochemically specific contrasts. OCT has the ability to produce a cross-sectional image of the cornea with fast speeds through its scattering contrast. By combining the two modalities, their advantages are complemented and provide researchers a powerful tool to visualize corneal morphology. Furthermore, the combination of MPM and OCT can also be used to quantitatively characterize the thicknesses and RI of the major corneal layers. These properties are important in many ophthalmology applications. Since the visualization of the morphology and the quantitative characterization of the cornea can be done together, the combined MPM/OCT system allows doctors to acquire more information for better diagnosis and analysis.

In this chapter, the MPM/OCT system is used to image corneas of five different species: mouse, fish, human, pig and cow. When available, the five corneal layers are identified and the morphology is qualitatively compared across the five species. Finally the thicknesses and RI of the major layers are measured and quantitatively compared between the species. Section 4.2.1 provides information on the acquisition and preparation of the corneal tissues, Section 4.2.2 describes the image acquisition process, the method used to determine the thicknesses and RI of the cornea. Section 4.3 and Section 4.4 present the corneal morphology and quantitative characterization results, respectively. Finally Section 4.5 presents the discussion.

4.2 METHOD

4.2.1 ACQUISITION AND PREPARATION OF THE CORNEAL TISSUES

Murine and piscine eyeballs are acquired from C3H/HeN mice and tilapia fish, respectively. Porcine and bovine eyeballs are acquired from the animal facilities on campus and a local farm, respectively. The eyeballs are positioned inside a container with the anterior side facing the laser source, as shown in Figure 4.1. They are submerged under BSS sterile irrigation solution (Alcon Canada Inc.), and the corneas are imaged from the anterior side to the posterior side. The murine, piscine, and bovine eyeballs are imaged within 6 hours post-mortem. The porcine eyeballs are imaged within 12 hours post-mortem.

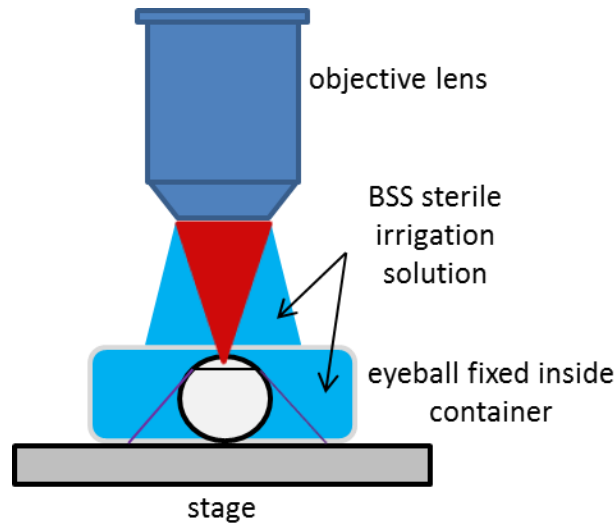


Figure 4.1: Murine, piscine, porcine, and bovine corneal imaging setup

Human corneas are obtained from the Vancouver General Hospital (VGH) eye bank. They are determined to be unsuitable for transplantation and thus are released for research purposes. The human corneas are excised corneal tissues. The samples are positioned inside a container with the laser source entering the posterior side first as

shown in Figure 4.2. These corneas are submerged under Optisol corneal storage media (Bausch & Lomb), and then imaged. They are stored in Optisol and are imaged within 6 weeks post-mortem. Unlike the other samples, the human corneas are several weeks old prior to imaging and exhibit some cloudiness, which limit the laser penetration through the thicker cellular layer of the epithelium. Therefore, in order to image the full thickness in MPM, the corneas are imaged with the laser entering the thinner cellular layer of the endothelium.

All the experimental protocols are approved by the ethics committee of the University of British Columbia.

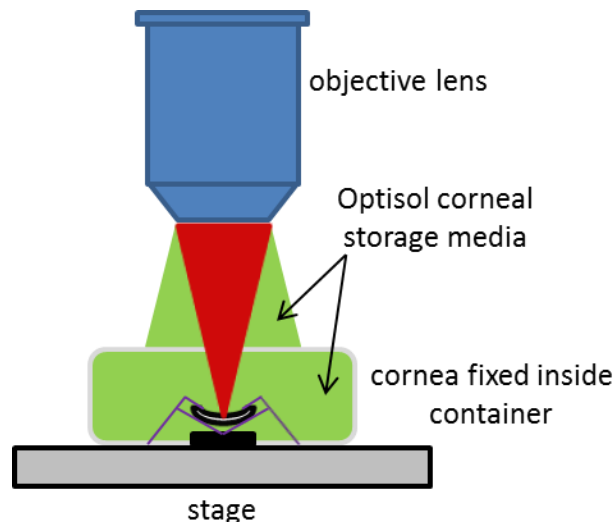


Figure 4.2: Human corneal imaging setup

4.2.2 MPM/OCT IMAGING AND RI AND THICKNESS MEASUREMENT

Firstly, a large field-of-view (FOV) OCT cross-sectional image of the sample is taken with the 10× or the 4× objective lens depending on the sample thickness. The FOV of the OCT can be controlled by changing the scanning voltage of the galvanometer scanner. The OCT axial imaging depth, determined by the effective focal length of the

lens in the spectrometer, is $\sim 550 \mu\text{m}$ for murine and piscine imaging and $\sim 1500 \mu\text{m}$ for human, porcine, and bovine imaging (Chapter 2).

Secondly the objective lens is switched to the $40\times$ objective lens without moving the sample. MPM *en face* images are obtained by scanning the X and Y galvanometer scanners. A stack of MPM *en face* images are acquired by stepping the piezo-scanner in the axial direction. By constructing a 3D volume using the *en face* images, a MPM cross-sectional image is generated as shown in Figure 4.3. The dimension of the MPM cross-sectional image in the axial direction is determined by the number of frames and the step size of the image stack. The maximum scanning range of the piezo-scanner is $400 \mu\text{m}$. If the sample thickness exceeds this value, multiple overlapping image stacks are taken by adjusting the sample stage with a micrometer. These overlapping MPM stacks are then merged together by identifying overlapping features in the *en face* images to form a single 3D volume.

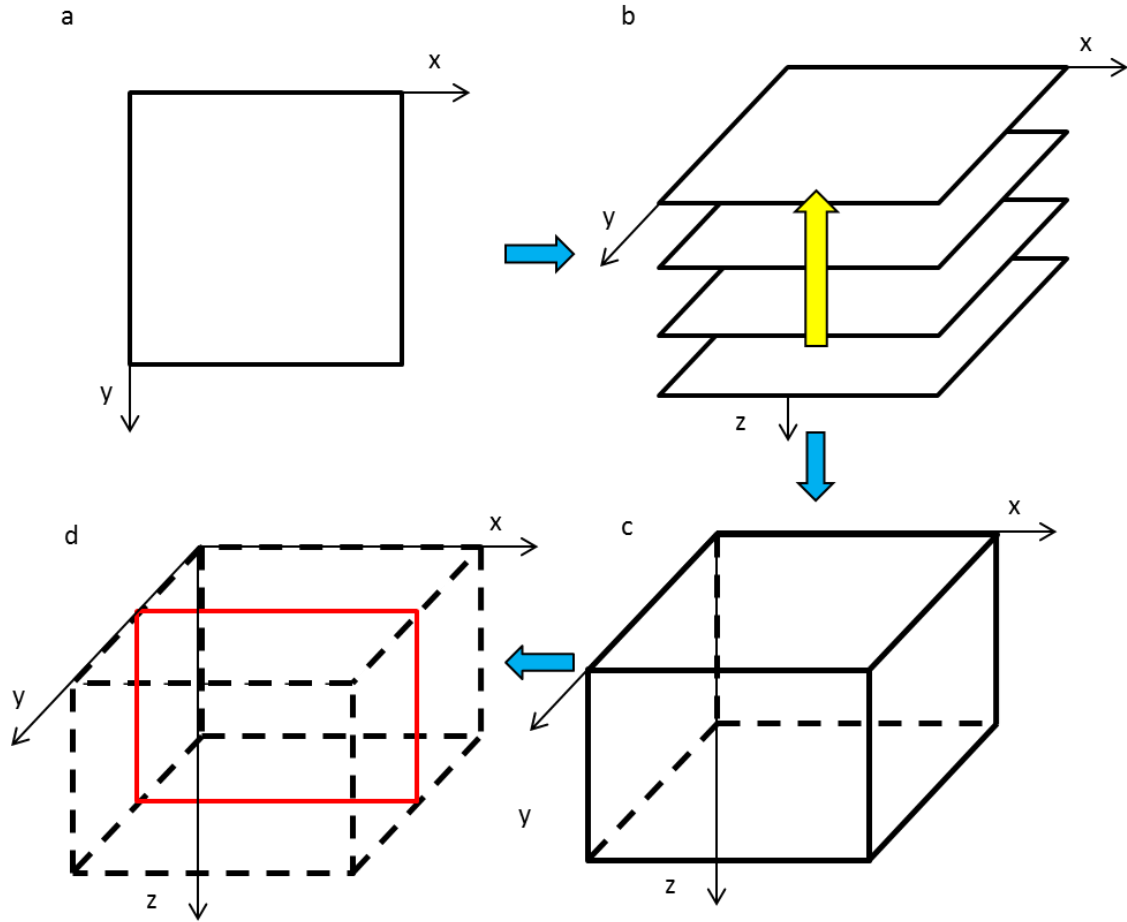


Figure 4.3: Generation of the MPM cross-sectional image from a stack of *en face* images. (a) One *en face* image is taken. (b) A stack of *en face* images are taken. (c) The stack of XY images are combined post-processing to obtain a MPM 3D volume. (d) A XZ cross-sectional MPM image is reconstructed from the 3D volume.

The thickness measured from the OCT image is the sample's optical pathlength, L_p . Assuming the group index is equivalent to the RI, for a sample of thickness t and RI of n , L_p can be expressed as:

$$L_p = t \times n \quad (4.1)$$

The thickness measured from the MPM cross-sectional image is named optical thickness, L_o , which corresponds to the distance the objective lens is moved when it steps through the sample. Based on multilayer refractions, L_o can be expressed as:

$$L_o = t \times \sqrt{\frac{n_o^2 - (NA)^2}{n^2 - (NA)^2}} \quad (4.2)$$

where NA is the numeric aperture of the objective lens (40×, $NA=0.8$), and n_o is the RI of the immersion medium. Here we assume the BSS sterile irrigation solution and the Optisol corneal storage media have a same RI as distilled water ($n_o=1.33$).

Using Equations 4.1 and 4.2, and applying ray tracing and trigonometry, equations for the RI and the physical thickness of the sample can be obtained as [40]:

$$n = \sqrt{\frac{(NA)^2 + \sqrt{(NA)^4 + 4[n_o^2 - (NA)^2]L_p^2 / L_o^2}}{2}} \quad (4.3)$$

$$t = \frac{\sqrt{2}L_p}{\sqrt{(NA)^2 + \sqrt{(NA)^4 + 4[n_o^2 - (NA)^2]L_p^2 / L_o^2}}} \quad (4.4)$$

By measuring the thicknesses L_p and L_o in the OCT and MPM images respectively, the RI and the physical thickness of the sample can be determined. The complete derivation of Equation 4.3 and Equation 4.4 can be found in Ref. [12].

Figure 4.4 shows an example of how L_p and L_o are obtained from the OCT and MPM images. Figure 4.4(a) shows an OCT cross-sectional image with an image width of 320 μm . Figure 4.4(b) shows the co-registered MPM cross-sectional image with an image width of 200 μm . The MPM and OCT images are co-registered because they share the same excitation beam path and the X and Y scanners. The respective OCT and MPM thicknesses (L_p and L_o respectively) for the epithelium and the stroma are determined by averaging 9 A-line profiles. From the L_p and L_o , the RI and thicknesses of the epithelial, stromal and the overall layers can be calculated using Equations 4.3 and 4.4.

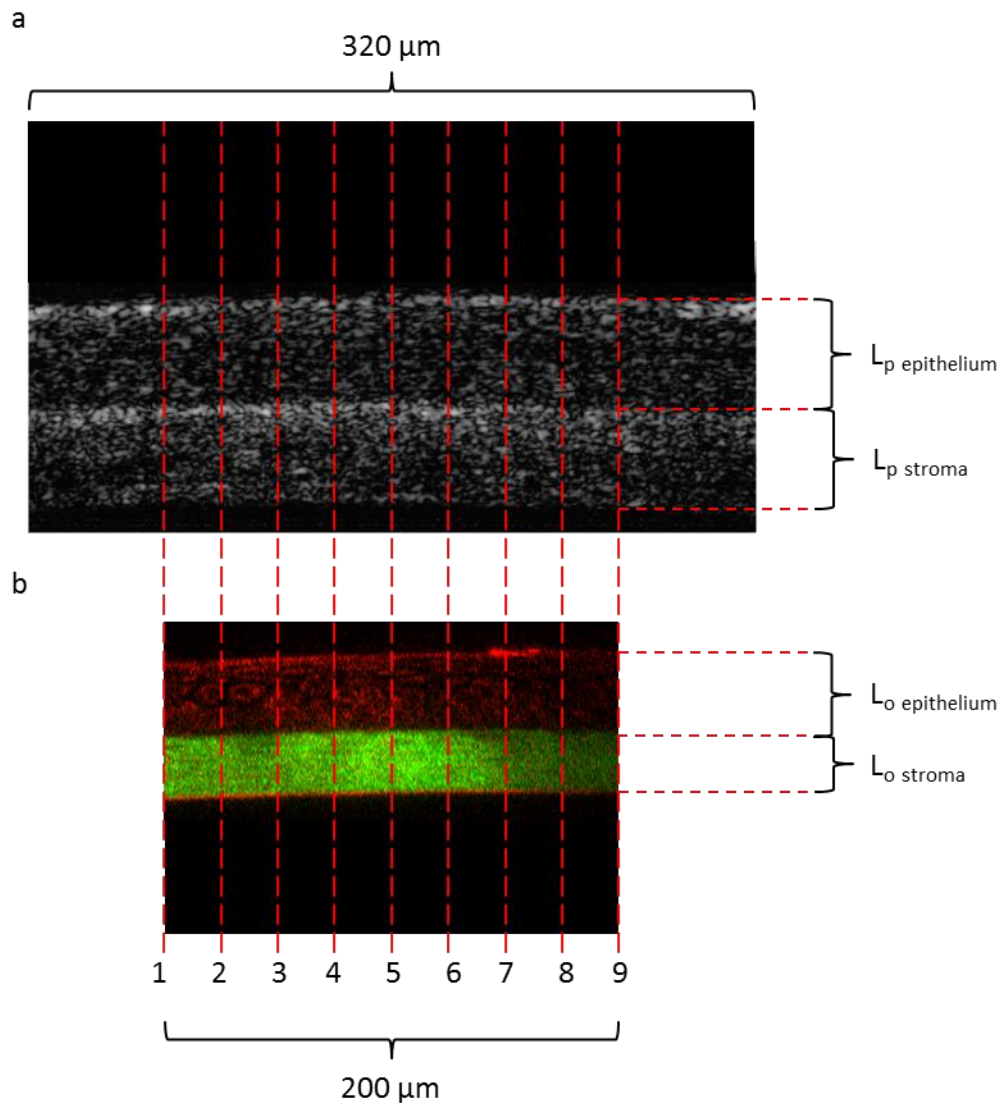


Figure 4.4: Determining the epithelial and stromal RI and thicknesses. (a) OCT cross-sectional image. (b) MPM cross-sectional image.

4.3 MORPHOLOGY

This section provides qualitative description and comparisons of the corneal morphology of the five different species.

4.3.1 MURINE CORNEA

Figure 4.5 shows the OCT and MPM images of a murine cornea. The OCT and MPM cross-sectional images are shown in Figures 4.5(a) and 4.5(b), respectively. In the

OCT cross-sectional image, two corneal layers are clearly distinguished. The top layer, L1, corresponds to the epithelium while the bottom layer, L2, is composed of mainly the stroma. The boundary between the epithelial and the stromal layers is observed due to the change in the RI at the interface. Collagen laminae can be seen in the stromal region in the OCT image. However, the thin Bowman's layer, Descemet's membrane, and endothelium cannot be differentiated from the stroma due to the lack of axial resolution and specificity in OCT. In the MPM cross-sectional image, three layers are clearly observed through the TPEF and SHG contrasts, color coded in red and green, respectively. Color yellow represents areas with overlapping TPEF and SHG signals which are caused by cross-talk between the two channels. From the top, the first layer (red) is the epithelium. The strong TPEF signal comes from the NADH inside the epithelial cells. The second layer (green) corresponds to the thick stroma which has strong SHG signals due to the type-I collagen fibers. The thin Bowman's layer is not differentiable from the stroma. The third layer (red) is composed of the Descemet's membrane and the monolayer of endothelial cells. They provide TPEF contrast from elastin in the Descemet's membrane and NADH in the endothelial cells. The co-registered MPM imaging area is marked by the red dashed rectangle on the larger-scaled OCT image in Figure 4.5(a).

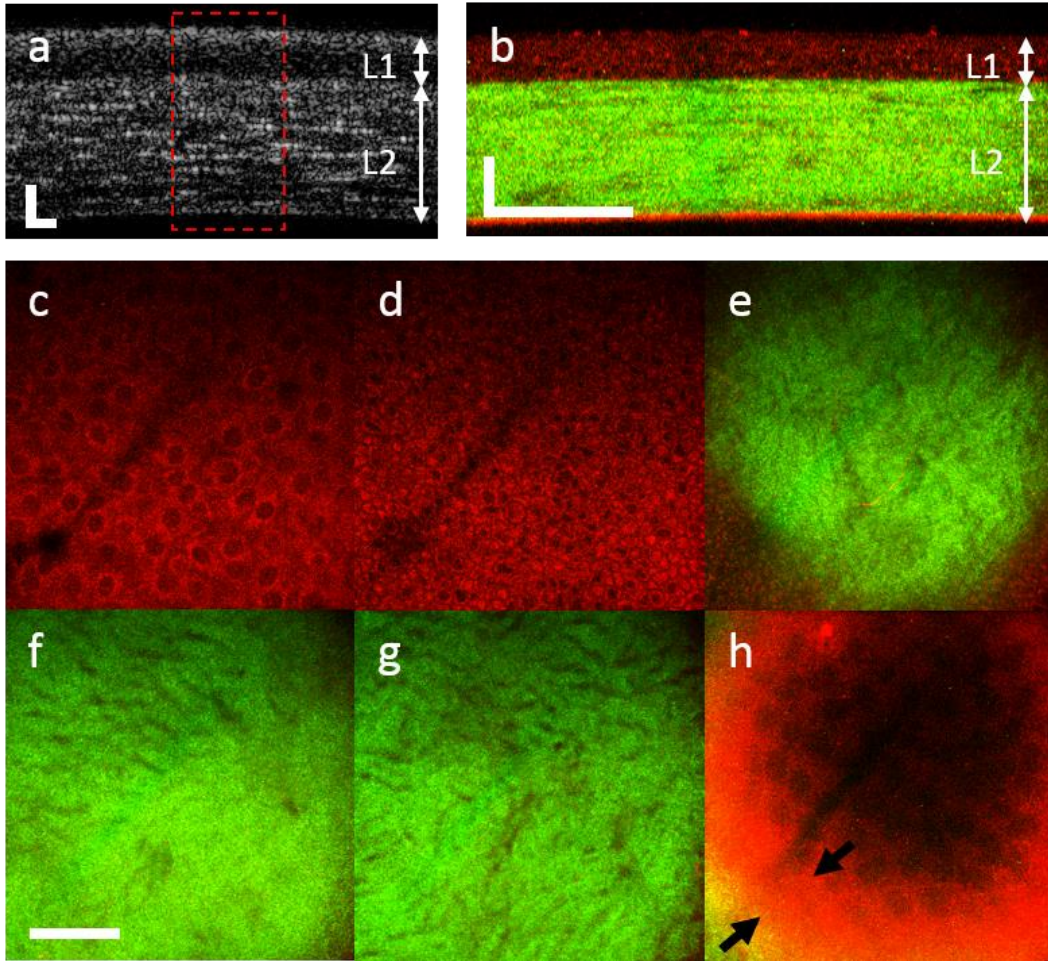


Figure 4.5: OCT and MPM images of a murine cornea. (a) OCT cross-sectional image. (b) MPM cross-sectional image. L1 is the epithelium layer. L2 is the Bowman's layer, stroma, Descemet's membrane, and endothelium layers. (c) – (h) MPM *en face* images. (c) Anterior epithelium. (d) Posterior epithelium. (e) Junction between the epithelium and the stroma. (f) Anterior stroma. (g) Posterior stroma. (h) Descemet's membrane and Endothelium. Arrowheads point to the Descemet's membrane. (c) – (h) are 12 μm , 28 μm , 42 μm , 92 μm , 146 μm , and 160 μm below the surface of the cornea, respectively. TPEF signals are in red. SHG signals are in green. Scale bars are 50 μm . The red dashed rectangle in the OCT image marks the co-registered MPM imaging area.

The MPM *en face* images from the anterior side to the posterior side of the murine cornea are shown in Figures 4.5(c) – (h). Larger cells are observed near the anterior side of the epithelium in Figure 4.5(c) while smaller cells are observed at the posterior side of the epithelium in Figure 4.5(d). The dark, diagonal band observable in Figures 4.5(c), 4.5(d) and 4.5(h) is an artifact that may have been caused by a blockage

of the beam somewhere in the beam path. Figure 4.5(e) shows the junction between the epithelium and the stroma. Interwoven collagen structures are observed in the stromal layer in Figures 4.5(f) and 4.5(g). A single layer of endothelium cells arranged in a honeycomb mosaic is detected at the posterior end of the cornea as shown in Figure 4.5(h). The Descemet's membrane is the region between the posterior stroma and the endothelial layer. This membrane is composed of mostly type-IV collagen which cannot be observed by SHG. However, it also contains elastin which provides TPEF contrast [9]. It is identified as the region between the arrowheads in Figure 4.5(h) where there is TPEF contrast but no honeycomb structure of cells.

4.3.2 PISCINE CORNEA

OCT and MPM images of a piscine cornea is shown in Figure 4.6 The OCT and MPM cross-sectional images are shown in Figures 4.6(a) and 4.6(b), while the MPM *en face* images are shown in Figures 4.6(c) – (h). Similar to the murine cornea, the epithelium, L1, and the stroma, L2, are identified in both the OCT and the MPM cross-sectional images. However, in the MPM cross-sectional image, the stroma can be further differentiated into two distinct sub-layers with different SHG intensities, labeled as S1 and S2. In the *en face* images, larger cells are detected near the anterior side of the epithelium in Figure 4.6(c) while smaller cells are observed at the posterior side of the epithelium in Figure 4.6(d). The interface between the epithelium and the stroma is shown in Figure 4.6(e). Figures 4.6(f) and 4.6(g) show representative collagen structures in the two stromal layers, S1 and S2, respectively. In the S1 layer, collagen fibers appear to form an orientation as marked by the black double arrow. This orientation changes direction from lamellae to lamellae. Meanwhile, the collagen fibers within the S2 layer

appear to be finer. Due to the difference in the fiber sizes, S1 shows a much higher SHG signal intensity than S2. Lastly, a thin layer of TPEF signal composed of the Descemet's membrane and the endothelium is seen at the posterior end of the cornea, as shown in Figure 4.6(h).

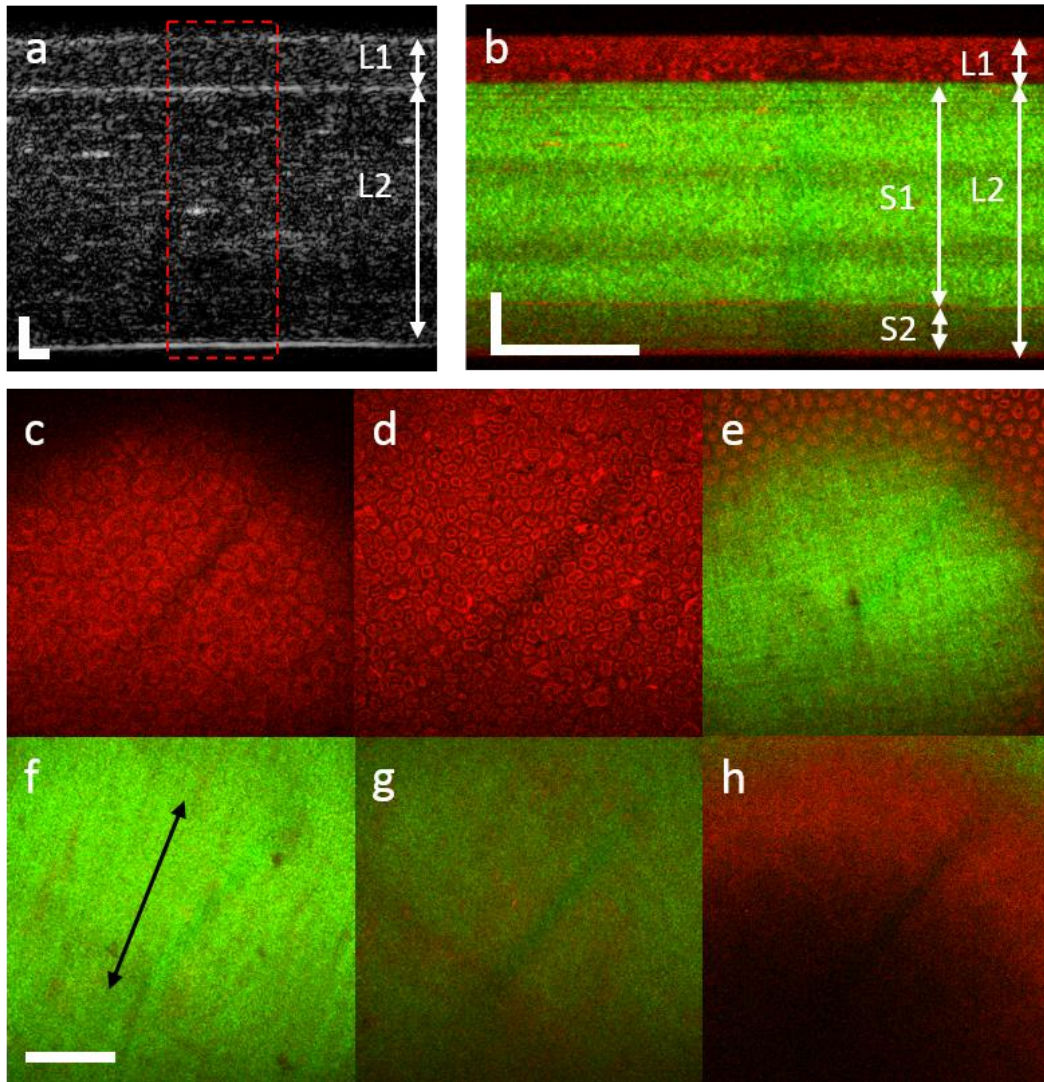


Figure 4.6: OCT and MPM images of a piscine cornea. (a) OCT cross-sectional image. (b) MPM cross-sectional image. S1 and S2 are the first and second stromal layers. (c) – (h) MPM *en face* images. (c) Anterior epithelium. (d) Posterior epithelium. (e) Junction between the epithelium and the stroma. (f) Stroma in S1. (g) Stroma in S2. (h) Descemet's membrane and endothelium. (c) – (h) are 4 μm , 28 μm , 44 μm , 69 μm , 253 μm , and 282 μm below the surface of the cornea, respectively. Double arrow marks the direction of the collagen fiber bundles. Scale bars are 50 μm . The red dashed rectangle in the OCT image marks the co-registered MPM imaging area.

4.3.3 HUMAN CORNEA

Figure 4.7 shows the OCT and MPM images of a human cornea. The OCT and MPM cross-sectional images are shown in Figures 4.7(a) and 4.7(b), and the MPM *en face* images are shown in Figures 4.7(c) – (h). Although the human corneas are imaged with the laser entering the cornea from the posterior side, the images in Figure 4.7 have been rearranged such that the orientation matches the format for the other species. Both the epithelial and stromal layers are observed in the OCT and MPM cross-sectional images. Because the human cornea attenuates the laser power significantly, the TPEF contrast is increased post-process to visualize the epithelium in Figure 4.7(b). As such, the increased TPEF signal overlaps with the strong SHG signal at the posterior stroma to cause the bright yellow color in the image. The cellular structure of the epithelium is shown in Figure 4.7(c) while the transition between the epithelium and the stroma is displayed in Figure 4.7(d). The SHG signal in Figure 4.7(d) is more indistinct and diffused which corresponds to the Bowman’s layer. Figure 4.7(e) shows the anterior stroma just below the Bowman’s layer, where it has regions of weak SHG signal as marked by the yellow arrowheads. Such patterns have also been observed by Morishige et al. [42,43]. Similar to the piscine corneas, small collagen fibers are observed that together seem to indicate a general orientation of the overall collagen structure, which varies from lamellae to lamellae. Furthermore, straight and dark ridges that are not present in the other species are seen in Figures 4.7(f) and 4.7(g), marked with red arrowheads. These dark ridges are suspected to be collagen micro-folds that are caused by corneal swelling [21]. The Descemet’s membrane and the endothelium are displayed

in Figure 4.7(h). The Descemet's membrane is shown as the TPEF region (red) between the posterior stroma and the endothelium, marked between the black arrows.

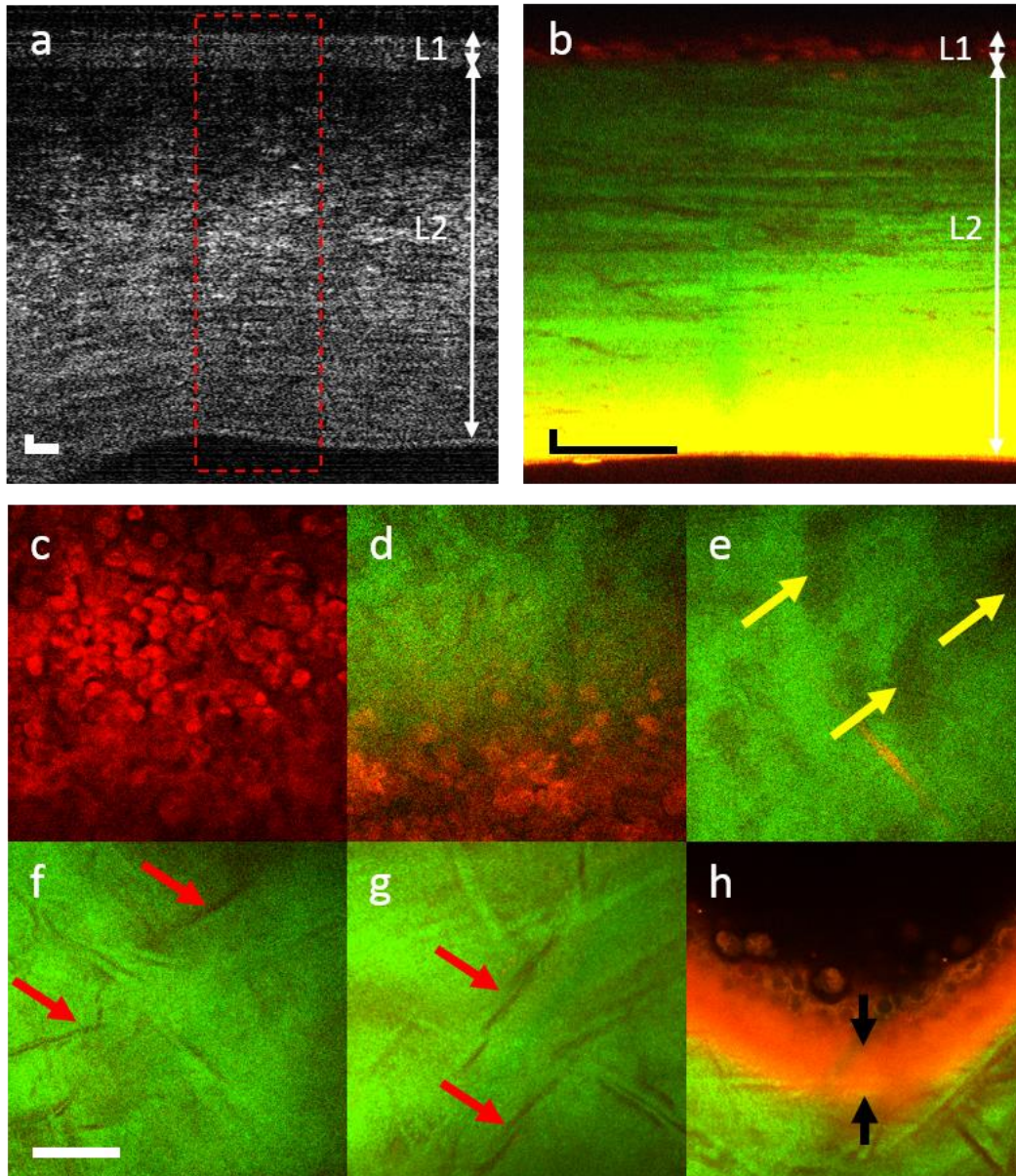


Figure 4.7: OCT and MPM images of a human cornea . (a) OCT cross-sectional image. (b) MPM cross-sectional image. (c) – (h) MPM *en face* images. (c) Epithelium. (d) Bowman's layer. (e) – (g) Anterior to posterior stroma. (h) Descemet's membrane and endothelium. Yellow arrowheads point to regions of weaker SHG signal in the anterior stroma. Red arrowheads point to collagen micro-folds. Black arrowheads point to the Descemet's membrane. (c) – (h) are 42 μm , 68 μm , 110 μm , 340 μm , 680 μm , and 870 μm below the surface of the cornea, respectively. Scale bars are 50 μm . The red dashed rectangle in the OCT image marks the co-registered MPM imaging area.

The Bowman's layer is more clearly observed and differentiated from the rest of the stroma in another human dataset as shown in Figure 4.8. The epithelium and the junction between epithelium and the stroma are shown in Figures 4.8(a) and 4.8(b). The anterior stroma displayed in Figures 4.8(d) and 4.8(e), is identifiable by its distinct regions of weak SHG signal with fine and randomly arranged collagen bundles. Between the anterior stroma and the epithelium is the Bowman's layer as shown in Figure 4.8(c), where the collagen signal is more indistinct and diffused. For qualitative comparison, a typical stromal region is shown in Figure 4.8(f).

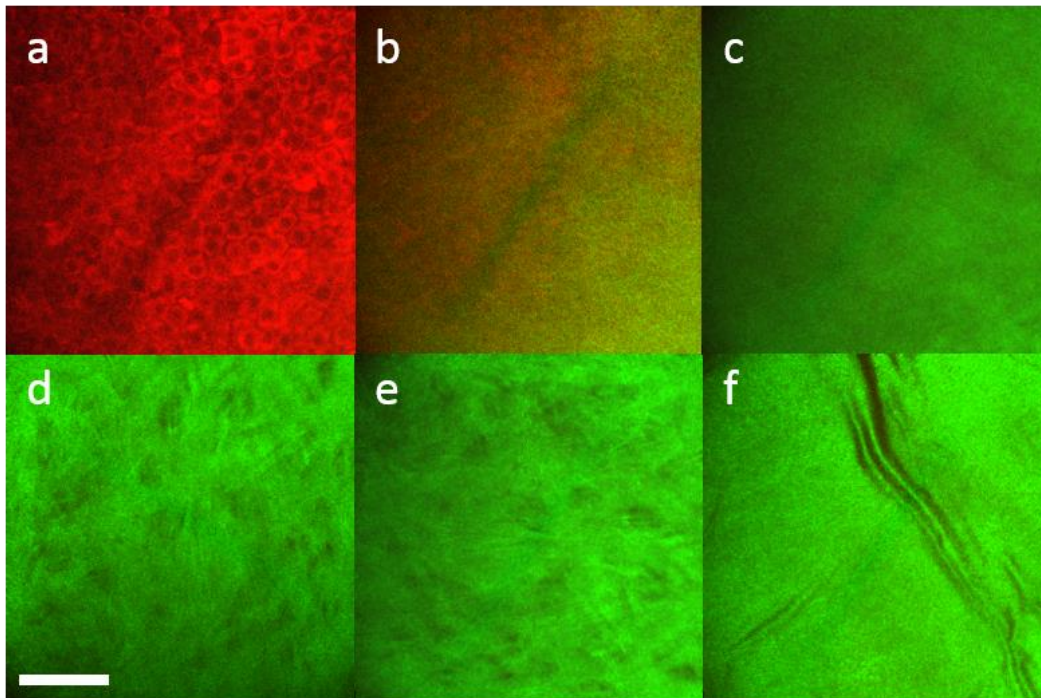


Figure 4.8: MPM *en face* images identifying the human Bowman's Layer. (a) Epithelium. (b) Posterior epithelium. (c) Bowman's layer. (d) – (e) Anterior stroma. (f) A typical stromal region. (a) – (f) are 26 μm , 34 μm , 42 μm , 50 μm , 60 μm , and 220 μm below the surface of the cornea, respectively. Scale bar is 50 μm .

4.3.4 PORCINE CORNEA

Figure 4.9 shows the OCT and MPM images of a porcine cornea. The OCT and MPM cross-sectional images are shown in Figs. 4.9(a) and 4.9(b), and the MPM *en face*

images are shown in Figures 4.9(c) – (h). At the junction between the epithelium and the stroma, finer collagen fiber bundles in a randomly organized pattern are observed in Figures 4.9(d) and 4.9(e), which are specific features of the Bowman’s layer. The Bowman’s layer is estimated as the region between the arrowheads. The exact boundary for the Bowman’s layer is hard to identify due to the smooth transition between the collagen fibers in the Bowman’s layer and the collagen fibers in the stroma. The continuous transition from the finer fiber bundles to the larger fiber bundles of the anterior stroma is shown in Figure 4.9(e). In the stroma, similar to the murine corneas, interwoven collagen structures are observed (Figures 4.9(e) – (g)). However, different from the murine corneas, large gaps which lack the SHG contrast are observed in both the *en face* and the cross-sectional MPM images. In addition, we notice that the interwoven patterns become finer and denser as we approach the posterior stroma.

The Bowman’s layer and its continuous transition into the anterior stroma are better observed in another porcine dataset as shown in Figure 4.10. The junction between the epithelium and the stroma is shown in Figure 4.10(a). The smooth transition of the collagen fiber bundles from finer and more randomly organized to larger and organized is shown in Figures 4.10(a) and 4.10(b). A typical collagen structure seen in the middle of the stroma is shown in Figure 4.10(c) for comparison.

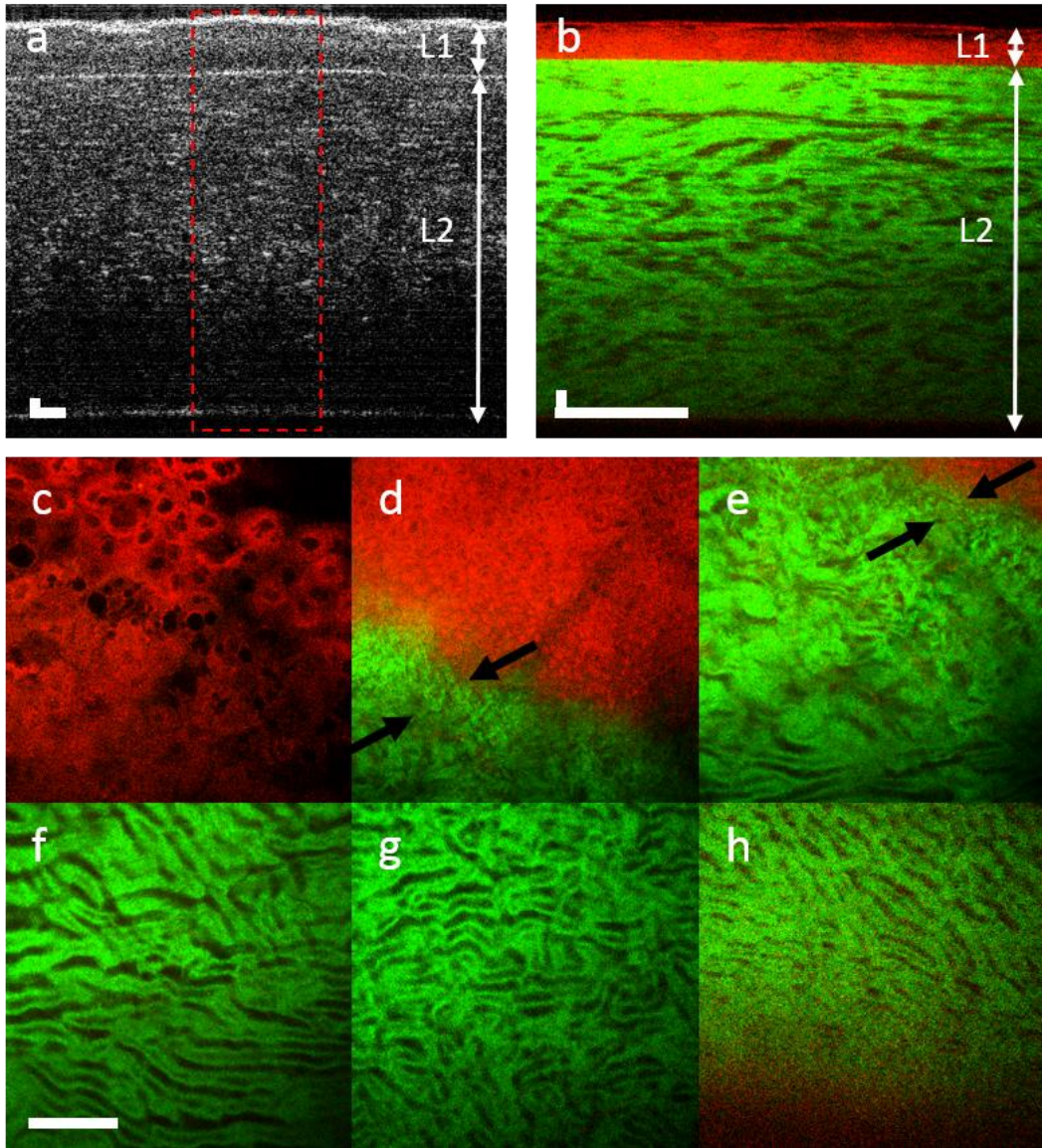


Figure 4.9: OCT and MPM images of a porcine cornea. (a) OCT cross-sectional image. (b) MPM cross-sectional image. (c) – (h) MPM *en face* images. (c) Anterior epithelium. (d) – (e) Junction between the posterior epithelium and the stroma. The Bowman's membrane is estimated as the region between the two arrowheads. (f) – (g) Anterior to posterior stroma. (h) Descemet's membrane and endothelium. (c) – (h) are 12 μm , 72 μm , 96 μm , 234 μm , 534 μm , and 772 μm below the surface of the cornea, respectively. Scale bars are 50 μm . The red dashed rectangle in the OCT image marks the co-registered MPM imaging area.

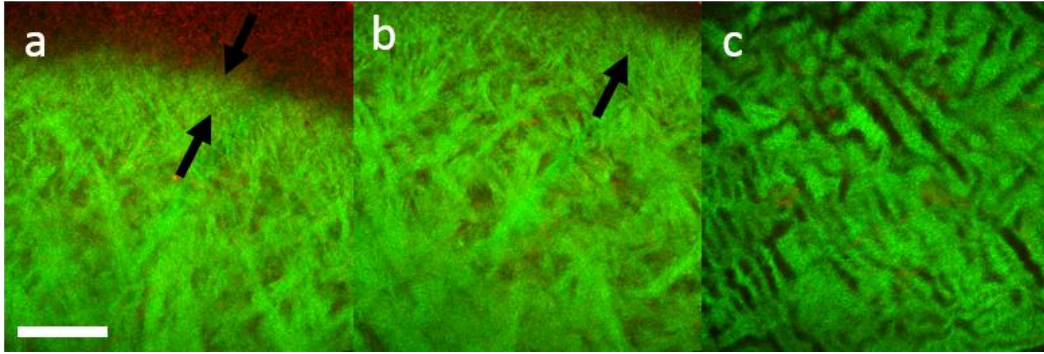


Figure 4.10: MPM *en face* images identifying the porcine Bowman's Layer. Collagen structural comparison between the Bowman's layer (a) – (b) and a typical stromal region (c) of a porcine cornea. (a) – (c) are 60 μm , 68 μm , and 190 μm below the surface of the cornea, respectively. Scale bar is 50 μm . The Bowman's membrane is highlighted by the arrowheads.

4.3.5 BOVINE CORNEA

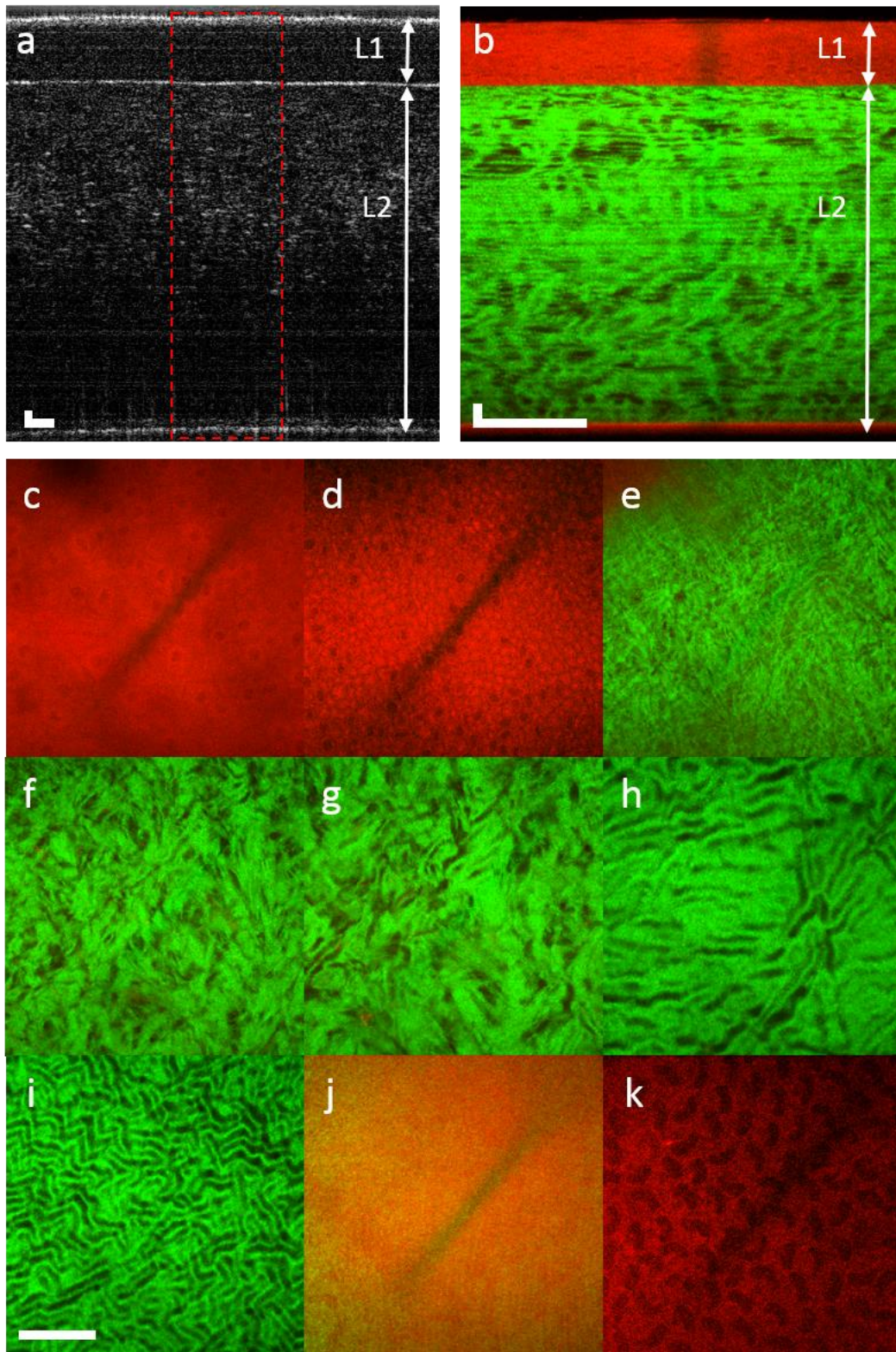


Figure 4.11: OCT and MPM images of a bovine cornea. (a) OCT cross-sectional image. (b) MPM cross-sectional image. (c) – (k) MPM *en face* images. (c) Anterior epithelium. (d) Posterior epithelium. (e) Bowman’s layer. (f) – (g) Transition from the Bowman’s layer to the stroma. (h) Anterior stroma. (i) Posterior stroma. (j) Descemet’s membrane. (k) Endothelium. (c) – (k) are 36 μm , 136 μm , 154 μm , 164 μm , 174 μm , 478 μm , 898 μm , 934 μm , and 958 μm below the surface of the cornea, respectively. Scale bars are 50 μm . The red dashed rectangle in the OCT image marks the co-registered MPM imaging area.

Figure 4.11 shows the OCT and MPM images of a bovine cornea. The OCT and MPM cross-sectional images are shown in Figures 4.11(a) and 4.11(b), and the MPM *en face* images are shown in Figures 4.11(c) – (k). In Figure 4.11(b), dark and bright horizontal lines are observed likely due to the different lamellae in the stroma. In stroma, collagen fibers form lamellae, where the fibers in a particular lamella run parallel with each other, but changes orientation from lamella to lamella. SHG intensity depends on the relative angle between the collagen fiber orientation and the laser polarization [44]. For different fiber orientations, the SHG intensity can vary from maximum to minimum and thus causes the horizontal lines. These lamellae are more clearly observed in the bovine samples likely because they are thicker than in other species. Similar to the porcine corneas, the collagen fibers at the Bowman’s layer are finer and in a randomly organized pattern, as shown in Figure 4.11(e). The transition from the finer collagen bundles of the Bowman’s layer to the larger collagen bundles of the anterior stroma is displayed in Figures 4.11(f) and 4.11(g). In the stroma, similar to the murine and porcine corneas, interwoven collagen structures are identified, as shown in Figures 4.11(h) and 4.11(i). Similar to the porcine cornea, the interwoven patterns become finer and denser towards the posterior stroma. The Descemet’s membrane is shown as a cloud of TPEF signals with no distinct structure in Figure 4.11(j) while the endothelial cells are shown in Figure 4.11(k).

4.4 QUANTITATIVE CHARACTERIZATION

The quantitative characterization of the RI and the thickness of the cornea are carried out on the two distinct layers of the cornea, L1 and L2. The L1 layer corresponds to the epithelium. The L2 layer is mainly composed of stroma but also includes the Descemet's membrane and the endothelium, and the Bowman's layer when it exists. The full thickness of the cornea and the overall RI over the entire cornea thickness are also obtained. The RI and thickness results for each species are summarized in Tables 4.1 – 4.5, for 6 murine corneas, 6 piscine corneas, 8 human corneas, 3 porcine corneas, and 5 bovine corneas, respectively. These results are also visually displayed in Figure 4.12.

Sample #	Parameters	Layer		
		L1	L2	Overall
1	Refractive Index	1.413 ± 0.030	1.330 ± 0.009	1.354 ± 0.006
	Thickness (µm)	47 ± 1.4	112 ± 1.0	159 ± 1.5
2	Refractive Index	1.356 ± 0.012	1.365 ± 0.004	1.363 ± 0.004
	Thickness (µm)	46 ± 0.4	119 ± 0.6	165 ± 0.4
3	Refractive Index	1.337 ± 0.018	1.363 ± 0.005	1.357 ± 0.004
	Thickness (µm)	42 ± 1.0	126 ± 1.0	168 ± 1.0
4	Refractive Index	1.403 ± 0.010	1.361 ± 0.002	1.371 ± 0.002
	Thickness (µm)	43 ± 1.1	126 ± 1.1	169 ± 0.8
5	Refractive Index	1.365 ± 0.006	1.400 ± 0.009	1.382 ± 0.004
	Thickness (µm)	80 ± 0.6	71 ± 0.6	151 ± 0.9
6	Refractive Index	1.349 ± 0.022	1.342 ± 0.019	1.346 ± 0.007
	Thickness (µm)	83 ± 1.4	65 ± 1.3	148 ± 1.1
Average	Refractive Index	1.371 ± 0.016	1.360 ± 0.008	1.362 ± 0.005
	Thickness (µm)	57 ± 18	103 ± 26	160 ± 8

Table 4.1: RI and thickness results for 6 murine corneas

Sample #	Parameters	Layer		
		L1	L2	Overall
1	Refractive Index	1.468 ± 0.026	1.333 ± 0.001	1.353 ± 0.003
	Thickness (µm)	43 ± 1.5	244 ± 1.2	287 ± 0.8
2	Refractive Index	1.499 ± 0.020	1.357 ± 0.003	1.377 ± 0.005
	Thickness (µm)	43 ± 1.1	256 ± 1.1	299 ± 0.9
3	Refractive Index	1.567 ± 0.063	1.323 ± 0.001	1.360 ± 0.010
	Thickness (µm)	43 ± 1.0	237 ± 1.1	280 ± 2.0
4	Refractive Index	1.587 ± 0.024	1.325 ± 0.003	1.366 ± 0.002
	Thickness (µm)	43 ± 0.9	231 ± 1.1	274 ± 0.7
5	Refractive Index	1.449 ± 0.018	1.337 ± 0.002	1.353 ± 0.003
	Thickness (µm)	42 ± 0.4	250 ± 0.8	292 ± 0.8
6	Refractive Index	1.438 ± 0.009	1.336 ± 0.002	1.352 ± 0.002
	Thickness (µm)	45 ± 0.7	239 ± 0.6	284 ± 0.4
Average	Refractive Index	1.502 ± 0.057	1.335 ± 0.011	1.360 ± 0.009
	Thickness (µm)	43 ± 1	243 ± 8	286 ± 8

Table 4.2: RI and thickness results for 6 piscine corneas

Sample #	Parameters	Layer		
		L1	L2	Overall
1	Refractive Index	1.482 ± 0.009	1.338 ± 0.002	1.349 ± 0.002
	Thickness (µm)	66 ± 0.6	822 ± 3.4	888 ± 3.3
2	Refractive Index	1.439 ± 0.025	1.356 ± 0.003	1.364 ± 0.003
	Thickness (µm)	90 ± 2.6	822 ± 17.5	912 ± 18.0
3	Refractive Index	1.399 ± 0.017	1.349 ± 0.002	1.353 ± 0.003
	Thickness (µm)	58 ± 2.2	759 ± 10.9	817 ± 11.0
4	Refractive Index	1.414 ± 0.024	1.358 ± 0.008	1.362 ± 0.009
	Thickness (µm)	58 ± 2.1	796 ± 1.7	854 ± 1.8
5	Refractive Index	1.435 ± 0.012	1.347 ± 0.015	1.355 ± 0.015
	Thickness (µm)	67 ± 0.8	727 ± 3.8	794 ± 4.4
6	Refractive Index	1.438 ± 0.015	1.358 ± 0.010	1.365 ± 0.010
	Thickness (µm)	65 ± 1.0	711 ± 3.1	776 ± 3.8
7	Refractive Index	1.418 ± 0.018	1.373 ± 0.008	1.376 ± 0.007
	Thickness (µm)	59 ± 1.1	711 ± 1.7	770 ± 2.0
8	Refractive Index	1.442 ± 0.009	1.380 ± 0.008	1.385 ± 0.007
	Thickness (µm)	65 ± 1.1	734 ± 6.4	798 ± 7.1
Average	Refractive Index	1.433 ± 0.023	1.357 ± 0.013	1.363 ± 0.011
	Thickness (µm)	66 ± 10	760 ± 44	826 ± 49

Table 4.3: RI and thickness results for 8 human corneas

Sample #	Parameters	Layer		
		L1	L2	Overall
1	Refractive Index	1.604 ± 0.022	1.356 ± 0.003	1.386 ± 0.002
	Thickness (µm)	101 ± 3.5	732 ± 2.6	833 ± 1.4
2	Refractive Index	1.405 ± 0.017	1.325 ± 0.000	1.331 ± 0.002
	Thickness (µm)	65 ± 1.7	801 ± 0.3	866 ± 1.7
3	Refractive Index	1.418 ± 0.012	1.348 ± 0.001	1.352 ± 0.001
	Thickness (µm)	59 ± 1.9	894 ± 2.3	953 ± 2.8
Average	Refractive Index	1.476 ± 0.091	1.343 ± 0.013	1.357 ± 0.023
	Thickness (µm)	75 ± 19	809 ± 66	884 ± 51

Table 4.4 RI and thickness results for 3 porcine corneas

Sample #	Parameters	Layer		
		L1	L2	Overall
1	Refractive Index	1.395 ± 0.004	1.379 ± 0.001	1.381 ± 0.001
	Thickness (µm)	160 ± 1.2	815 ± 2.2	975 ± 1.4
2	Refractive Index	1.394 ± 0.006	1.379 ± 0.000	1.382 ± 0.001
	Thickness (µm)	164 ± 0.9	825 ± 0.8	989 ± 1.4
3	Refractive Index	1.408 ± 0.000	1.374 ± 0.001	1.380 ± 0.001
	Thickness (µm)	156 ± 1.1	837 ± 0.6	993 ± 1.7
4	Refractive Index	1.395 ± 0.006	1.372 ± 0.001	1.375 ± 0.001
	Thickness (µm)	161 ± 1.9	853 ± 1.3	1014 ± 0.9
5	Refractive Index	1.408 ± 0.004	1.378 ± 0.001	1.382 ± 0.000
	Thickness (µm)	142 ± 0.6	885 ± 0.6	1027 ± 0.0
Average	Refractive Index	1.400 ± 0.007	1.376 ± 0.003	1.380 ± 0.003
	Thickness (µm)	157 ± 8	843 ± 25	1000 ± 19

Table 4.5: RI and thickness results for 5 bovine corneas

The RI are calculated by averaging multiple A-lines in the co-registered MPM and OCT cross-sectional images, where the error bars represent the standard deviations. The RI from the epithelial layer, L1, is found to be higher than the RI from L2 in most of the samples except for a few murine corneas. The epithelial RI is higher likely due to the lipid and DNA compositions in the cell membrane and nuclei. The exception in some of the murine corneas is likely caused by the decrease in measurement accuracy due to the thin murine epitheliums. The RI of the piscine epithelium is significantly higher than its

stromal RI and the epithelial RI of the other species, possibly because the piscine eyes function in a water environment as compared to air for the other species. For the three porcine corneas, sample one is from a Yucatan swine while samples two and three are from the domestic Yorkshire swine. The epithelial RI from sample one of the porcine corneas is significantly higher than the epithelial RI from the other two samples which shows that different sub-species could have different RI values. For the other species, the RI values are relatively consistent among the different samples of the same species.

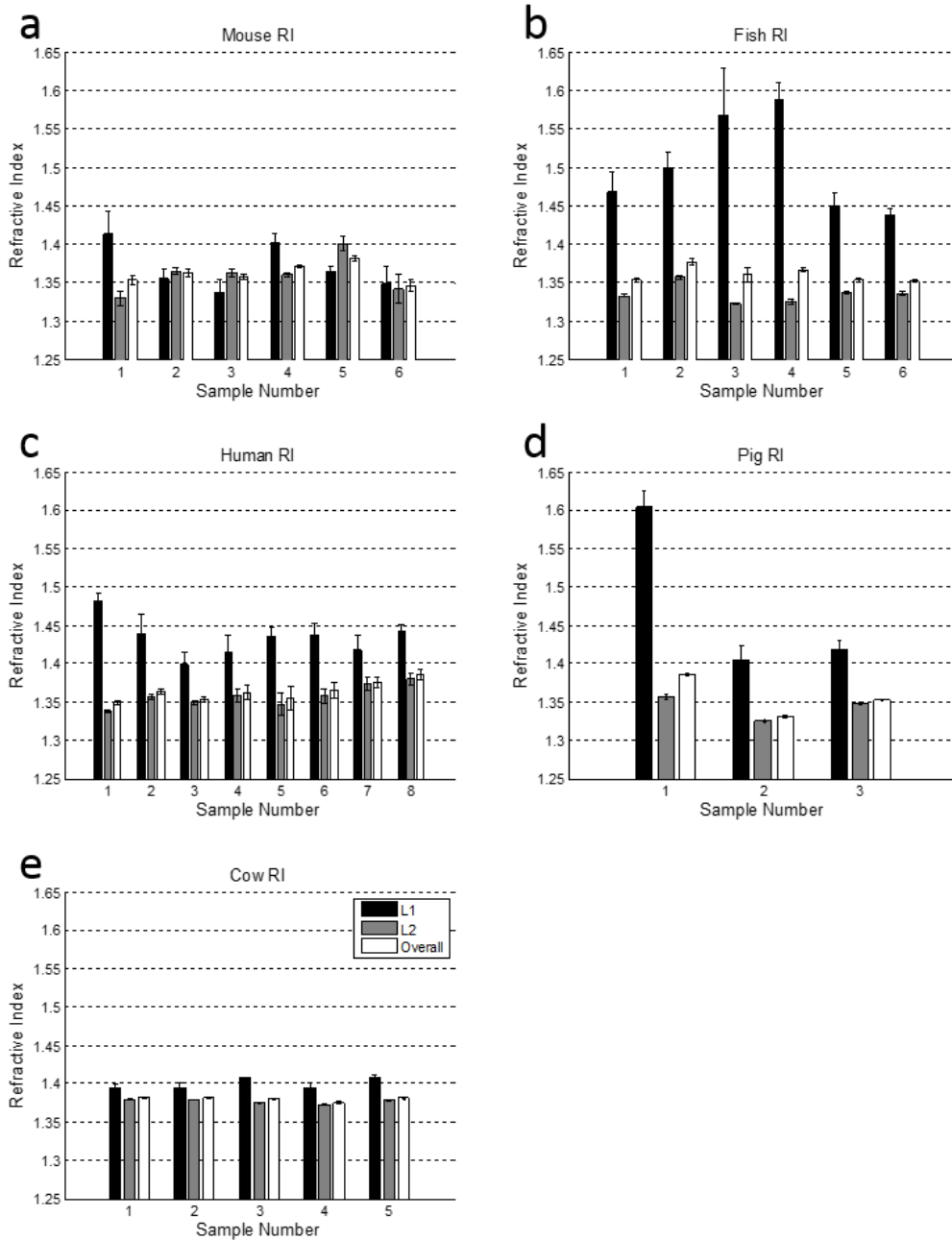


Figure 4.12: RI results. (a) 6 murine samples. (b) 6 piscine samples. (c) 8 human samples. (d) 3 porcine samples. (e) 5 bovine samples. L1 is epithelium, L2 is the remaining corneal layers, and overall is the entire cornea thickness.

Species	Parameters	Layer		
		L1	L2	Overall
Murine	Refractive Index	1.371 ± 0.016	1.360 ± 0.008	1.362 ± 0.005
	Thickness (µm)	57 ± 18	103 ± 26	160 ± 8
	% of total thickness	36%	64%	100%
Piscine	Refractive Index	1.502 ± 0.057	1.335 ± 0.011	1.360 ± 0.009
	Thickness (µm)	43 ± 1	243 ± 8	286 ± 8
	% of total thickness	15%	85%	100%
Human	Refractive Index	1.433 ± 0.023	1.357 ± 0.013	1.363 ± 0.011
	Thickness (µm)	66 ± 10	760 ± 44	826 ± 49
	% of total thickness	8%	92%	100%
Porcine	Refractive Index	1.476 ± 0.091	1.343 ± 0.013	1.357 ± 0.023
	Thickness (µm)	75 ± 19	809 ± 66	884 ± 51
	% of total thickness	8%	92%	100%
Bovine	Refractive Index	1.400 ± 0.007	1.376 ± 0.003	1.380 ± 0.003
	Thickness (µm)	157 ± 8	843 ± 25	1000 ± 19
	% of total thickness	16%	84%	100%

Table 4.6: Refractive index and thickness results for murine, piscine, human, porcine and bovine corneas

For each species, the RI and thicknesses of the two distinct layers of the cornea are averaged over multiple samples and the results are summarized in Table 4.6. For this calculation, the results of 6 murine, 6 piscine, 8 human, 3 porcine, and 5 bovine corneas are averaged for their respective species. Here, the overall RI and thickness are the average RI of the entire cornea (combining L1 and L2) and its corresponding full thickness of the cornea, respectively. The ratios in percentage of the thickness of L1 or L2 to the full corneal thickness are also listed. The RI of L1 and L2 are different across the species likely due to the different cell packing and collagen structures in the epithelium and the stroma, respectively. While the respective RI of L1 and L2 differ greatly across the species, the overall RI appear to be similar around 1.357-1.363 with the exception of the bovine RI which is 1.380. The converging overall RI is caused by the different ratios of the epithelial thickness to the total thickness. For example, murine corneas have the largest ratio of epithelium thickness to total thickness of 36% while the

human corneas have the smallest ratio at 8%. The order in ascending thickness is murine, piscine, human, porcine, and then bovine corneas. The relative corneal thicknesses correlate well with the physical sizes of the respective animals.

4.5 DISCUSSION

4.5.1 CORNEA TRANSPARENCY

Transparency is an important feature of cornea which can be analyzed by the combined MPM/OCT imaging. The corneal transparency is a result of the highly organized collagen packing in the stroma. Swelling disrupts the organized collagen packing and can cause the cornea to have regions of varying RI, which makes the cornea lose its transparency. In the experiment, the human corneas show slight cloudiness due to swelling while the bovine corneas show perfect transparency. In the multimodal imaging, the OCT intensity is directly proportional to the reflectivity of the tissue under the measurement, while the SHG intensity is affected by the intensity of the excitation light and the collagen structure in the tissue. Assuming that the collagen structure is relatively uniform in the cornea, the SHG intensity thus shows the attenuation of the excitation light.

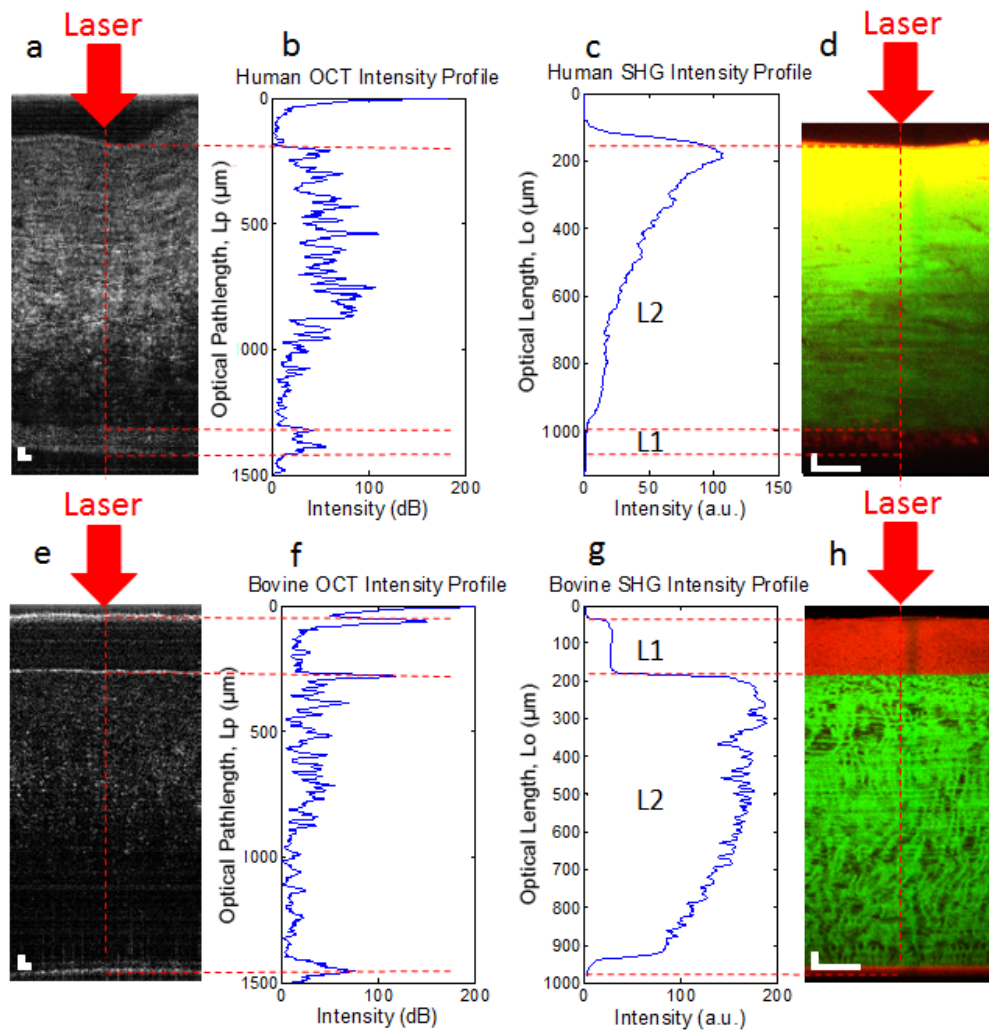


Figure 4.13: Comparison between the OCT and SHG signals of a human cornea and a bovine cornea. (a) – (d) OCT image, OCT intensity profile, SHG intensity profile, MPM cross-sectional image of a human cornea, respectively. (e) – (h) OCT image, OCT intensity profile, SHG intensity profile, and MPM cross-sectional image of a bovine cornea, respectively. L1 is the epithelium layer. L2 is the Bowman’s layer, stroma, Descemet’s membrane, and endothelium layers. Scale bars are 50 μm .

A comparison between the OCT and SHG signal attenuations of a human cornea and a bovine cornea is shown in Figure 4.13. The first row (Figures 4.13(a) – (d)) corresponds to the OCT image, the OCT intensity profile, the SHG intensity profile, and the MPM image of a human cornea, respectively. The second row (Figures 4.13(e) – (h)) displays the same information but for a bovine cornea. The red, horizontally-dashed lines

mark the anterior epithelial boundary, the epithelium and stroma boundary, and the posterior endothelial boundary. The three boundaries for the bovine cornea are clearly identified as the three sharp peaks in the OCT intensity profile in Figure 4.13(f). In the SHG intensity profile, Figure 4.13(g), the epithelium is shown to have minimal SHG signal. At the junction between the epithelium and the stroma, the SHG signal intensity increases dramatically due to the onset of fibrous collagen. Then it attenuates relatively slowly towards the posterior stroma because the bovine cornea is very transparent. The SHG signal is reduced by 2.29 dB over 750 μm . Meanwhile, in the SHG intensity profile of the human cornea as shown in Figure 4.13(c), because the cornea is imaged from the endothelial side, the SHG intensity increases greatly after the endothelium, due to the collagen in the stroma, and then decreases quickly towards the anterior stroma. The SHG intensity is reduced by 7.96 dB over 750 μm . This is significantly higher than in the bovine case because the human corneal samples exhibit cloudiness and thus scatters the light more. The scattering effect of the cloudy human cornea can also be seen in both the OCT image (Figures 4.13(a)) and the OCT intensity profile (Figure 4.13(b)) as strong scattering signals in the stroma. The signal in the middle of the stroma is slightly higher because the focus of the objective lens is set in the middle of the stroma. The cloudiness of the human cornea is likely caused by the micro-folds in the stroma from corneal swelling which have been observed in the MPM images. As there are significant scattering from inside the stroma of the human cornea, the scattering from the three boundaries are not as distinct as in the bovine case. In the bovine stroma, dark gaps between the collagenous signals are observed in the MPM images. These dark gaps lack the SHG contrast which indicates that they are not composed of fibrous type-I collagen.

Since the OCT image of the bovine cornea shows low scattering and these gaps are not observed, we hypothesize that the gaps have similar RI as the surrounding collagenous material.

5.5.1 MORPHOLOGY

In terms of morphology, all the five layers of cornea can be observed by the MPM imaging. In the epithelium, larger winged cells are observed at the anterior epithelium and smaller basal cells from the posterior epithelium. The Bowman's layer can be identified as indistinct and diffused signal in the human corneas, and condensed and randomly-arranged layer of fine collagen fiber bundles in the porcine and bovine corneas. However, not every animal species have a Bowman's layer [6]. Hayashi et al. found the Bowman's layer in the C3H mouse to be approximately 0.8 μm [45]. The Bowman's layer is not distinguished in the MPM *en face* images of the mouse likely because it is thinner than the depth resolution of the MPM system. Collin et al. reported that the Bowman's layer is not present in many of the teleost species [6]. The Bowman's layer is not observed in my tilapia samples because tilapia is a type of teleost fish. Morishige et al. observed similar features as in our Figures 4.7 and 4.8 in the human Bowman's layer [42,43]. Merindano et al. reported the existence of the Bowman's layer in bovine corneas but mentioned that it was difficult to distinguish the Bowman's layer in the case of the pig [6]. In our study, a condensed and randomly-arranged layer of finer collagen fiber bundles is observed just posterior to the epithelium of the porcine and bovine corneas, which is attributed as the Bowman's layer for these species.

In the stroma, similarities and differences in the collagen structures across the different species are noticed. The piscine and the human stromata exhibit thin collagen

fibers that together seem to indicate an overall collagen direction. In the human corneas, long, straight, and dark ridges are seen that are not present in the other species. These ridges are micro-folds caused by corneal swelling. Murine, porcine, and bovine corneas exhibit collagen bundles that form interwoven patterns in the stroma. In the porcine and bovine corneas, the interwoven collagen patterns become finer, and denser towards the posterior ends. Similar stromal morphology has been observed by Bueno et al. for the human, porcine, and bovine corneas [46].

The Descemet's membrane and endothelium can be detected by the TPEF contrast which comes from elastin in the Descemet's membrane and NADH from the endothelium. The endothelium is distinguished as the honeycomb cellular structure, while the surrounding region with homogenous TPEF signal is distinguished as the Descemet's membrane in the murine, human and bovine corneas. In the piscine and porcine corneas, the Descemet's membrane and the endothelium could not be differentiated, because their cellular structure is not clear due to the weak signal.

5.5.3 QUANTITATIVE CHARACTERIZATION

For all the species, higher RI in the epithelium as compared to the stroma is observed. The RI of the two layers vary from species to species possibly due to the different cell packing in the epithelium, and the collagen packing in the stroma. In the literature, the RI of the human epithelium is found to be ~1.397 by Vasudevan et al. and ~1.401 by Patel et al. [30,34], and the human stromal RI is between ~1.373 to ~1.380 [34]. The overall human corneal RI is found to be in the range of 1.37-1.39 [8,12,24,30]. The RI of the bovine epithelium and the stroma are found to be ~1.376 and ~1.372 respectively [30]. My RI values fall within reasonable range from these literature results.

The human corneas measured in my experiment have a higher thickness than the literature value of $\sim 550 \mu\text{m}$ [23,29]. The variation is likely from corneal swelling due to the age of the corneas. Nelson et al. found that rabbit and human corneas experienced increased corneal thickness after 3 weeks in the Optisol storage medium [35].

The precision of the RI measurement has been evaluated previously to be within $\sim 1\%$ error compared to reference values on standard samples like water, air, immersion oil, and cover glass [12]. Although our method can have high precision on non-tissue samples, we notice large error bars in some measurements of the corneas. The variations may come from several factors. Firstly, corneal thicknesses and RI are known to change due to fluctuations in the corneal hydration. In literature, the RI of the stromal surface is found to gradually increase exponentially after exposure to air [38]. We also observed as much as a 30% decrease in the piscine corneal thicknesses when exposed to air. We minimized the variations from corneal hydration by submerging all our samples under either BSS sterile irrigation solution or Optisol corneal storage media during the experiment. Furthermore, since all the samples are *ex vivo*, the epithelium and endothelium layers degrade continuously which reduces their ability to maintain corneal hydration. Secondly, there is an inherent sample to sample variation. This can be differences in age, sex, size, and healthy of the sample. Finally, the accuracy of the RI measurement is also affected by the sample thickness where a thinner sample tends to have lower accuracy. Thus the epithelium generally has lower accuracy than the stroma.

CHAPTER 5: INDUCED ACANTHAMOEBA KERATITIS IMAGING

APPLICATION

5.1 INTRODUCTION

Corneal disease is a leading cause of blindness worldwide [47]. In developing and underdeveloped countries, it accounts for up to 90% of vision loss cases. In these countries, vision loss is often caused by infectious agents such as bacteria, viruses, protozoa, and fungi, or by non-infectious conditions such as immune or autoimmune conditions and trauma. Keratitis, an inflammatory condition of the cornea, exists in all of the above cases. If left untreated, keratitis can lead to blindness. In this chapter, infectious keratitis will be discussed; specifically, a common protozoa keratitis caused by the *Acanthamoeba* species.

5.1.1 ACANTHAMOEBA KERATITIS

Acanthamoeba is one of the most common protozoa found in soil, fresh water and other habitats. Protozoa are a type of eukaryotic organism (organisms whose cells contain a nucleus and organelles, enclosed within membranes) with animal-like behaviour. *Acanthamoeba* is a parasitic protozoon and consumes nutrients from its host. It can exist in either a trophozoite or a cyst stage [48]. In the trophozoite stage (25-40 μm in diameter), the parasite actively absorbs the nutrients from its host [49]. However, when the environment becomes unfavourable, the parasite becomes metabolically inactive and enters its cyst stage (15-30 μm in diameter). In the cyst stage, *Acanthamoeba* can survive up to a year in extreme temperature, pH and osmolarity [48]. It also becomes very resistant to the host's immune response or external anti-microbial

agents. When the environment becomes favourable again, the parasite can return to its trophozoite form. Figure 5.1 shows a scanning electron microscope image of a species of *Acanthamoeba*, *Acanthamoeba castellanii*. Figures 5.2(a) and 5.2(b) show light microscope images of *Acanthamoeba castellanii* in its trophozoite and cyst stages, respectively. Eight species of *Acanthamoeba* have been reported to cause *Acanthamoeba keratitis* (AK) [48]: *A. castellanii*; *A. polyphaga*; *A. hatchetti*; *A. culbertsoni*; *A. rhyodes*; *A. lugdunensis*; *A. quina*; and *A. griffin*.

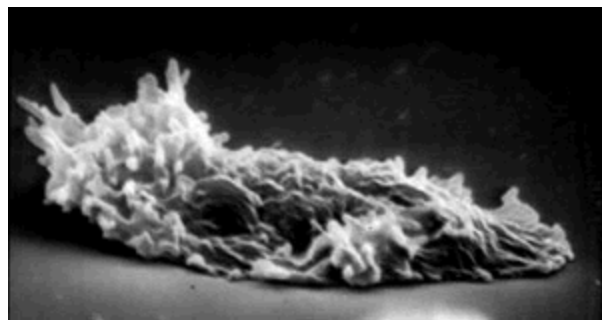


Figure 5.1: Scanning electron microscope image of *Acanthamoeba castellanii* [50]

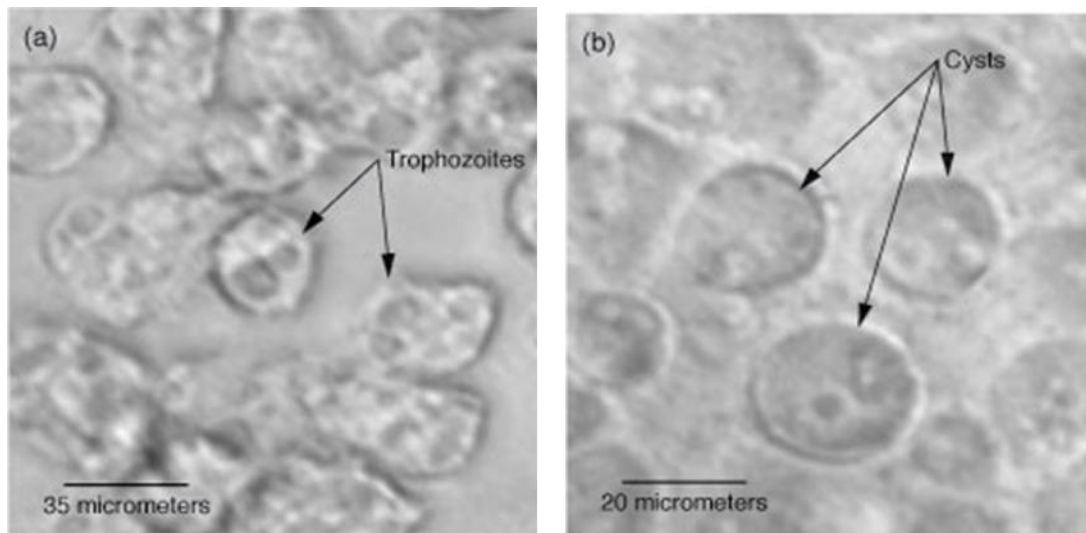


Figure 5.2: *Acanthamoeba castellanii* in the trophozoite and cyst stages [51]. (a) *Acanthamoeba castellanii* in the trophozoite stage. (b) *Acanthamoeba castellanii* in the cyst stage.

AK is usually associated with trauma, contact with objects, previous ocular surgery, exposure to contaminated water or soil and poor socioeconomic conditions

[48,49]. However, since the introduction of soft contact lens in the 1970s, the number of cases of AK has increased dramatically [48]. Currently, about 85% of the time, AK is associated with users of contact lenses. The causes for AK for contact lens wearers include swimming with contact lenses, improper contact lens care or using home-made saline solutions [48,49].

The symptoms associated with AK are red eye, photophobia, decreased visual acuity, foreign body sensation, swelling, tearing and intense pain [47,49]. Figure 5.3 shows ocular images of a patient suffering AK.

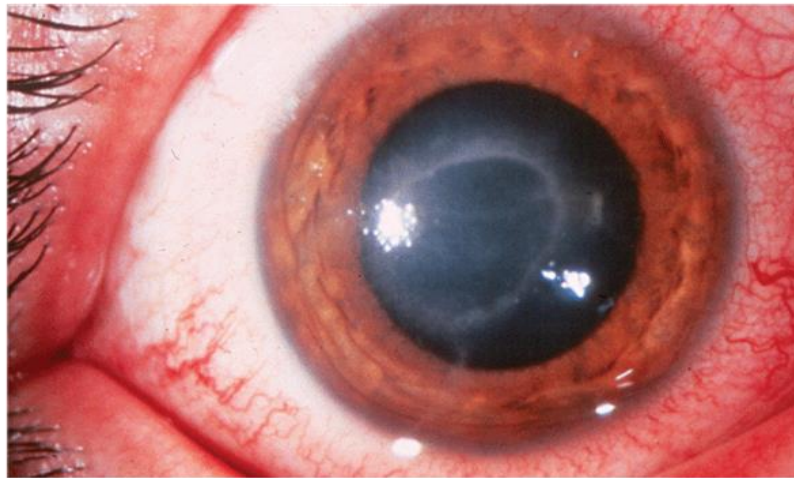


Figure 5.3: Patient with Acanthamoeba Keratitis [52].

To date, clinicians still rely on the subjective evaluation of the cornea using slit-lamp microscopes to identify keratitis (Figure 5.4) [47]. However, this instrument is developed over a century ago and often cannot differentiate between the various infectious agents causing the keratitis [47,48]. In fact, clinical presentation of AK can mimic bacterial, viral, or fungal infections [48]. This is especially problematic since the treatment for each infection is different and can be detrimental to the cornea and its future recovery [48]. Definitive diagnosis requires cell culture, histology or the identification of the Acanthamoeba by polymerase chain reaction (PCR). Cultures from

the conjunctiva lines inside the eyelid or from corneal scrapping can be taken and stained to identify the existence of the protozoa. However, these methods can be misleading if there are other infections present [48,53]. PCR can also be utilized to identify Acanthamoeba infections. PCR is a method to amplify a few copies of a piece of DNA to millions of copies. By applying primers, which are targets, specific to the Acanthamoeba DNA sequences, this method can achieve high sensitivity of Acanthamoeba detection [48]. However, both the culturing and the PCR methods require up to several weeks to perform and in the meantime, the patient may be subjected to an improper treatment. Finally, if the infection is deep inside the cornea, a biopsy may be required which is much more invasive to the eye [47].



Figure 5.4: Slit-lamp microscope [54]

Once AK is suspected or identified, a combination of anti-microbial agents is used for its treatment [48]. The therapeutic process can take up to 12 months baring major setbacks [48]. After treatment, the patient will need to be monitored closely for recurrence [48]. 90% of the patients will retain visual acuity of 6/12 or better and less than 2% may become blind [48]. A visual acuity of 6/12 means the person needs to be as close as 6 meters to see objects clearly that a person with normal eyesight could see from

12 meters away. Prolonged AK can lead to other complications such as cataract, peripheral ulcerative keratitis, and glaucoma [49].

5.1.2 PROJECT MOTIVATION AND OVERVIEW

Early and accurate diagnosis of AK is critical for successful treatment and follow-up [47]. However, current clinical diagnosis method is subjective and cannot definitively differentiate between the different types of infections. This can result in improper treatments which are detrimental to the eye and its future recovery. Laboratory diagnosis methods can identify the various types of infections but require invasive methods and can take several weeks to perform. Late diagnosis can lead to increased cost, morbidity and poor visual outcomes [47]. Therefore, there exists a need for clinical diagnosis through non-invasive medical imaging techniques. Currently, confocal microscopy (CM) and optical coherence tomography (OCT) can be used clinically to help with the diagnosis of keratitis.

Near infrared CM has the ability to detect AK cysts [55]. It can also identify fibroblast, Langerhans cells, nerve fibers and corneal endothelial cells which can provide additional information about the corneal immunology [47]. Corneal fibroblasts, also known as keratocytes, are cells that synthesize the extracellular matrix and collagen in the stroma. They are activated when the cornea experiences inflammation or requires wound healing. CM, however, is not effective in identifying the structural changes in the stromal collagen [55]. It cannot differentiate between different connective tissues such as collagen and elastin. Finally, turbidity, which is common in most keratitis, can also create additional background reflections and decrease the quality of the CM images.

OCT can be used to observe changes in the corneal thickness, which can provide information about the infection and the treatment progress [47]. However, it cannot be used to identify the infectious agent due to its lower resolution, and it has difficulty differentiating scars from inflammation.

MPM has not been implemented clinically due to its slow image acquisition as well as its relatively high cost and in-portability; however it provides many advantages over the aforementioned imaging techniques [47]. MPM has low photo-toxicity, deep penetration, and high resolution. It is also label free and has optical sectioning capability. It can see cells and collagen through its TPEF and SHG contrasts. Therefore, it can identify the infectious agent and observe the cellular and the collagen responses to the infection.

Although MPM has not been used *in vivo*, it has been used to study different infectious keratitis in *ex vivo*. Tan et al. has imaged bacterial, fungal, and *Acanthamoeba* keratitis using MPM [56]. They imaged excised tissues that are culture-proven to contain the three types of infections. My study and this chapter attempt to reproduce Tan et al.'s results for *Acanthamoeba* keratitis. However, instead of acquiring culture-proven corneal tissues with AK, I used *ex vivo* corneas that are inoculated with *Acanthamoeba castellanii*, which is one of the most common causes of AK [48]. The objective of this project is to inoculate *ex vivo* human corneas with *Acanthamoeba castellanii* using a syringe, and identify features of the *Acanthamoeba* infection. The groundwork necessary to start the project and the people involved are highlighted in Appendix A. Due to limitations in time, training and personnel, my project and this chapter will act as a pilot

study and set up the groundwork for future research. The possible future research directions are presented in Chapter 6.

5.2 METHOD

The human corneas are acquired from the VGH eye bank. They are transferred to Teresa Lo to store in a fridge at the BCCDC parasitology lab. The corneas are inoculated with *Acanthamoeba castellanii* by Dr. Imperial at BCCDC. The inoculation process is:

1. The corneas are rinsed with BSS sterile irrigation solution 3 times to get rid of the Optisol corneal storage media as it may contain compounds that affect the *Acanthamoeba castellanii*.
2. Some corneas are injected with 0.1 ml of 8×10^5 *Acanthamoeba castellanii* cultures using a 0.3112 mm diameter needle (B-D Precision Glide Needle, 30G½) and syringe (Terumo Syringe, 27G × ½).
3. Other corneas are injected with saline instead to provide the control samples

The equipment used is displayed in Figure 5.5. A photo of the injection process is shown in Figure 5.6.



Figure 5.5: The inoculation equipment. (From left to right) Sterile needles and syringes; Two *Acanthamoeba castellanii* cultures; and an ex vivo corneal button stored inside Optisol corneal storage media.

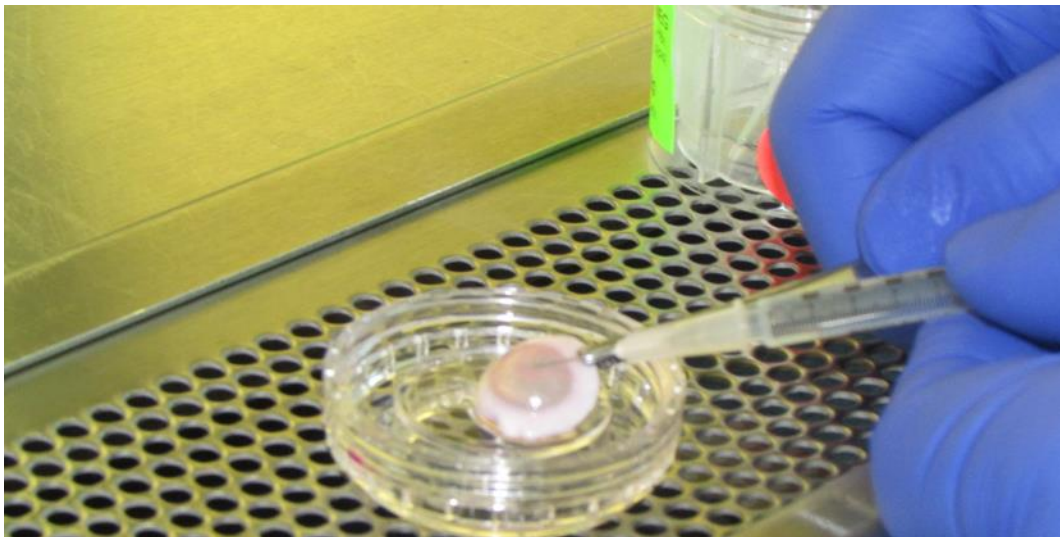


Figure 5.6: The inoculation process

I am notified on the same day to pick up the samples for imaging. The samples are positioned inside a container with the laser source entering the anterior side first as shown in Figure 5.7. These corneas are submerged under BSS sterile irrigation solution, and then imaged. The samples are primarily imaged with the 40× water immersion

objective lens. However, in a later experiment, the 60× water immersion objective lens is used.

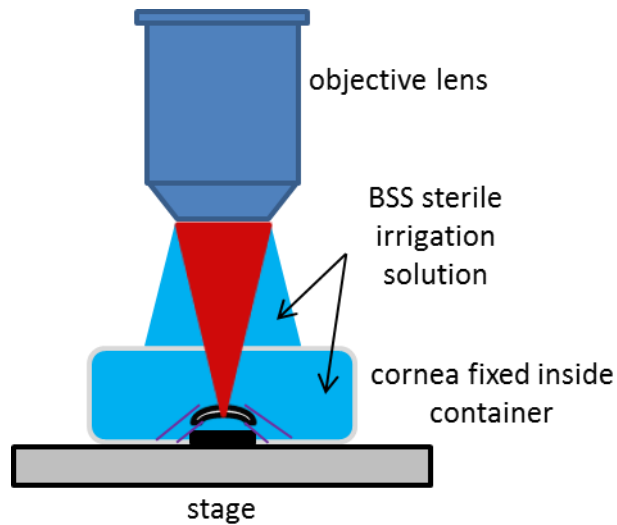


Figure 5.7: AK corneal imaging setup

5.3 RESULTS

Figures 5.8(a) and 5.8(b) show the TPEF and SHG images of an inoculated cornea using the 40× objective lens, respectively. In Figure 5.8(a) the Acanthamoeba cysts are identified with the red arrows. In Figure 5.8(b) the collagen structure in the stroma is observed.

Figure 5.9 shows a different location of an inoculated cornea using the 40× objective lens. Two keratocytes are observed in Figure 5.9(a), as indicated by the red arrows.

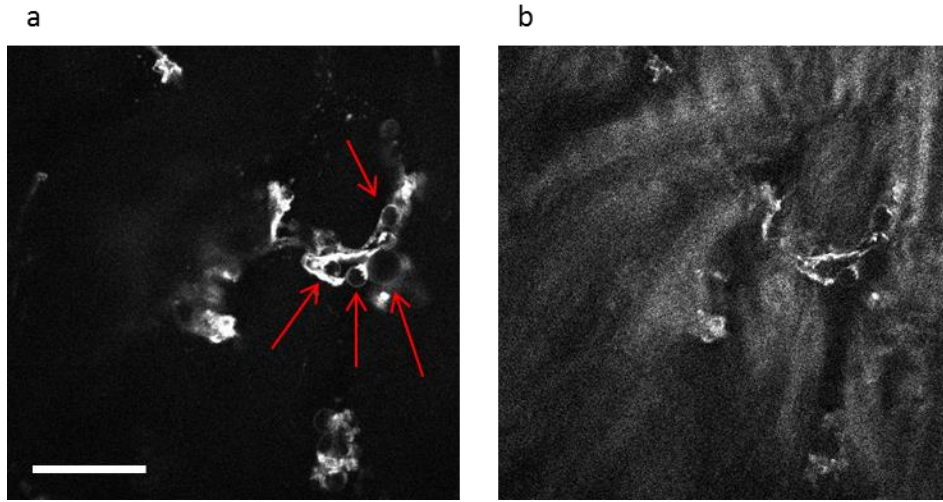


Figure 5.8: Acanthamoeba cysts using the 40 \times objective lens. (a) TPEF channel. (b) SHG channel. Red arrows point to the Acanthamoeba cysts. Scale bar is 50 μ m.

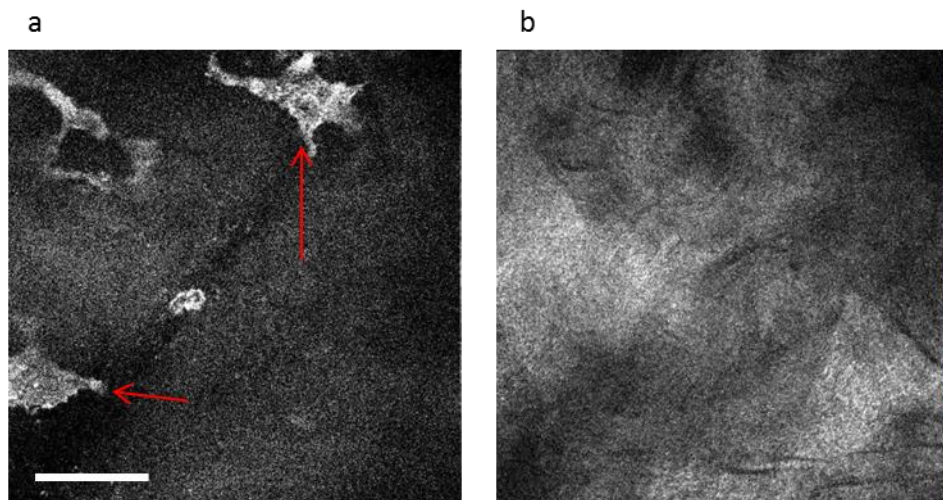


Figure 5.9: Keratocytes in the inoculated sample using the 40 \times objective lens. (a) TPEF channel. (b) SHG channel. Red arrows point to the keratocytes. Scale bar is 50 μ m.

Figures 5.10(a) and 5.10(b) show the TPEF and SHG images of an inoculated cornea using the 60 \times objective lens, respectively. Again, the Acanthamoeba cysts are identified with the red arrows. Some TPEF signal is leaked into the SHG channel, as indicated by the yellow arrow in Figure 5.10(b).

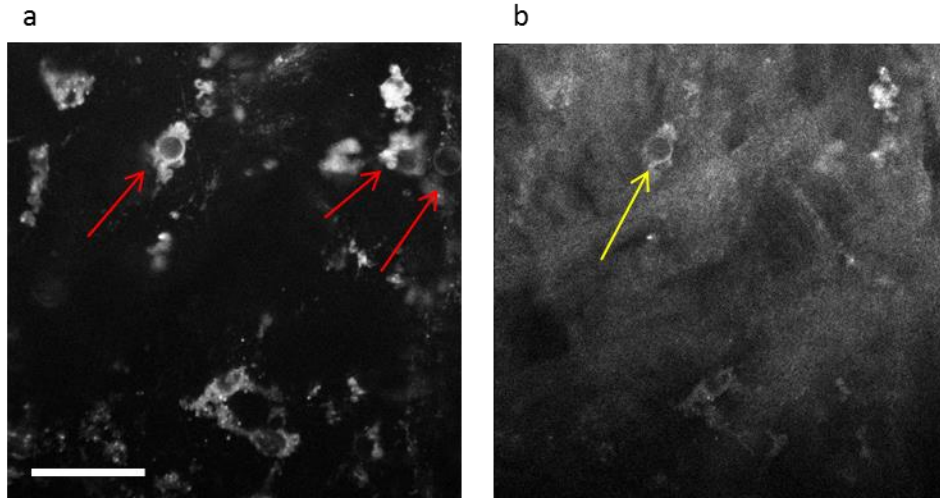


Figure 5.10: Acanthamoeba cysts using the 60× objective lens. (a) TPEF channel. (b) SHG channel. Red arrows point to the Acanthamoeba cysts. Yellow arrow points to leakage signal from the TPEF channel. Scale bar is 33 μm.

Figures 5.11(a) and 5.11(b) show the TPEF and SHG images of a control cornea using the 60× objective lens, respectively. Here, as expected, we do not observe any Acanthamoeba cysts; however, we notice some TPEF structures in Figure 5.11(a).

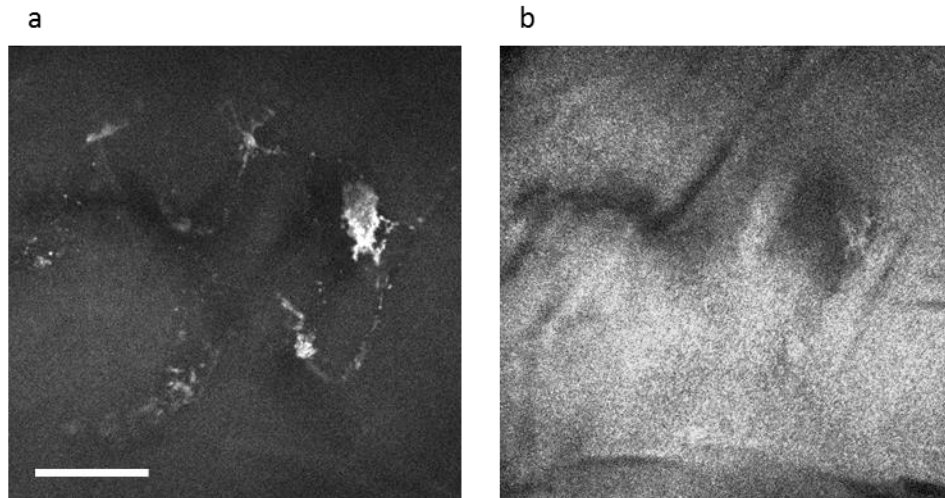


Figure 5.11: Control sample using the 60× objective lens. (a) TPEF channel. (b) SHG channel. Scale bar is 33 μm.

5.4 DISCUSSION

As shown in Figures 5.8 and 5.10, I have successfully identified *Acanthamoeba* cysts in the inoculated human corneas. In Figure 5.9, keratocytes are observed. The existence of the keratocytes is likely from the cornea's response to the *Acanthamoeba* infiltration. Figure 5.12 shows the TPEF, SHG and the merged images of a stromal location of a normal *ex vivo* human cornea from Chapter 4. The left and middle images are TPEF and SHG signals in greyscale. The right image is the merged image with TPEF signal in red and SHG signal in green. Here, we see similar collagen structures as the stroma from the control sample in Figures 5.11(b). However, we notice almost no TPEF signal in Figure 5.12, whereas, in Figure 5.11, unknown TPEF structures are observed. In addition, we observe plenty of TPEF structures that are not cysts in the inoculated corneas (Figures 5.8(a) and 5.10(a)). Therefore, we suspect that the non-cyst TPEF structures seen in the inoculated and the control samples are by products of the injection process. Although the clinical doctors are able to confirm the existence of the *Acanthamoeba* cysts and the keratocytes, they could not identify the sources of these non-cyst TPEF structures. As such, additional studies need to be performed in the future, as will be discussed in Chapter 6. This study shows that MPM can potentially be used clinically for corneal disease diagnosis. The ability to identify an infection at an early stage and to differentiate between different infection types will be a major advancement in the diagnosis and treatment of infectious keratitis.

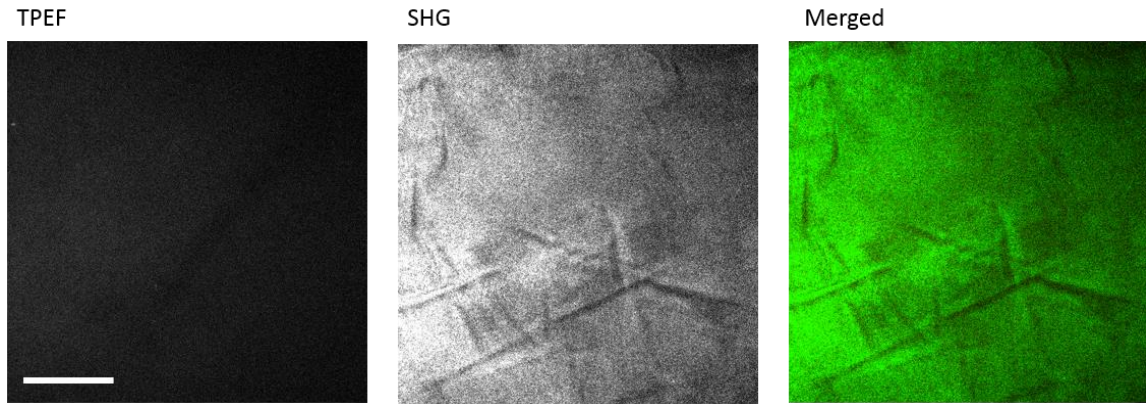


Figure 5.12: MPM stromal image of human corneas from Chapter 4. TPEF signal is in red and SHG signal is in green. Scale bar is 50 μm .

CHAPTER 6: CONCLUSIONS AND FUTURE WORK

6.1 CONCLUSIONS

A combined MPM and OCT system is used to image normal and diseased corneas. Firstly, the advantages and capabilities of the system are shown through the visualization and characterization of five different species of normal corneas. The five species studied are mouse, fish, human, pig, and cow. The similarities and differences within the corneal morphologies of the five species are identified. Furthermore, the thicknesses and RI of the major corneal layers are determined. Secondly, the MPM modality is used to identify *Acanthamoeba* cysts in induced parasitic infections in *ex vivo* human corneas. The visualization of the corneal morphologies for both normal and diseased corneas, and the quantitative characterization of the thicknesses and RI of the major corneal layers are successfully achieved using the combined system. The study serves as an important step towards bringing the combined MPM and OCT technology into clinical setting.

In order to image the entire thickness of the thicker corneal tissues, the OCT modality is altered in two ways. Firstly, a prism-based hardware dispersion balancing unit is added in the reference arm to minimize the dispersion mismatch between the sample beam and the reference beam. Through the addition of the HDBU, the maximum imaging depth, axial resolution and signal to noise ratio are increased, while the sensitivity fall-off and the DC band due to the OCT image reconstruction process are minimized. Secondly, two OCT configurations are interchangeably used to image the thinner and thicker corneal tissues. A 10× objective lens with an effective $f = 37.5$ mm compound lens in the spectrometer is used to image the murine and piscine corneas. A

4× objective lens with an effective $f = 100$ mm compound lens in the spectrometer is used to image the human, porcine, and bovine corneas. The capability of the multimodal imaging system is demonstrated in Chapter 4. The five layers of the cornea, which are the epithelium, Bowman's layer, stroma, Descemet's membrane, and endothelium, can be distinguished respectively by the high resolution MPM modality with the TPEF and SHG contrasts from the cells and the collagen fibers. The Bowman's layer is observed in the human, porcine, and bovine corneas but not in the murine and piscine corneas. The stroma also shows significantly different collagen structures among the five species. With the co-registered MPM and OCT images, the RI and thickness of the two major layers of cornea, the epithelium and stroma, are quantified for the five species. While the overall RI of the entire corneal thickness is similar, the respective RI of the epithelium and stroma vary greatly among the species. Furthermore, the RI of the epithelium is found to be higher than the stroma in all the five species.

The MPM modality of the multimodal system is also utilized for a specific application in ophthalmology. Since clinical diagnosis of *Acanthamoeba* keratitis can be subjective while laboratory diagnosis can take up to several weeks, there exists a need for clinical diagnosis through non-invasive medical imaging techniques. Therefore, in Chapter 5, *ex vivo* human corneas are inoculated with *Acanthamoeba castellanii* using a syringe and imaged with MPM. *Acanthamoeba* cysts are successfully identified in the inoculated samples. Keratocytes are also observed in the corneal stroma, possibly due to the cornea's response to the *Acanthamoeba* infection. Additional non-cyst TPEF structures are observed in both the inoculated and the control samples. However, they are not present in any human corneas imaged in Chapter 4. Therefore, we hypothesize that

these structures are a by-product of the injection method, and not caused by the *Acanthamoeba* infection. Due to the limitation in time, training and personnel, the project was stopped here. However, the groundwork is set up for future research which is outlined in the next section.

6.2 FUTURE WORK

In order to apply the combined imaging system to a wide range of applications in ophthalmology, several aspects of the system must be improved. Firstly, the OCT modality needs deeper penetration while maintaining source limited resolution. This can be achieved through: a pre-spectrometer beam-expander to improve the focus of the light onto the CCD camera; and a line CCD camera with more pixels and larger pixel area. Secondly, for clinical studies, the MPM modality needs to acquire images quicker to reduce motion artifacts from the patient. This requires the implementation of faster scanning methods. However, as the imaging speed is increased, the image quality will ultimately be limited by the signal to noise ratio. To increase the signal level, the laser power can be increased while keeping it below the safety limit. Alternatively, a laser with a shorter pulse-width can be used to excite TPEF and SHG signals more efficiently.

Quantitative characterization of the cornea can be investigated further by moving the research into animal studies. For instance, the relationship between intraocular pressure, and corneal thickness, RI and hydration can be identified by measuring these values from an *in vivo* rabbit.

For the diagnosis of *Acanthamoeba* keratitis, there are many possible future directions. Firstly, histology can be performed on the inoculated and control samples to help identify the unknown TPEF structures observed in Figures 5.8 – 5.11. Secondly,

instead of inoculating the corneas, we can study excised tissues with culture-proven AK. Since *ex vivo* tissues may not represent realistic infection process and corneal response, this project should move into animal studies as well. We can study the cornea's response to an infection over time on an *in vivo* rabbit cornea. In addition, we can compare different anti-microbial agents for different species of AK over time to determine the best treatments. Finally, all of these directions can be expanded upon by looking at other infectious agents such as bacteria, fungi and viruses.

BIBLIOGRAPHY

- [1] B. E. Goldstein, *Sensation & Perception* (Cengage Learning, 2007).
- [2] D. W. DelMonte, and T. Kim, "Anatomy and physiology of the cornea," *J. Cataract Refract. Surg.* **37**, 588-598 (2011).
- [3] R. F. Guthoff, A. Zhivov, and O. Stachs, "In vivo confocal microscopy, an inner vision of the cornea – a major review," *Clinical and Experimental Ophthalmology* **37**, 100-117(2009).
- [4] NTD.TV, "New artificial corneas bring hope to thousands," 2012 [online], Available: <http://www.ntd.tv/en/news/science-technology/20121014/75087-new-artificial-corneas-bring-hope-to-thousands-.html>
- [5] Simple Medicine, "Histology of cornea," 2008 [online], Available: <http://simple-med.blogspot.ca/2008/07/histology-of-cornea.html>
- [6] M. D. Merindano, J. Costa, M. Canals, J. M. Potau, and D. Ruano, "A comparative study of Bowman's layer in some mammals: relationships with other constituent corneal structures," *Eur. J. Anat.* **6**(3), 133-139 (2002).
- [7] K. M. Meek, and A. J. Quantock, "The use of x-ray scattering technique to determine corneal ultrastructure," *Progress in Retinal and Eye Research* **20**(1), 95-137 (2001).
- [8] Y. L. Kim, J. T. W. Jr, T. K. Goldstick, and M. R. Glucksberg, "Variation of corneal refractive index with hydration," *Phys. Med. Biol.* **49**, 859 (2004).
- [9] F. Aptel, N. Olivier, A. Deniset-Besseau, J. M. Legeais, K. Plamann, M. c. Schanne-Klein, and E. Beaurepaire, "Multimodal nonlinear imaging of the human cornea," *Investigative Ophthalmology & Visual Science* **51**(5), 2459-2465 (2010).

- [10] W. R. Zipfel, R. M. Williams, and W. W. Webb, "Nonlinear magic: multiphoton microscopy in the biosciences," *Nat. Biotech.* **21**(11), 1369-1377 (2003).
- [11] S. Tang, Y. Zhou, K. K. H. Chan, and T. Lai, "Multiscale multimodal imaging with multiphoton microscopy and optical coherence tomography," *Opt. Lett.* **36**(24), 4800-4802 (2011).
- [12] Y. Zhou, K. K. H. Chan, T. Lai, and S. Tang, "Characterizing refractive index and thickness of biological tissues using combined multiphoton microscopy and optical coherence tomography," *Biomed. Opt Express* **4**(1), 38-50 (2012).
- [13] B. J. Kaluzny, J. J. Kaluzny, A. Szkulmowska, I. Gorczynska, M. Szkulmowski, T. Bajraszewski, M. Wojtkowski, and P. Targowski, "Spectral optical coherence tomography," *Cornea* **25**(8), 960-965 (2006).
- [14] J. M. Schmitt, "Optical coherence tomography (OCT): a review," *IEEE Journal of Selected Topics in Quantum Electronics* **5**(4), pp. 1205-1215 (1999).
- [15] G. J. Tearney, M. E. Brezinski, J. F. Southern, B. E. Bouma, S. A. Boppart, and J. G. Fujimoto, "Optical biopsy in human gastrointestinal tissue using optical coherence tomography," *Am. J. Gastroenterol.* **92**(10), pp. 1800-1804 (1997).
- [16] C. Pitris, A. Goodman, S. A. Boppart, J. J. Libus, J. G. Fujimoto, and M. E. Brezinski, "High-resolution imaging of gynecologic neoplasms using optical coherence tomography," *Obstetrics & Gynecology* **93**(1), pp. 135-139 (1999).
- [17] C. Pitris, M. E. Brezinski, B. E. Bouma, G. J. Tearney, J. F. Southern, and J. G. Fujimoto, "High resolution imaging of the upper respiratory tract with optical coherence tomography," *Am. J. Respir. Crit. Care Med.* **157**(5), pp. 1640-1644 (1998).

- [18] G. J. Tearney, M. E. Brezinski, J. F. Southern, B. E. Bouma, S. A. Boppart, and J. G. Fujimoto, "Optical biopsy in human urologic tissue using optical coherence tomography," *J. Urology* **157**(5), pp. 1915-1919 (1997).
- [19] U. L. Meuller-Lisse, M. Bader, M. Bauer, E. Engelram, Y. Hocaoglu, M. Puls, O. A. Messner, G. Babaryka, R. Sroka, C. G. Stief, M. F. Reiser, and U. G. Meuller-Lisse, "Optical coherence tomography for the upper urinary tract: review of initial experience ex vivo and in vivo," *Medical Laser Application* **25**, pp. 44-52 (2010).
- [20] M. E. Brezinski, G. J. Tearney, B. E. Bouma, S. A. Boppart, M. R. Hee, E. A. Swanson, J. F. Southern, and J. G. Fujimoto, "Imaging of coronary artery microstructure (in vitro) with optical coherence tomography," *Am. J. Cardiology* **77**(1), pp. 92-93 (1996).
- [21] B. R. Masters, "Correlation of histology and linear and nonlinear microscopy of the living human cornea," *J. Biophoton.* **2**(3), 127-139 (2009).
- [22] N. Efron, I. Perez-Gomez, H. A. Mutalib, and J. Hollingsworth, "Confocal microscopy of the normal human cornea," *Contact Lens and Anterior Eye* **24**, 16-24 (2001).
- [23] S. Shah, A. Chatterjee, M. Mathai, S. P. Kelly, J. Kwartz, D. Henson, and D. McLeod, "Relationship between corneal thickness and measured intraocular pressure in a general ophthalmology clinic," *Ophthalmology* **106**, 2154-2160 (1999).
- [24] S. R. Uhlhorn, F. Manns, H. Tahi, P. Rol, and J. M. Parel, "Corneal group refractive index measurement using low-coherence interferometry," *SPIE* **3246**, 14-21 (2003).

- [25] J. W. McLaren, C. B. Nau, J. C. Erie, and W. M. Bourne, "Corneal thickness measurement by confocal microscopy, ultrasound, and scanning slit methods," *American Journal of Ophthalmology* **137**(6), 1011-1020 (2004).
- [26] M. Benchmann, M. J. Thiel, A. S. Neubauer, S. Ullrich, K. Ludwig, K. R. Kenyon, and M. W. Ulbig, "Central corneal thickness measurement with a retinal optical coherence tomography device versus standard ultrasonic pachymetry," *Cornea* **20**(1), 50-54 (2001).
- [27] C. Wirbelauer, and D. T. Pham, "Continuous monitoring of corneal thickness changes during LASIK with online optical coherence pachymetry," *J. Cataract Refract. Surg.* **30**, 2559-2568 (2004).
- [28] Y. Barkana, Y. Gerber, U. Elbaz, S. Schwartz, G. Ken-Dror, I. Avni, and D. Zadok, "Central corneal thickness measurement with the pentacam scheimpflug system, optical low-coherence reflectometry pachymeter, and ultrasound pachymetry," *J. Cataract Refract. Surg.* **31**, 1729-1735 (2005).
- [29] A. Faramarzi, and H. Ziai, "Central corneal thickness measurement by ultrasound versus Orbscan II," *J. Ophthalmic Vis. Res.* **3**(2), 83-86 (2008).
- [30] B. Vasudevan, T. L. Simpson, and J. G. Sivak, "Regional variation in the refractive-index of the bovine and human cornea," *Optometry and Vision Science* **85**, 977-981 (2008).
- [31] K. D. rao, Y. Verma, H. S. Patel, and P. K. Gupta, "Non-invasive ophthalmic imaging of adult zebrafish eye using optical coherence tomography," *Current Science* **90**(11), 1506-1510 (2006).

- [32] G. J. Tearney, "Determination of the refractive index of highly scattering human tissue by optical coherence tomography," *Optics Letters* **20**(21), 2258-2260 (1995).
- [33] P. J. Campagnola, and L. M. Loew, "Second-harmonic imaging microscopy for visualizing biomolecular arrays in cells, tissues and organisms," *Nature Biotechnology* **21**, pp. 1356-1360 (2003).
- [34] S. Tang, T.B. Krasieva, Z. Chen, B.J. Tromberg, "Combined multiphoton microscopy and optical coherence tomography using a 12-fs broadband source", *J. Biomed. Opt.* **11**, pp. 020502 (2006).
- [35] Esposito, F. Federici, C. Usai, F. Cannone, G. Chirico, M. Collini, A. Diaspro, "Notes on theory and experimental conditions behind two-photon excitation microscopy", *Microscopy Research and Technique* **63**, pp. 12-17 (2004).
- [36] P.J. Campagnola, M. Wei, A. Lewis, and L.M. Loew, "High-Resolution Nonlinear Optical Imaging of Live Cells by Second Harmonic Generation", *Biophysical Journal* **77**, pp. 3341-3349 (1999).
- [37] P. Fratzl, *Collagen: Structure and Mechanics*, (Springer, 2008).
- [38] R.M. Williams, D.W. Piston, and W.W. Webb, "Two-photon molecular excitation provides intrinsic 3-dimensional resolution for laser-based microscopy and microphotochemistry", *The FASEB Journal* **8**, pp. 804-13 (1994).
- [39] K.K.H. Chan, "Spectral Domain Optical Coherence Tomography System Design: sensitivity fall-off and processing speed enhancement", Master's Thesis, University of British Columbia (2010).

- [40] Y. F. Zhou, "Design and Application of Combined Multiphoton Microscopy and Optical Coherence Tomography System," Master's Thesis, University of British Columbia (2012).
- [41] A. Dubois, L. Vabre, A. C. Boccara, and E. Beaurepaire, "High-Resolution Full-Field Optical Coherence Tomography with a Linnik Microscope", *App. Opt.* **41**, pp. 805-812 (2002).
- [42] N. Morishige, A. J. Wablert, M. C. Kenney, D. J. Brown, K. Kawamoto, T. Chikama, T. Nishida, and J. V. Jester, "Second-harmonic imaging microscopy of normal human and keratoconus cornea," *Investigative Ophthalmology & Visual Science* **48**, 1087-1094 (2007).
- [43] N. Morishige, W. M. Petroll, T. Nishida, C. Kenney, and J. V. Jester, "Noninvasive corneal stromal collagen imaging using two-photon-generated second-harmonic signals," *J. Cataract Refract. Surg.* **32**, 1784-1791 (2006).
- [44] G. Latour, I. Gusachenko, L. Kowalczyk, I. Lamarre, and M. Schanne-Klein, "In vivo structural imaging of the cornea by polarization-resolved second harmonic microscopy," *Biomed. Opt Express* **3**(1), 1-15 (2011).
- [45] S. Hayashi, T. Osawa, and K. Tohyama, "Comparative observations on corneas, with special reference to Bowman's layer and Descemet's membrane in mammals and amphibians," *J. Morph.* **254**, 247-258 (2002).
- [46] J. M. Bueno, E. J. Gualda, and P. Artal, "Analysis of corneal stroma organization with wavefront optimized nonlinear microscopy," *Cornea* **30**(6), 692-701 (2011).

- [47] D. Mantopoulos, A. Cruzat, and P. Hamrah, "In vivo imaging of corneal inflammation: new tools for clinical practice and research," *Semin Ophthalmol.* **25**(5-6), p. 178-185 (2010).
- [48] D. A. Schaumberg, K. K. Snow, and M. R. Dana, "The epidemic of acanthamoeba keratitis: where do we stand?" *Cornea* **17**(1), p. 3-10 (1998).
- [49] J. K. G. Dart, V. P. J. Saw, and S. Kilvington, "Acanthamoeba keratitis: diagnosis and treatment," *American Journal of Ophthalmology* **148**(4), p. 487-499 (2009).
- [50] The University of Edinburgh, "Acanthamoeba," 2003 [online], Available: http://www.cdc.gov/parasites/acanthamoeba/health_professionals/acanthamoeba_keratitiss_images.html
- [51] Science & Technology Review, "Insight into a deadly disease," 2010 [online], Available: <https://str.llnl.gov/JulAug10/rasley.html>
- [52] M. B. Abelson, D. Dewey-Mattia, and A. Shapiro, "Acanthamoeba: a dangerous pathogen," 2008 [online], Available: http://www.revophth.com/content/d/therapeutic_topics/i/1223/c/23018/
- [53] Y. Sun, W. Lo, R. J. Wu, S. J. Lin, W. C. Lin, S. H. Jee, H. Y. Tang, and C. Y. Dong, "Multiphoton microscopy for imaging infectious keratitis: demonstration of pattern of microbial spread in an experimental model," *SPIE* **6138**, p. 61381V (2006).
- [54] MedicinePlus, "Slit-lamp exam," 2013 [online], Available: <http://www.nlm.nih.gov/medlineplus/ency/imagepages/1140.htm>
- [55] P. Steven, M. Muller, N. Koop, C. Rose, and G. Huttmann, "Comparison of corneal module and DermaInspect for noninvasive imaging of ocular surface pathologies," *J. Biomed. Opt.* **14**(6), 064040 (2009).

[56] H.Y. Tan, Y. Sen, W. Lo, S.W Teng, R. J. Wu, S. H. Jee, W. C. Lin, C. H. Hsiao, H.C. Lin, Y. F. Chen, D. H. K. Ma, S. C. M. Huang, S. J. Lin, C. Y. Dong, “Multiphoton fluorescence and second harmonic generation microscopy for imaging infectious keratitis,” *J. Biomed. Opt.* **12**(2), 024013 (2007).

APPENDIX A: GROUNDWORK FOR CHAPTER 5

In order to start the infected cornea project, I had to set up the groundwork which includes:

1. Applying for and attaining UBC biosafety and human ethics approvals;
2. Establishing new agreement with Christopher Frketich of the VGH eye bank for additional *ex vivo* human corneal tissues;
3. Presenting the project and recruiting Dr. Miguel Imperial to perform the inoculation since *Acanthamoeba castellanii* is a level 2 biosafety hazard and I am not trained to work with it;
4. Setting up collaboration efforts with Quantine Wong and Teresa Lo from the parasitology lab of the British Columbia Centre for Disease Control (BCCDC) because I do not have access to *Acanthamoeba castellanii* or a level 2 biosafety lab;
5. Presenting the project and recruiting Dr. Simon Holland, Dr. Gregory Moloney, and Dr. Johnson Tan as my clinical advisors.

The people involved in this project are summarized in Table A.1.

Name	Affiliation	Roles
Tom Lai	UBC Biophotonics Lab	Primary researcher; conducts the experiment
Dr. Shuo Tang	UBC Biophotonics Lab	Supervisor
Dr. Simon Holland	Eye Care Centre	Clinical doctor
Dr. Gregory Moloney	Eye Care Centre	Clinical doctor
Dr. Johnson Tan	Eye Care Centre	Clinical doctor
Quantine Wong	BCCDC	Section head of the parasitology lab
Dr. Miguel Imperial	BCCDC	Medical microbiologist; performs the inoculation
Teresa Lo	BCCDC	Lab scientist and Acanthamoeba expert; prepares and maintains the <i>Acanthamoeba castellanii</i>
Christopher Frketch	VGH eye bank	Senior transplant coordinator; prepares and gives Tom Lai the corneal buttons for research

Table A.1: List of people involved

APPENDIX B: RESEARCH ETHICS

The use of human and animal tissues in this thesis is for the sole purpose of demonstrating the imaging capabilities of the combined multiphoton microscopy and optical coherence tomography imaging system. No additional studies were performed on the tissues and no live animals were kept in the lab.

The murine eyeballs were obtained from a collaborator at the BC Cancer Agency. The piscine eyeballs were obtained from a local supermarket. The human corneal buttons were acquired from the Vancouver General Hospital's Eye Bank. They were released for research purposes after the tissues have expired and/or deemed unsuitable for transplantation. The porcine eyeballs were acquired from the UBC Centre for Comparative Medicine. The bovine eyeballs were obtained from a local farm.

The certificate numbers for the biosafety, human ethics, and animal care approvals are H12-01682, A12-0182 and B12-0065, respectively. These certificates were used for both Chapters 4 and 5.

APPENDIX C: LIST OF PUBLICATIONS

1. S. Tang, Y.F. Zhou, K.K.H. Chan, and T. Lai, "Multiscale multimodal imaging with multiphoton microscopy and optical coherence tomography," *Optics Letters* **36**, pp. 4800-4802 (2011).
2. Y. Zhou, K. K. H. Chan, T. Lai, and S. Tang, "Characterizing refractive index and thickness of biological tissues using combined multiphoton microscopy and optical coherence tomography," *Biomed. Opt. Express* **4**(1), 38-50 (2012).
3. S. P. Chong, T. Lai, and S. Tang, "Tri-modal microscopy with multiphoton and optical coherence microscopy/tomography for multi-scale and multi-contrast imaging," *Biomed. Opt. Express* **4**(9), 1584-1594 (2013).
4. T. Lai and S. Tang, "Cornea characterization using a combined multiphoton microscopy and optical coherence tomography system," *Biomed. Opt. Express* **5**(5), 1494-1511 (2014).